

Mathematical Model Development and Experimental Verification of Electromagnetic Force Actuators for use in Space Applications

Robert C. Youngquist

NASA, Applied Physics Laboratory, Kennedy Space Center, Florida

Mark A. Nurge

NASA, Applied Physics Laboratory, Kennedy Space Center, Florida

Katherine T. Wilson

Cornell University, Sibley School of Mechanical and Aerospace Engineering, Ithaca, New York

NASA STI Program... in Profile

Since its founding, NASA has been dedicated to the advancement of aeronautics and space science. The NASA scientific and technical information (STI) program plays a key part in helping NASA maintain this important role.

The NASA STI Program operates under the auspices of the Agency Chief Information Officer. It collects, organizes, provides for archiving, and disseminates NASA's STI. The NASA STI Program provides access to the NASA Aeronautics and Space Database and its public interface, the NASA Technical Report Server, thus providing one of the largest collection of aeronautical and space science STI in the world. Results are published in both non-NASA channels and by NASA in the NASA STI Report Series, which includes the following report types:

- **TECHNICAL PUBLICATION.** Reports of completed research or a major significant phase of research that present the results of NASA programs and include extensive data or theoretical analysis. Includes compilations of significant scientific and technical data and information deemed to be of continuing reference value. NASA counterpart of peer-reviewed formal professional papers, but having less stringent limitations on manuscript length and extent of graphic presentations.
- **TECHNICAL MEMORANDUM.** Scientific and technical findings that are preliminary or of specialized interest, e.g., quick release reports, working papers, and bibliographies that contain minimal annotation. Does not contain extensive analysis.
- **CONTRACTOR REPORT.** Scientific and technical findings by NASA-sponsored contractors and grantees.

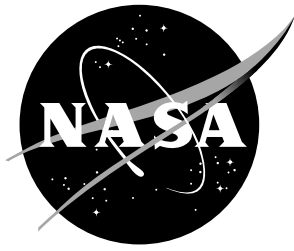
- **CONFERENCE PUBLICATION.** Collected papers from scientific and technical conferences, symposia, seminars, or other meetings sponsored or co-sponsored by NASA.
- **SPECIAL PUBLICATION.** Scientific, technical, or historical information from NASA programs, projects, and missions, often concerned with subjects having substantial public interest.
- **TECHNICAL TRANSLATION.** English-language translations of foreign scientific and technical material pertinent to NASA's mission.

Specialized services also include organizing and publishing research results, distributing specialized research announcements and feeds, providing information desk and personal search support, and enabling data exchange services.

For more information about the NASA STI Program, see the following:

- Access the NASA STI program home page at <http://www.sti.nasa.gov>
- E-mail your question to help@sti.nasa.gov
- Phone the NASA STI Information Desk at 757-864-9658
- Write to:
NASA STI Information Desk
Mail Stop 148
NASA Langley Research Center
Hampton, VA 23681-2199

NASA/TM-20210010505



Mathematical Model Development and Experimental Verification of Electromagnetic Force Actuators for use in Space Applications

Robert C. Youngquist

NASA, Applied Physics Laboratory, Kennedy Space Center, Florida

Mark A. Nurge

NASA, Applied Physics Laboratory, Kennedy Space Center, Florida

Katherine T. Wilson

Cornell University, Sibley School of Mechanical and Aerospace Engineering, Ithaca, New York

National Aeronautics and
Space Administration

John F. Kennedy Space Center
Kennedy Space Center, Florida, 32899

March 2021

Acknowledgments

The authors would like to thank and acknowledge the National Aeronautics and Space Administration Space Technology Research Fellowship Grant 80NSSC18K1166 which provided support for the work of Katherine T. Wilson. Ms. Wilson is a PhD student at Cornell University under the guidance of Professor Mason Peck. We would also like to thank Professor Peck for his insightful discussions and support throughout the project.

The use of trademarks or names of manufacturers in this report is for accurate reporting and does not constitute an official endorsement, either expressed or implied, of such products or manufacturers by the National Aeronautics and Space Administration.

Available from:

NASA STI Program / Mail Stop 148
NASA Langley Research Center
Hampton, VA 23681-2199
Fax: 757-864-6500

Abstract

This technical memorandum shows the development of the mathematics needed to model several types of electromagnetic force actuators that may be of interest for use in space applications. The actuators described are capable of providing attractive, repulsive, and longitudinal forces between the actuator and a variety of metal surfaces. Potential applications for these propellant free actuators include spacecraft docking, in-space fabrication, robotic spacecraft inspection and servicing, deflection of metallic debris, and interaction with iron core asteroids (e.g., landing, repelling, and relocating).

Contents

1	Overview and Purpose	8
2	Magnetic Force Actuators - Electromagnet Coils and their Eddy-Current Interactions with Conductive Targets	9
2.1	Single Electromagnetic Coil	9
2.1.1	Problem Setup	9
2.1.2	The Magnetic Vector Potential for an Isolated Coil	9
2.1.3	Force on the Coil	12
2.2	Single Coil Facing a Conductive Slab	13
2.2.1	The Magnetic Vector Potential for a Coil Facing a Conductive Slab	13
2.2.2	The Force on the Coil	16
2.2.3	Mathematica Repulsive Force Simulation	17
2.3	Two Coils Facing a Conductive Slab	18
2.3.1	Problem Setup	18
2.3.2	Longitudinal Force on the Second Coil	18
2.3.3	Mathematica Simulation of Longitudinal Force in a Linear Induction Motor	21
2.3.4	\hat{z} Directed Force on the Second Coil	22
2.3.5	Mathematica Simulation of Repulsive Force in a Linear Induction Motor	25
2.3.6	Comparison of Linear Induction Motor Forces using a Mathematica Simulation and a COMSOL Model	27
2.4	One Coil Facing a Conductive Slab with a Time Varying/ Pulsed Current	27
2.5	Multi-turn Coil Facing a Conductive Slab with a Time Varying/ Pulsed Current	31
2.6	Electromagnetic coil surrounding an electrically conductive cylinder	32
2.6.1	Problem Setup	32
2.6.2	Oscillating Current and Infinite Length Rod	32
2.6.3	The Magnetic Vector Potential Including the Rod	33
2.6.4	The Force on the Cylinder	36
2.6.5	The Magnetic Field	37
2.6.6	Comments	37
3	Magnetic Force Actuators - Electromagnet Coils and their Eddy-Current Interactions with Conductive and Ferromagnetic Targets	39
3.1	Single Coil Facing a Conductive Ferrous Slab	40
3.1.1	The Magnetic Vector Potential for a Coil Facing a Conductive Ferrous Slab	40
3.1.2	The Force on the Coil	44
3.1.3	Mathematica and COMSOL Force Models for a Coil Facing a Ferrous Slab	45
3.2	Single Coil Facing a Stack of Two Conductive and/ or Ferrous Slabs	46

3.2.1	The Vector Potential and Force on the Coil	46
3.2.2	Mathematica and COMSOL Force Models for a Coil Facing a Conductive Slab Over a Ferrous Slab	49
3.3	Two Coils Facing a Stack of Two Conductive and/ or Ferrous Slabs	50
3.3.1	Problem Setup and Force Solution	50
3.3.2	Mathematica Model of LIM Longitudinal and Axial Forces .	51
3.3.3	Comparison of Linear Induction Motor Forces using a Math- ematica Simulation and a COMSOL Model for an Aluminum Slab on Top of a Ferrous Slab	52
4	AC Modulated Electrostatic Force Actuator	54
4.1	Force Between Plates of a Parallel Plate Capacitor	54
4.2	Electrostatic Force Experiment	55
4.2.1	Test Description	55
4.2.2	Moment of Inertia Computation for Test Fixture	57
4.2.3	Test Results	59
4.3	Plasma Shielding	61
4.4	Plasma Test	63
4.4.1	Test Description	63
4.4.2	Equipment List	63
4.4.3	Test Configuration with Transformer	64
4.4.4	Test Configuration with High-Voltage DC-DC Converter . . .	64
4.4.5	Test Plan	66
4.4.6	Test Results	68
4.4.7	Discussion of Results	71
5	Conclusions	75
6	Appendix A - COMSOL Model for a Linear Induction Motor In- teracting with and Aluminum Slab and an Aluminum Slab on top of an Iron Slab - Longitudinal Force	78
7	Appendix B - COMSOL Model for a Linear Induction Motor In- teracting with and Aluminum Slab and an Aluminum Slab on top of an Iron Slab - Repulsive Force	94

List of Figures

1	A magnetic coil of radius r , at a distance d above a conducting sheet of thickness s , is shown with a cylindrical coordinate system.	10
2	The plot for the force between an AC driven coil with 320 Amps (136 mm diameter) and an 1.5 mm thick aluminum plate.	18
3	Two coils, one a drive coil and one under evaluation, are placed facing a conductive sheet. Both cylindrical and Cartesian coordinates are shown.	19
4	Four coil linear induction motor model with varying amounts of overlap between adjacent coils	22
5	Four coil linear induction motor model with varying phase between adjacent coils	23
6	The two loops are shown so that the relationship between $d\vec{l}$ and $B_\rho\hat{\rho}$ can be seen.	23
7	Plots showing the lateral (blue) and repulsive (red) forces for different amount of coil overlap. The left hand side shows the forces over a range of 0-2 kHz while the right side zooms in on the potentially more useful region where the lateral force exceeds the repulsive force. From top to bottom, the first pair of plots is for $b=r/4$, the 2nd set is for $b=4/2$, and the last pair is for $b=r$	26
8	Plots showing a comparison between the analytical model and a COMSOL model when used to compute the longitudinal (top) and repulsive (bottom) forces with an aluminum slab for a four coil LIM driven in quadrature with a coil overlap equal to the radius. Slight differences occur due to the discrete nature of the finite elements used in the COMSOL model.	28
9	Plots showing a comparison between the analytical model and a COMSOL model when used to compute the repulsive forces between a copper slab and pulsed current loop.	30
10	Plots showing the repulsive forces between a solenoid and a copper slab for four different separation distances. The excitation current pulse is the same as shown in Figure 9.	32
11	Force plots versus frequency for a small loop (1.5 cm radius) with a cylinder sitting on the plane of the loop with radius 1.5 cm and height equal to 3 cm. Two conductivities are shown, aluminum 4×10^7 S/m (the left plot (blue)) and a lower conductivity (right plot (red)) of 4×10^6 S/m.	38
12	Force plots versus frequency for a small loop (1.5 cm radius) with a cylinder sitting on the plane of the loop with radius 1.5 cm and height equal to 0.5, 1.0, 1.5 cm and conductivity of 4×10^6 S/m.	39
13	Semi-log plots showing the repulsive forces between a coil and a ferrous slab for multiple permeabilities over a broad frequency range. The separation between the slab and the face of the solenoid is 1 cm.	46

14	Plots comparing results computed from the analytic expression derived above and a COMSOL FEM model. The models were each used to compute the repulsive forces between a coil and a ferrous slab for multiple permeabilities. The analytic expressions are shown as a continuous line and the COMSOL results are shown as a dashed line. The separation between the slab and the face of the solenoid is 1 cm.	47
15	Semi-log plots showing the repulsive forces between a coil and an aluminum slab over a ferrous slab for multiple permeabilities over a range of frequencies. The separation between the slab and the face of the solenoid is 1 cm.	49
16	Two coils, one a drive coil and one under evaluation, are placed facing a conductive sheet. Both cylindrical and Cartesian coordinates are shown. A second conducting sheet with thickness s_2 is added behind the first. Additionally, both sheets are allowed to vary in permeability.	50
17	The longitudinal and z axis forces for a LIM facing an aluminum slab over an iron slab. The longitudinal force about doubles as μ_r approaches the value for iron of 1000, while the peak repulsive forces converge on the same value, regardless of μ_r	51
18	A zoomed in plot of the longitudinal and z axis forces for a LIM facing an aluminum slab over an iron slab. Note that the z axis force is zero at around 70 Hz when $\mu_r = 1000$, the case for iron. At 70 Hz, the longitudinal force is still large and the lack of forces in the \hat{z} direction allows for cross plane motion without requiring another compensating actuator. If the frequency is allowed to vary between 30-170 Hz, up to 200 mN of attractive or repulsive force can be added to the longitudinal force.	52
19	Plots showing a comparison between the analytical model and a COMSOL model when used to compute the longitudinal (top) and repulsive (bottom) forces with an aluminum slab over an iron slab for a four coil LIM driven in quadrature with a coil overlap equal to the radius. Slight differences occur due to the discrete nature of the finite elements used in the COMSOL model.	53
20	Computed electrostatic attractive force magnitude for a 15.2 cm on a side square plate charged with a 4242 V_{rms} source opposite an infinite conductor as a function of separation distance.	55
21	Electrostatic attraction test configuration showing a mobile balanced by two square plates. An optical displacement sensor is used to measure the movement of the plate on the left. The mobile servicing spacecraft is modeled by the parallel plate capacitor on the right hand side.	56
22	Drawing of test fixture with one plate removed. The dimensions are given in millimeters and are used to compute the moment of inertia. The thickness of the support frame is 3.11 mm and the thickness of the square plate is 1.54 mm	58

23	A photo showing a linear induction motor test setup for measuring lateral motion and force along with electrostatic actuators above and below the coils. A suspended drag wire is used to provide an adequate source of charge so the mobile can respond to the electrostatic actuators.	59
24	Position vs time data for two electrostatic attraction tests showing predicted data (blue) and actual data (black). The upper plot is for a 10 Hz 2545 V RMS sinusoidal drive signal and the lower plot is for a 10 Hz 4242 V RMS sinusoidal drive signal.	60
25	Block diagram showing test configuration using a step-up transformer to generate the high voltages between the sphere and the ground plane.	64
26	Photos showing test configuration using a step-up transformer to generate the high voltages between the sphere and the ground plane. . .	65
27	Block diagram showing test configuration using a HVM Technology DC-DC converter to generate the high voltages between the sphere and the ground plane.	66
28	Graph showing the displacement as a function of voltage of the sphere starting at 1 cm separation from the ground plane compared to the predicted displacement. Data was generated using the HVA0560 DC-DC converter operating at frequencies between 10-150 Hz in normal atmosphere.	67
29	Graph showing the displacement as a function of voltage of the sphere starting at 1 cm separation from the ground plane using the step-up transformer at 20 kHz	67
30	Photos showing the test configuration at MSFC.	69
31	Plot showing displacement of a sphere starting 1 cm from a ground plane as the voltage on the sphere is increased with a 10 kHz drive frequency in vacuum. The curve for the predicted motion is shown for comparison.	70
32	Plot of points showing displacement of a sphere starting 1 cm from a ground plane as the voltage on the sphere is increased. The points shown are from runs at three different frequencies, 10, 15, and 20 kHz. The curve for the predicted motion is shown for comparison . .	70
33	The photo on the left shows the charged sphere in the presence of the plasma. The glow of a corona discharge is present. The bright spots on the sphere are believed to be electrons punching through the paint to try and neutralize the charge. The photo on the right shows the discoloration to the sphere from the hot spots in the paint that occur from the plasma electrons attempting to neutralize the potential. . .	71
34	Plot of points showing displacement of a sphere starting 1 cm from a ground plane as the voltage on the sphere is increased in the presence of plasma with a Debye length of 4.4 mm. The points shown are from runs at two different frequencies, 10 and 20 kHz. The curve for the predicted motion is shown for comparison	72

35 Plot of points showing displacement of a sphere starting 1 cm from a ground plane as the voltage on the sphere is increased in the presence of plasma with a Debye length of 4.0 mm. The points shown are from runs at various frequencies between 1-20 kHz. The curve for the predicted motion is shown for comparison 73

1 Overview and Purpose

This technical memorandum shows the development of the mathematics needed to model several types of electromagnetic force actuators that may be of interest for use in space applications. The actuators described are capable of providing attractive, repulsive, and longitudinal forces between the actuator and a variety of metal surfaces. Potential applications for these propellant free actuators include spacecraft docking, in-space fabrication, robotic spacecraft inspection and servicing, deflection of metallic debris, and interaction with iron core asteroids (e.g., landing, repelling, and relocating).

The majority of the document focuses on the interactions of electromagnets (air coils driven with alternating currents (AC)) and conductive metals, both non-magnetic and ferromagnetic. An AC coil located in a parallel plane to the surface of a conductive plate generates eddy currents in the plate that result in a repulsive force between the two. If that conductive plate has a relative permeability greater than one, attractive forces dominate with direct currents (DC) and for low frequency AC, but then transition to repulsive forces as the frequency of the drive current is increased. Adding a conductive plate over a ferromagnetic plate makes this transition occur at lower frequencies compared to a ferromagnetic plate alone. Configuring multiple overlapping coils in the same plane and driving the currents with an advancing or retarding phase (e.g., in quadrature) results in longitudinal force generation. Coils used in this way form what is often referred to as a linear induction motor. Each of these configurations are explored in detail. Examples are provided to illustrate the force values obtained for different cases, computed directly from the math models. In several cases, finite element models were developed in COMSOL to serve as an independent check on the theory. Data from relevant experiments is presented where possible. Additionally, a few sections include analysis of coils driven with a general time-varying current to aid in determining the forces generated in pulsed current applications.

A non-magnetic method of attraction is described by using a series of plates to induce mirror charges in the conductive plate. Since part of the original purpose for this work was to consider servicing spacecraft for use on the outside of the International Space Station (ISS), the effect the ionosphere will have on such a system needed to be considered. Details are provided about the ionosphere and testing conducted using this electrostatic method. An important result showed that by using sufficient charge and modulating the polarity of the drive plates, it is possible to operate at distances beyond the Debye length without adversely affecting the attractive force.

2 Magnetic Force Actuators - Electromagnet Coils and their Eddy-Current Interactions with Conductive Targets

This section presents the mathematics to compute the magnetic field and vector potential for a loop or current and then looks at the eddy currents formed in a conducting slab parallel to the current loop. These solutions are then used to predict the forces between the eddy currents and single and then multiple loops. After developing the math for an isolated current loop, the case of a single loop opposite a conductive slab is presented, predicting the repulsive force generated when the loop is driven with an alternating current. The next case describes the forces generated when two current loops face the slab and are driven with alternating currents at the same frequency but a separation in phase. In this case, there are translational (longitudinal) forces generated (the basis for a linear induction motor) and repulsive forces.

2.1 Single Electromagnetic Coil

2.1.1 Problem Setup

Assume a single current loop, or coil, of radius r is oriented parallel to a conducting slab of thickness s and infinite extent as shown in Figure 16. The coil is a distance d from the surface of the slab. Place a cylindrical coordinate system on the surface of the slab, with the origin aligned with the center-line of the loop and located on the surface of the slab closest to the coil.

The coil is driven with a time varying current, $I(t) = I \cos \omega t$, where $\omega = 2\pi f$ is the angular frequency and where, without loss of generality, a cosine time dependence has been assumed. It is assumed that the current is not affected by coupling with the plate eddy currents. A more accurate analysis would have the coil driven with a power supply of known impedance where the impact of the back electromotive force (EMF) on the coil current could be modeled. The slab is assumed to have conductivity, σ and be non-magnetic $\mu_r = 1$.

2.1.2 The Magnetic Vector Potential for an Isolated Coil

Several authors have considered the problem of a current loop located over an infinite slab of material [1–6]. Most were concerned with eddy current testing and could assume high current frequencies such that even a thin sheet of metal would look like an infinite slab (the skin depth of aluminum at 1 kHz is only 2.7 mm and at 1 MHz it is only 85 microns). All of them developed their solutions by solving for the magnetic vector potential, \vec{A} , and that same approach is taken here.

Before introducing the complexities of the conductive slab it is worthwhile to start with just an isolated coil. The non-homogeneous wave equation for \vec{A} , is

$$\nabla^2 \vec{A} - (1/c^2) \frac{\partial^2 \vec{A}}{\partial t^2} = -\mu_0 \vec{J}, \quad (1)$$

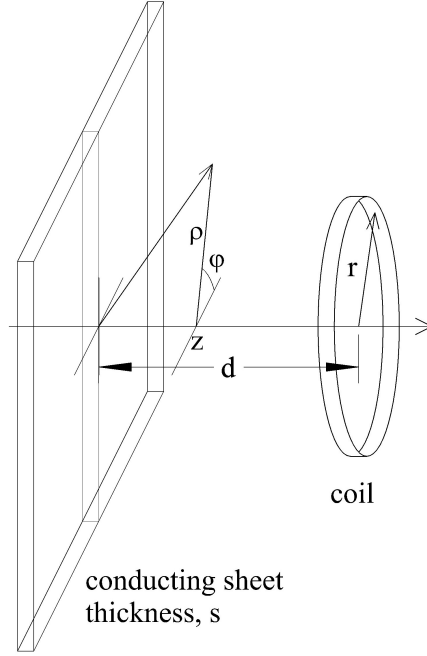


Figure 1. A magnetic coil of radius r , at a distance d above a conducting sheet of thickness s , is shown with a cylindrical coordinate system.

where \vec{J} is the current density. We limit our maximum frequency to about 10 kHz and our maximum length or size to one meter. Consequently, the time derivative has a maximum factor about 4×10^{-8} times smaller than the spatial derivative and can be dropped, leaving

$$\nabla^2 \vec{A} = -\mu_0 \vec{J}. \quad (2)$$

The current density in the coil is given by $\vec{J} = I(t)\delta(\rho - r)\delta(z - d)\hat{\phi}$, i.e. there is only current within the loop which is assumed to be infinitesimal in size. Since the current only points in the $\hat{\phi}$ direction, so does the vector potential, and recalling the problem has cylindrical symmetry (i.e. no ϕ dependence) allows the vector potential to be written in the form, $\vec{A} = A(\rho, z, t)\hat{\phi}$. Then, assuming a Lorentz Gauge,

$$\nabla \cdot \vec{A} + \frac{1}{c^2} \frac{\partial V}{\partial t} = 0, \quad (3)$$

we see that $\nabla \cdot \vec{A}$ can be assumed to be zero because at low frequency the change in potential divided by c^2 is very small. These two results allow the vector Laplacian to be replaced by a double curl and allows the vector differential equation to reduce to a scalar differential equation (taking only the $\hat{\phi}$ direction)

$$\nabla^2 \vec{A} = -\nabla \times \nabla \times \vec{A} = \left(\frac{\partial^2 A}{\partial \rho^2} + \frac{\partial^2 A}{\partial z^2} + \frac{1}{\rho} \frac{\partial A}{\partial \rho} - \frac{A}{\rho^2} = -\mu_0 J \right) \hat{\phi}. \quad (4)$$

Now, assuming separation of variables, we write $A(\rho, z) = A_\rho(\rho)A_z(z)$ and this

equation, after dividing by $A_\rho(\rho)A_z(z)$, becomes

$$(A''_\rho + A'_\rho/\rho - A_\rho/\rho^2)/A_\rho + A''_z/A_z = -\mu_0 J/(A_\rho A_z) \quad (5)$$

where primes indicate differentiation and where the explicit variable dependence has been dropped since the subscripts provide that information.

First solve the problem for all space other than the current loop (i.e., set the differential equation equal to zero). Doing this yields

$$(A''_\rho + A'_\rho/\rho - A_\rho/\rho^2)/A_\rho = -\alpha^2 = -A''_z/A_z, \quad (6)$$

where α is an arbitrary constant. Solving this yields, for a particular α , the solution

$$A(\rho, z) = (C_1 e^{\alpha z} + C_2 e^{-\alpha z}) (C_3 J_1(\alpha \rho) + C_4 Y_1(\alpha \rho)), \quad (7)$$

i.e., a product of exponentials and Bessel functions. The function $Y_1(\alpha \rho)$ is a Bessel function of the second kind and is not bounded when $\rho = 0$, so $C_4 = 0$. Also, noting that the potential has to stay bounded for large positive or negative values of z around the coil and that the solution is symmetrical about the plane of the coil, i.e., if we let $z \rightarrow z - d$ then $C_1 = C_2$, we can write the solution as

$$A(\rho, z) = \begin{cases} \int_0^\infty C(\alpha) e^{\alpha d} e^{-\alpha z} J_1(\alpha \rho) d\alpha, & z > d \\ \int_0^\infty C(\alpha) e^{-\alpha d} e^{\alpha z} J_1(\alpha \rho) d\alpha, & z \leq d. \end{cases} \quad (8)$$

The solution is symmetrical about d and the parameters C_1, C_2 , and C_3 have been absorbed into the function $C(\alpha)$.

The next step is to find the function $C(\alpha)$ by re-inserting the current. Consider a location $(r, d - \epsilon)$ where ϵ is very small and a symmetric location on the other side of the coil $(r, d + \epsilon)$. By symmetry we expect the vector potential to have the same value at both of these points, which is verified by examination of the solution above. We also expect the slopes in the $\hat{\rho}$ direction to be the same at these two locations, just on either side of the coil's wire. What is different is the slope in the \hat{z} direction at these two locations. So consider, Eq. 4 with the coil current inserted

$$\frac{\partial^2 A}{\partial \rho^2} + \frac{\partial^2 A}{\partial z^2} + \frac{1}{\rho} \frac{\partial A}{\partial \rho} - \frac{A}{\rho^2} = -\mu_0 I(t) \delta(z - d) \delta(\rho - r). \quad (9)$$

Integrating along a line from $(r, d - \epsilon)$ to $(r, d + \epsilon)$ passes through the coil and begins and ends on locations where the ρ derivatives are equal and cancel, yielding

$$\frac{\partial A}{\partial z} \Big|_{z=d+\epsilon} - \frac{\partial A}{\partial z} \Big|_{z=d-\epsilon} = -\mu_0 I(t) \delta(\rho - r). \quad (10)$$

Substituting in the general solution yields

$$-2 \int_0^\infty C(\alpha) e^{-\alpha \epsilon} J_1(\alpha \rho) \alpha d\alpha = -\mu_0 I(t) \delta(\rho - r). \quad (11)$$

The Bessel function closure relation

$$\int_0^\infty J_1(\beta \rho) J_1(\alpha \rho) \rho d\rho = (1/\alpha) \delta(\beta - \alpha) \quad (12)$$

can be used to simplify the expression above. Multiply both sides by $-\rho J_1(\beta\rho)$ and integrate ρ from 0 to ∞ to obtain

$$\begin{aligned} \int_0^\infty \rho J_1(\beta\rho) 2 \int_0^\infty C(\alpha) e^{-\alpha\epsilon} J_1(\alpha\rho) \alpha d\alpha d\rho &= \int_0^\infty \rho J_1(\beta\rho) \mu_0 I(t) \delta(\rho-r) d\rho \\ 2 \int_0^\infty C(\alpha) e^{-\alpha\epsilon} \delta(\beta-\alpha) d\alpha &= \mu_0 I(t) r J_1(\beta r) \\ 2C(\beta) e^{-\beta\epsilon} &= \mu_0 I(t) r J_1(\beta r) \\ C(\beta) &= \mu_0 I(t) r J_1(\beta r) / 2, \end{aligned} \quad (13)$$

where ϵ has been taken to zero in the final step. So the complete vector potential for a current loop is given by

$$A(\rho, z) = \begin{cases} \frac{1}{2} \int_0^\infty \mu_0 I(t) r e^{\alpha d} e^{-\alpha z} J_1(\alpha r) J_1(\alpha \rho) d\alpha, & z > d \\ \frac{1}{2} \int_0^\infty \mu_0 I(t) r e^{-\alpha d} e^{\alpha z} J_1(\alpha r) J_1(\alpha \rho) d\alpha, & z \leq d. \end{cases} \quad (14)$$

This expression can be converted to an elliptical integral:

$$A(\rho, z) = \frac{\mu_0 I(t) \sqrt{r}}{2\pi \sqrt{k\rho}} (-2E(k) + (2-k)K(k)), \quad (15)$$

where $k = \frac{4r\rho}{(\rho+r)^2 + (z-d)^2}$ using Kausel's paper [7]. This is in agreement with the results on pages 181-182 in Jackson [8], obtained by performing a line integral around the coil loop.

2.1.3 Force on the Coil

Before including the slab, it is worthwhile to consider the mathematics predicting the force the coil exerts on itself. Of course we expect this to yield a net zero force—an object can't make itself move—but by going through this derivation we highlight what terms in the last analysis correspond to coil-coil interaction as opposed to coil-slab interaction. The force on an element of the coil is given by $d\vec{F} = I(t)d\vec{l} \times \vec{B}$. For now only consider the force along the \hat{z} axis, and since $d\vec{l}$ points in the $\hat{\phi}$ direction, only the radial components of the magnetic field contribute, yielding $dF\hat{z} = -IdlB_\rho\hat{z}$. Integrating about the coil's circumference yields

$$F_z = -I2\pi r B_\rho(r, d) = I2\pi r \frac{\partial A(r, d)}{\partial z}. \quad (16)$$

where $B_\rho(r, d)$ is the radial component of the magnetic field on the coil, where $\partial A(r, d)/\partial z$ is determined on the coil, and where the time dependence of the current and fields is not shown. Using the set of equations in Eq. 14, we find

$$\frac{\partial A(\rho, z)}{\partial z} = \begin{cases} -\frac{1}{2} \int_0^\infty \alpha \mu_0 I(t) r e^{\alpha d} e^{-\alpha z} J_1(\alpha r) J_1(\alpha \rho) d\alpha, & z > d \\ \frac{1}{2} \int_0^\infty \alpha \mu_0 I(t) r e^{-\alpha d} e^{\alpha z} J_1(\alpha r) J_1(\alpha \rho) d\alpha, & z < d. \end{cases} \quad (17)$$

Now let $z = d + \epsilon$ when $z > d$ and $z = d - \epsilon$ when $z < d$, which upon substitution gives

$$\begin{aligned}\frac{\partial A(\rho, d + \epsilon)}{\partial z} &= -\frac{1}{2} \int_0^\infty \alpha \mu_0 I(t) r e^{\alpha d} e^{-\alpha(d+\epsilon)} J_1(\alpha r) J_1(\alpha \rho) d\alpha \\ \frac{\partial A(\rho, d - \epsilon)}{\partial z} &= \frac{1}{2} \int_0^\infty \alpha \mu_0 I(t) r e^{-\alpha d} e^{\alpha(d-\epsilon)} J_1(\alpha r) J_1(\alpha \rho) d\alpha.\end{aligned}\quad (18)$$

These two expressions are the negative of each other, so their summation is zero. If we assume the coil has finite thickness then the force on one side of segment of the coil is canceled by the force on the other side, so there is no net force.

2.2 Single Coil Facing a Conductive Slab

2.2.1 The Magnetic Vector Potential for a Coil Facing a Conductive Slab

Inside of the conductive slab the time variation of the vector potential generates an electric field given by $\vec{E} = -\partial \vec{A} / \partial t$. This causes currents to flow by Ohm's Law, $\vec{J} = \sigma \vec{E}$. Using these, the differential equation for the vector potential in the slab becomes

$$\nabla^2 \vec{A} = -\mu_0 \vec{J} = -\mu_0 \sigma \vec{E} = \mu_0 \sigma \frac{\partial \vec{A}}{\partial t}. \quad (19)$$

Now assume the coil current is varying sinusoidally, $I(t) = I \cos(\omega t)$, causing the vector potential to also vary sinusoidally and allowing it to be expressed as

$$\vec{A}(\rho, z, t) = \frac{\vec{A}(\rho, z) e^{i\omega t} + \vec{A}^*(\rho, z) e^{-i\omega t}}{2}. \quad (20)$$

There is a phase difference between the current and the vector potential that will cause $\vec{A}(\rho, z)$ to be complex, but when we calculate forces we will need to multiply the vector potential times the current and this multiplication can only be done between real terms, not complex ones. Consequently, it must be kept in mind that before this multiplication can be performed that the above formula must be used to recover the real version of the vector potential. So using $\vec{A}(\rho, z) e^{i\omega t}$ as the form for the vector potential, the differential equation in the slab becomes

$$\nabla^2 \vec{A} = -\nabla \times \nabla \times \vec{A} = \frac{\partial^2 \vec{A}}{\partial \rho^2} + \frac{\partial^2 \vec{A}}{\partial z^2} + \frac{1}{\rho} \frac{\partial \vec{A}}{\partial \rho} - \frac{\vec{A}}{\rho^2} = i\omega \mu_0 \sigma \vec{A}. \quad (21)$$

The coefficient $\omega \mu_0 \sigma$ can be significant. Aluminum has a conductivity of about 4×10^7 A/(V-m) and if the frequency is 50 Hz this coefficient is about 16,000 m⁻². So the term on the right of this equation must be kept through the analysis.

As was the case with the isolated coil, the currents and therefore the magnetic vector potential are only in the $\hat{\phi}$ direction. So, $\vec{A} = A(\rho, z) \hat{\phi}$, allowing Eq. 21 to be written in scalar form. Then, using separation of variables, $A(\rho, z) = A_\rho(\rho) A_z(z)$, yields the differential equation

$$\begin{aligned}(A_\rho'' + A_\rho'/\rho - A_\rho/\rho^2)/A_\rho + A_z''/A_z &= i\omega \mu_0 \sigma \\ (A_\rho'' + A_\rho'/\rho - A_\rho/\rho^2)/A_\rho = -\alpha^2 = -A_z''/A_z + i\omega \mu_0 \sigma.\end{aligned}\quad (22)$$

Solving this yields the solution for a specific α

$$A(\rho, z) = \left(D e^{z\sqrt{\alpha^2+i\omega\mu_0\sigma}} + E e^{-z\sqrt{\alpha^2+i\omega\mu_0\sigma}} \right) J_1(\alpha\rho), \quad (23)$$

and the general solution for the vector potential within the slab

$$A(\rho, z) = \int_0^\infty \left(D(\alpha) e^{z\sqrt{\alpha^2+i\omega\mu_0\sigma}} + E(\alpha) e^{-z\sqrt{\alpha^2+i\omega\mu_0\sigma}} \right) J_1(\alpha\rho) d\alpha. \quad (24)$$

Using the expressions obtained for the isolated coil, there are now four general solutions, for four different regions of space.

$$A(\rho, z) = \begin{cases} \int_0^\infty C(\alpha) e^{\alpha d} e^{-\alpha z} J_1(\alpha\rho) d\alpha, & z > d \\ \int_0^\infty \left(F(\alpha) e^{\alpha d} e^{-\alpha z} + G(\alpha) e^{-\alpha d} e^{\alpha z} \right) J_1(\alpha\rho) d\alpha, & 0 < z < d \\ \int_0^\infty \left(D(\alpha) e^{z\sqrt{\alpha^2+i\omega\mu_0\sigma}} + E(\alpha) e^{-z\sqrt{\alpha^2+i\omega\mu_0\sigma}} \right) J_1(\alpha\rho) d\alpha, & -s < z < 0 \\ \int_0^\infty H(\alpha) e^{\alpha z} J_1(\alpha\rho) d\alpha, & z < -s \end{cases} \quad (25)$$

Across each interface the vector potential is continuous and, since the slab is assumed to not be magnetic ($\mu_r = 1$), the tangential components of the magnetic field, $H_\rho = -\partial A/\partial z$, are continuous on each slab interface. This yields five boundary conditions for the six unknown functions. The sixth boundary condition comes from the coil itself. Starting with the continuity condition and letting $\alpha_1 = \sqrt{\alpha^2 + i\omega\mu_0\sigma}$ (we assume α_1 is in the quadrant where both its real and imaginary components are greater than zero) we obtain

$$\begin{aligned} C(\alpha) &= F(\alpha) + G(\alpha) \\ F(\alpha) e^{\alpha d} + G(\alpha) e^{-\alpha d} &= D(\alpha) + E(\alpha) \\ D(\alpha) e^{-\alpha_1 s} + E(\alpha) e^{\alpha_1 s} &= H(\alpha) e^{-\alpha s}. \end{aligned} \quad (26)$$

The two magnetic field conditions across the slab surfaces yield

$$\begin{aligned} -\alpha F(\alpha) e^{\alpha d} + \alpha G(\alpha) e^{-\alpha d} &= \alpha_1 D(\alpha) + \alpha_1 E(\alpha) \\ \alpha_1 D(\alpha) e^{-\alpha_1 s} - \alpha_1 E(\alpha) e^{\alpha_1 s} &= \alpha H(\alpha) e^{-\alpha s}. \end{aligned} \quad (27)$$

Across the coil we have

$$\frac{\partial A(\rho, z, t)}{\partial z} \Big|_{z=d+\epsilon} - \frac{\partial A(\rho, z, t)}{\partial z} \Big|_{z=d-\epsilon} = -\mu_0 I(t) \delta(\rho - r). \quad (28)$$

But we need a boundary condition form for $A(\rho, z)$, i.e., with the time dependence removed. Using the expression for $A(\rho, z, t)$ given in Eq. 20 and expanding $I(t) = I \cos(\omega t)$ allows such a condition to be found:

$$\begin{aligned} \frac{\partial \left(A(\rho, z) e^{i\omega t} + A^*(\rho, z) e^{-i\omega t} \right)}{2\partial z} \Big|_{z=d+\epsilon} - \frac{\partial \left(A(\rho, z) e^{i\omega t} + A^*(\rho, z) e^{-i\omega t} \right)}{2\partial z} \Big|_{z=d-\epsilon} \\ = -\mu_0 I \frac{e^{i\omega t} + e^{-i\omega t}}{2} \delta(\rho - r). \end{aligned} \quad (29)$$

Rearranging terms to separate the time dependence gives:

$$\left(\frac{\partial A(\rho, z)}{\partial z} \Big|_{z=d+\epsilon} - \frac{\partial A(\rho, z)}{\partial z} \Big|_{z=d-\epsilon} \right) \frac{e^{i\omega t}}{2} + cc = -\mu_0 I \frac{e^{i\omega t}}{2} \delta(\rho - r) + cc, \quad (30)$$

where cc is the complex conjugate of each side of the equation. This can be further simplified to a time independent form:

$$\frac{\partial A(\rho, z)}{\partial z} \Big|_{z=d+\epsilon} - \frac{\partial A(\rho, z)}{\partial z} \Big|_{z=d-\epsilon} = -\mu_0 I \delta(\rho - r). \quad (31)$$

Substituting this into the first two general solutions in Eq. 24 gives:

$$\int_0^\infty (-C(\alpha) + G(\alpha)) e^{-\alpha\epsilon} + F(\alpha) e^{\alpha\epsilon} J_1(\alpha\rho) \alpha d\alpha = -\mu_0 I \delta(\rho - r). \quad (32)$$

Now use the orthogonality integral relationship $\int_0^\infty J_1(\beta\rho) J_1(\alpha\rho) \rho d\rho = (1/\alpha) \delta(\beta - \alpha)$ to obtain:

$$\begin{aligned} \int_0^\infty J_1(\beta\rho) \int_0^\infty (-C(\alpha) + G(\alpha)) e^{-\alpha\epsilon} + F(\alpha) e^{\alpha\epsilon} J_1(\alpha\rho) \alpha d\alpha \rho d\rho \\ = - \int_0^\infty J_1(\beta\rho) \mu_0 I \delta(\rho - r) \rho d\rho. \end{aligned} \quad (33)$$

This then reduces to

$$\int_0^\infty (-C(\alpha) + G(\alpha)) e^{-\alpha\epsilon} + F(\alpha) e^{\alpha\epsilon} \delta(\beta - \alpha) d\alpha = -J_1(\beta r) r \mu_0 I. \quad (34)$$

Evaluating the final integral results in

$$-(C(\beta) + G(\beta)) e^{-\beta\epsilon} + F(\beta) e^{\beta\epsilon} = -J_1(\beta r) r \mu_0 I. \quad (35)$$

Letting ϵ go to zero and changing variables gives the last expression needed to find the full solution:

$$C(\alpha) + G(\alpha) - F(\alpha) = J_1(\alpha r) r \mu_0 I. \quad (36)$$

Solving these six equations for the coefficient functions yields:

$$\begin{aligned} C(\alpha) &= \mu_0 I r \frac{J_1(\alpha r)}{2} \left(1 + \frac{(\alpha^2 - \alpha_1^2) e^{-2\alpha d} (e^{\alpha_1 s} - e^{-\alpha_1 s})}{(\alpha + \alpha_1)^2 e^{\alpha_1 s} - (\alpha - \alpha_1)^2 e^{-\alpha_1 s}} \right) \\ F(\alpha) &= \mu_0 I r \frac{J_1(\alpha r)}{2} \left(\frac{(\alpha^2 - \alpha_1^2) e^{-2\alpha d} (e^{\alpha_1 s} - e^{-\alpha_1 s})}{(\alpha + \alpha_1)^2 e^{\alpha_1 s} - (\alpha - \alpha_1)^2 e^{-\alpha_1 s}} \right) \\ G(\alpha) &= \mu_0 I r \frac{J_1(\alpha r)}{2} \\ D(\alpha) &= \mu_0 I r J_1(\alpha r) \left(\frac{\alpha(\alpha_1 + \alpha) e^{\alpha_1 s - \alpha d}}{(\alpha + \alpha_1)^2 e^{\alpha_1 s} - (\alpha - \alpha_1)^2 e^{-\alpha_1 s}} \right) \\ E(\alpha) &= \mu_0 I r J_1(\alpha r) \left(\frac{\alpha(\alpha_1 - \alpha) e^{-\alpha_1 s - \alpha d}}{(\alpha + \alpha_1)^2 e^{\alpha_1 s} - (\alpha - \alpha_1)^2 e^{-\alpha_1 s}} \right) \\ H(\alpha) &= \mu_0 I r J_1(\alpha r) \left(\frac{2\alpha\alpha_1 e^{\alpha(s-d)}}{(\alpha + \alpha_1)^2 e^{\alpha_1 s} - (\alpha - \alpha_1)^2 e^{-\alpha_1 s}} \right) \end{aligned} \quad (37)$$

These expressions combined with Eq. 25 yield the complete description of the time-independent portion of the vector potential. If $\alpha_1 = \alpha$, i.e., the slab is non-conducting or the frequency is very small, these expressions reduce to the same vector potential as found for the isolated coil.

2.2.2 The Force on the Coil

Now consider the force on the coil due to the presence of the slab. The force on an element of the coil is given by $d\vec{F} = I(t)d\vec{l} \times \vec{B}$. Since we are only interested in the total force along the z axis, and since $d\vec{l}$ points in the $\hat{\phi}$ direction, only the radial components of the magnetic field contribute, resulting in $dF\hat{z} = -I(t)dlB_\rho\hat{z}$. Integrating around the coil's circumference yields:

$$\vec{F} = -I(t)2\pi r B_\rho(r, d, t)\hat{z} = I(t)2\pi r \frac{\partial A(r, d, t)}{\partial z} \hat{z}, \quad (38)$$

where $B_\rho(r, d, t)$ is the radial component of the magnetic field on the coil and where $\partial A(r, d, t)/\partial z$ is the derivative of A with respect to z and evaluated at $\rho = r$ and $z = d$. From Eq. 20

$$\frac{\partial A(r, d, t)}{\partial z} = \left(\frac{\partial A(r, d)}{\partial z} e^{i\omega t} + \frac{\partial A^*(r, d)}{\partial z} e^{-i\omega t} \right) / 2. \quad (39)$$

This results in a force on the coil given by

$$\vec{F} = I \cos(\omega t) 2\pi r \left(\frac{\partial A(r, d)}{\partial z} e^{i\omega t} + \frac{\partial A^*(r, d)}{\partial z} e^{-i\omega t} \right) / 2 \hat{z}. \quad (40)$$

We are only interested in the steady state force so we can average the time dependence over a cycle which will leave

$$\vec{F}_{avg} = I\pi r \left(\frac{\partial A(r, d)}{\partial z} + \frac{\partial A^*(r, d)}{\partial z} \right) / 2 \hat{z}. \quad (41)$$

From the above expressions we know that

$$A(\rho, z) = \begin{cases} \int_0^\infty C(\alpha) e^{\alpha d} e^{-\alpha z} J_1(\alpha \rho) d\alpha, & z > d \\ \int_0^\infty (F(\alpha) e^{\alpha d} e^{-\alpha z} + G(\alpha) e^{-\alpha d} e^{\alpha z}) J_1(\alpha \rho) d\alpha, & 0 < z < d. \end{cases} \quad (42)$$

Taking the derivatives yields,

$$\frac{\partial A(\rho, z)}{\partial z} = \begin{cases} \int_0^\infty -\alpha C(\alpha) e^{\alpha d} e^{-\alpha z} J_1(\alpha \rho) d\alpha, & z > d \\ \int_0^\infty (-\alpha F(\alpha) e^{\alpha d} e^{-\alpha z} + \alpha G(\alpha) e^{-\alpha d} e^{\alpha z}) J_1(\alpha \rho) d\alpha, & 0 < z < d. \end{cases} \quad (43)$$

Now let $z = d + \epsilon$ when $z > d$ and $z = d - \epsilon$ when $0 < z < d$ to obtain

$$\begin{aligned} \frac{\partial A(\rho, d + \epsilon)}{\partial z} &= \int_0^\infty -\alpha C(\alpha) e^{-\alpha \epsilon} J_1(\alpha \rho) d\alpha \\ \frac{\partial A(\rho, d - \epsilon)}{\partial z} &= \int_0^\infty (-\alpha F(\alpha) e^{\alpha \epsilon} + \alpha G(\alpha) e^{-\alpha \epsilon}) J_1(\alpha \rho) d\alpha. \end{aligned} \quad (44)$$

Now use the expression $C(\alpha) = F(\alpha) + G(\alpha)$

$$\begin{aligned}\frac{\partial A(\rho, d + \epsilon)}{\partial z} &= \int_0^\infty (-\alpha F(\alpha)e^{-\alpha\epsilon} - \alpha G(\alpha)e^{-\alpha\epsilon}) J_1(\alpha\rho) d\alpha \\ \frac{\partial A(\rho, d - \epsilon)}{\partial z} &= \int_0^\infty (-\alpha F(\alpha)e^{\alpha\epsilon} + \alpha G(\alpha)e^{-\alpha\epsilon}) J_1(\alpha\rho) d\alpha.\end{aligned}\quad (45)$$

The $G(\alpha)$ terms correspond to the vector potential gradient due to the current in the coil itself. As was discussed earlier, these two terms are of opposite sign and cancel each other. The remaining term corresponds to the vector potential gradient from the slab and is given by

$$\frac{\partial A(\rho, d)}{\partial z} = \int_0^\infty -\alpha F(\alpha) J_1(\alpha\rho) d\alpha. \quad (46)$$

On the coil itself, this becomes

$$\frac{\partial A(r, d)}{\partial z} = \int_0^\infty -\alpha F(\alpha) J_1(\alpha r) d\alpha. \quad (47)$$

Combining this with Eq. 41, the force on the coil due to the slab is given by

$$\vec{F}_{avg} = -\frac{I\pi r}{2} \int_0^\infty \alpha (F(\alpha) + F^*(\alpha)) J_1(\alpha r) d\alpha \hat{z}, \quad (48)$$

where

$$F(\alpha) = \mu_0 I r \frac{J_1(\alpha r)}{2} \left(\frac{(\alpha^2 - \alpha_1^2) e^{-2\alpha d} (e^{\alpha_1 s} - e^{-\alpha_1 s})}{(\alpha + \alpha_1)^2 e^{\alpha_1 s} - (\alpha - \alpha_1)^2 e^{-\alpha_1 s}} \right) \quad (49)$$

and

$$\alpha_1 = \sqrt{\alpha^2 + i\omega\mu_0\sigma}. \quad (50)$$

If the slab becomes nonconducting, or if the frequency is zero, then $\alpha_1 = \alpha$ and the force is zero, as expected. Also, if the thickness of the slab, s , goes to zero then the force becomes zero, again as expected.

2.2.3 Mathematica Repulsive Force Simulation

Wolfram's Mathematica was used to code the result in the previous section to understand the force developed between AC driven coil and a sheet of aluminum. The aluminum was assumed to be 1.5 mm thick with a conductivity of 3.77×10^7 S/m. The coil modeled contains 320 turns with 1 Amp of current and is assumed to be infinitely thin but has a 136 mm diameter. The frequency was varied and the the distance between the coil and plate was varied between 0.2-1.0 cm. The resulting force plots are shown in Figure 2

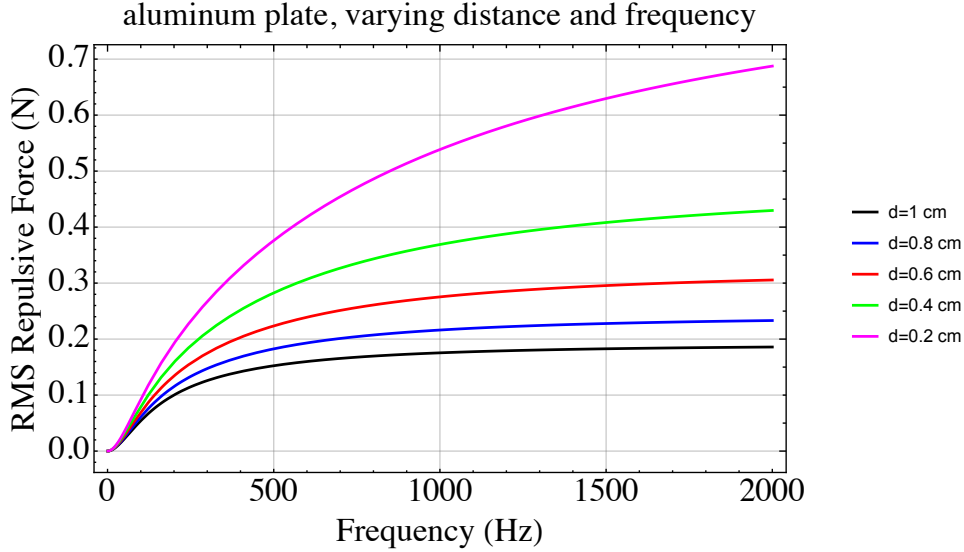


Figure 2. The plot for the force between an AC driven coil with 320 Amps (136 mm diameter) and an 1.5 mm thick aluminum plate.

2.3 Two Coils Facing a Conductive Slab

This section develops the math for the addition of a second current loop. The resulting forces can then be summed to achieve the overall forces for a variety of coil configurations including the longitudinal forces for the linear induction motor or the axial forces for a solenoid coil.

2.3.1 Problem Setup

The first current loop, located as in the previous sections, is now considered to be a drive loop that generates the vector potential and the eddy currents in the plate. It is driven with the same current as before, $I(t) = I \cos \omega t$. The second current loop is also driven with an oscillating current of the same frequency, but different phase than the drive coil, $I_2(t) = I_2 \cos(\omega t + \varphi)$ and is not inductively coupled to the first loop, i.e. the power supply can overcome inductive voltages.

The drive coil, has radius r , is centered on the \hat{z} axis a distance d from the near surface of the plate, and faces the plate. The second coil also faces the plate, but is a distance d_2 from the front plate surface. The second coil is radius r_2 and its center is a distance b along the \hat{x} axis from the center of the drive coil as shown in Figure 3

2.3.2 Longitudinal Force on the Second Coil

There will be both longitudinal and \hat{z} directed forces created on the second coil due to its current interacting with the vector potential created by the drive coil and the slab. In this section only the longitudinal force will be found. In practice the total

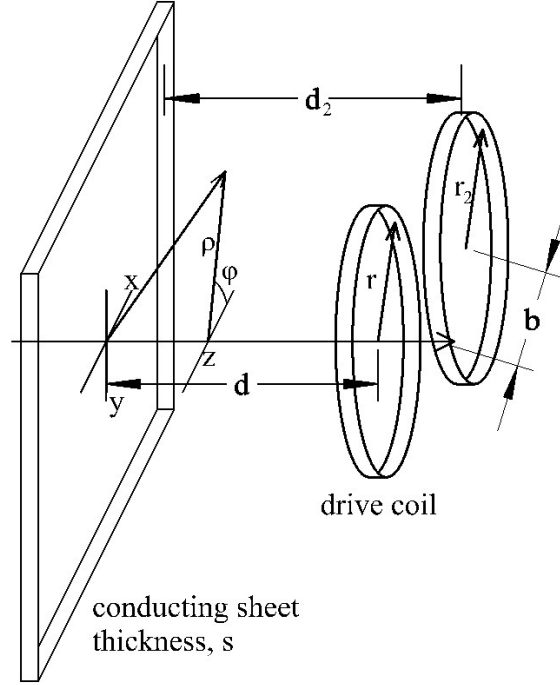


Figure 3. Two coils, one a drive coil and one under evaluation, are placed facing a conductive sheet. Both cylindrical and Cartesian coordinates are shown.

longitudinal force on a number of coils is desired and to find this, the force exerted by each coil on all of the other coils is summed using the results derived below.

The force on an element, $d\vec{l}$, of the second coil is given by

$$d\vec{F} = I_2(t)d\vec{l} \times \vec{B}(\rho, z, t) \quad (51)$$

where the magnetic field, $\vec{B}(\rho, z, t)$ is generated by the currents in the drive coil and in the slab. In this section the \hat{x} directed force is being calculated. The \hat{y} force will total to zero by symmetry and the \hat{z} force will be found in the next section. Since the coil is in an \hat{x} - \hat{y} plane, only the \hat{z} component of the magnetic field contributes to the \hat{x} directed force and only the \hat{y} component of the current contributes. So the differential force equation simplifies to

$$dF_x(x, y, t) = I_2 \cos(\omega t + \varphi) B_z(\rho, z, t) dy. \quad (52)$$

The magnetic field is complex due to phase shifts in time caused by the slab, and can be expressed as

$$B_z(\rho, z, t) = \frac{B_z(\rho, z)e^{i\omega t} + B_z^*(\rho, z)e^{-i\omega t}}{2} \quad (53)$$

substituting this into the force equation and expanding the cosine yields

$$dF_x(x, y, t) = (I_2/4)(e^{i(\omega t + \varphi)} + e^{-i(\omega t + \varphi)}) (B_z(\rho, z)e^{i\omega t} + B_z^*(\rho, z)e^{-i\omega t}) dy. \quad (54)$$

Averaging this over time yields

$$dF_x(x, y) = (I_2/4) (B_z(\rho, z)e^{-i\varphi} + B_z^*(\rho, z)e^{i\varphi}) dy. \quad (55)$$

Since the vector potential points only in the $\hat{\phi}$ direction, i.e., $\vec{A} = A(\rho, z)\hat{\phi}$, the \hat{z} component of the magnetic field is given by

$$B_z(\rho, z) = \frac{1}{\rho} \frac{\partial}{\partial \rho} (\rho A(\rho, z)) \quad (56)$$

$B_z(\rho, z)$ is only needed when $z = d_2$, the plane containing the second coil, and only the component of the vector potential generated by the slab is needed, not the component generated by the drive coil. The drive coil component will generate a force that will be balanced by the force exerted by the second coil on the first, yielding no net force. From the prior development, this component of the vector potential is given by

$$A(\rho, z) = \int_0^\infty F(\alpha) e^{\alpha d} e^{-\alpha z} J_1(\alpha \rho) d\alpha \quad (57)$$

which becomes, when $z = d_2$

$$A(\rho, d_2) = \int_0^\infty F(\alpha) e^{\alpha(d-d_2)} J_1(\alpha \rho) d\alpha \quad (58)$$

so the magnetic field component, $B_z(\rho, d_2)$ is

$$\begin{aligned} B_z(\rho, z) &= \frac{1}{\rho} \frac{\partial}{\partial \rho} \left(\rho \int_0^\infty F(\alpha) e^{\alpha(d-d_2)} J_1(\alpha \rho) d\alpha \right) \\ B_z(\rho, z) &= \int_0^\infty F(\alpha) e^{\alpha(d-d_2)} \frac{1}{\rho} \frac{\partial}{\partial \rho} (\rho J_1(\alpha \rho)) d\alpha \\ B_z(\rho, z) &= \int_0^\infty F(\alpha) e^{\alpha(d-d_2)} J_0(\alpha \rho) \alpha d\alpha \end{aligned} \quad (59)$$

where, from the prior analysis

$$F(\alpha) = \mu_0 I r \frac{J_1(\alpha r)}{2} \left(\frac{(\alpha^2 - \alpha_1^2) e^{-2\alpha d} (e^{\alpha_1 s} - e^{-\alpha_1 s})}{(\alpha + \alpha_1)^2 e^{\alpha_1 s} - (\alpha - \alpha_1)^2 e^{-\alpha_1 s}} \right) \quad (60)$$

where $\alpha_1^2 = \alpha^2 + i\omega\mu_0\sigma$. So the differential force is given by

$$dF_x(x, y) = (I_2/4) \int_0^\infty (F(\alpha) e^{-i\varphi} + F^*(\alpha) e^{i\varphi}) e^{\alpha(d-d_2)} J_0(\alpha \rho) \alpha d\alpha dy. \quad (61)$$

To obtain the total force the differential force is integrated around the upper half of the second coil (and multiplied by 2 to account for the lower half of the coil). The upper half of the coil is described by

$$y^2 + (x - b)^2 = r_2^2 \quad \rightarrow \quad y = \sqrt{r_2^2 - (x - b)^2} \quad b - r_2 \leq x \leq b + r_2 \quad (62)$$

Recalling that $\rho = \sqrt{x^2 + y^2}$, the dy and ρ become

$$dy[x] = \frac{b - x}{\sqrt{r_2^2 - (x - b)^2}} dx \quad \text{and} \quad \rho = \sqrt{r_2^2 - b^2 + 2bx} \quad (63)$$

So the total force on the second coil (including the factor of 2) is given by

$$\begin{aligned} F_x &= 2 \int_{b-r_2}^{b+r_2} dF_x(x, y) \\ F_x &= \int_{b-r_2}^{b+r_2} \frac{I_2}{2} \int_0^\infty (F(\alpha)e^{-i\varphi} + F^*(\alpha)e^{i\varphi}) e^{\alpha(d-d_2)} J_0(\alpha\sqrt{r_2^2 - b^2 + 2bx}) \alpha d\alpha \frac{b - x}{\sqrt{r_2^2 - (x - b)^2}} dx \\ F_x &= \frac{I_2}{2} \int_0^\infty (F(\alpha)e^{-i\varphi} + F^*(\alpha)e^{i\varphi}) e^{\alpha(d-d_2)} \alpha \int_{b-r_2}^{b+r_2} \frac{(b - x) J_0(\alpha\sqrt{r_2^2 - b^2 + 2bx})}{\sqrt{r_2^2 - (x - b)^2}} dx d\alpha \end{aligned} \quad (64)$$

It's worth noting that the $e^{-2\alpha d}$ term from $F(\alpha)$ and the $e^{\alpha(d-d_2)}$ from F_x combine to show that total force drops exponentially according to the total distance of the two coils from the slab. Additionally, if $b = r_2$ then the dx integral can be performed in closed form yielding

$$\int_{b-r_2}^{b+r_2} \frac{(b - x) J_0(\alpha\sqrt{r_2^2 - b^2 + 2bx})}{\sqrt{r_2^2 - (x - b)^2}} dx = \int_0^{2b} \frac{(b - x) J_0(\alpha\sqrt{2bx})}{\sqrt{2bx - x^2}} dx = -b\pi J_1^2(\alpha b) \quad (65)$$

2.3.3 Mathematica Simulation of Longitudinal Force in a Linear Induction Motor

The general solution of the LIM presented above was used to determine the maximum mean force configuration for a four coil motor by varying the overlap of the coils and then the phase. The coils again are 320 Amp loops that are 136 mm in diameter. The first drive coil is assumed to be 1.5 cm from a 1.5 mm thick aluminum plate with a conductivity of 3.77×10^7 S/m. The 2nd coil is assumed to be 3.5 cm from the plate since the two coils can't occupy the same space. The remaining two coils repeat the pattern. The overlap parameter, b , was varied to allow different amounts of overlap while computing the force generated. The model supports allowing the radii of the coils to all be different, but for this example they are all assumed to be equal to r , which is calculated from the diameter mentioned above to be 68 mm. The first set of plots is shown in Figure 4 showing that the maximum

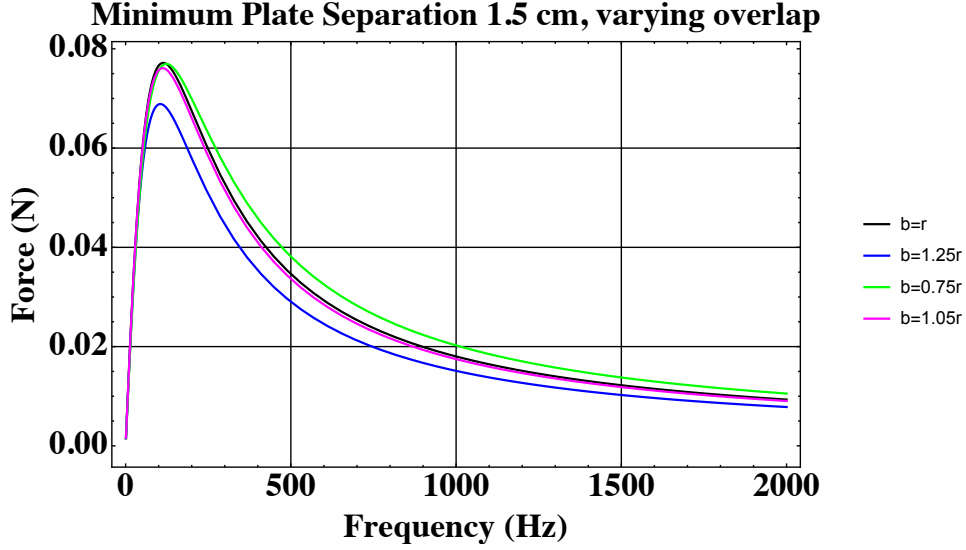


Figure 4. Four coil linear induction motor model with varying amounts of overlap between adjacent coils

mean force is generated for $0.75r \leq b \leq 1.0r$. Other modeling showed that the force drops off for overlaps less than around $0.75r$.

The results of the phase variation are given below in Figure 5. Driving the LIM in quadrature ($\phi = \pi/2$) results in the maximum mean force. However, the phase can vary a bit around that point with almost no adverse effect.

2.3.4 \hat{z} Directed Force on the Second Coil

This section will derive an expression for the \hat{z} directed force on the second coil due to the presence of the slab and the eddy-currents induced in it by the first coil. Start by recalling that the force on an element of the second coil is given by $d\vec{F} = I_2 d\vec{l} \times \vec{B}$. Since we are only interested in the total force along the z axis, and since $d\vec{l}$ lays in the $x - y$ plane and \vec{B} has no ϕ component, only the radial component of the magnetic field contributes, resulting in $dF\hat{z} = -I_2 d\vec{l} \times B_\rho \hat{\rho}$.

To resolve the cross product, start with the equation for the second coil (see Figure 6)

$$y^2 + (x - b)^2 = r_2^2 \quad \rightarrow \quad y[x] = \sqrt{r_2^2 - (x - b)^2} \quad b - r_2 \leq x \leq b + r_2 \quad (66)$$

Recalling that $\rho = \sqrt{x^2 + y^2}$, the dy and ρ become

$$dy[x] = \frac{b - x}{\sqrt{r_2^2 - (x - b)^2}} dx \quad \text{and} \quad \rho = \sqrt{r_2^2 - b^2 + 2bx} \quad (67)$$

Converting $\hat{\rho}$ to Cartesian coordinates yields

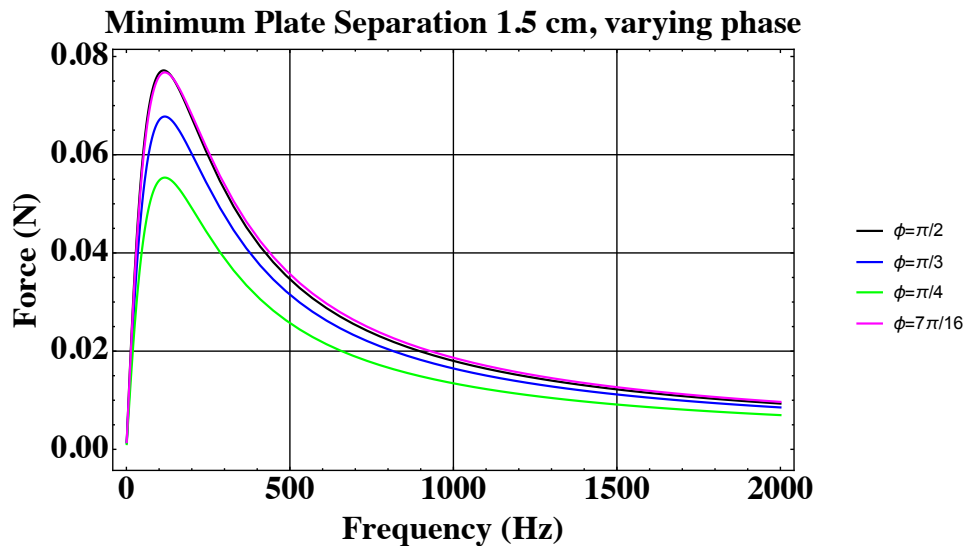


Figure 5. Four coil linear induction motor model with varying phase between adjacent coils

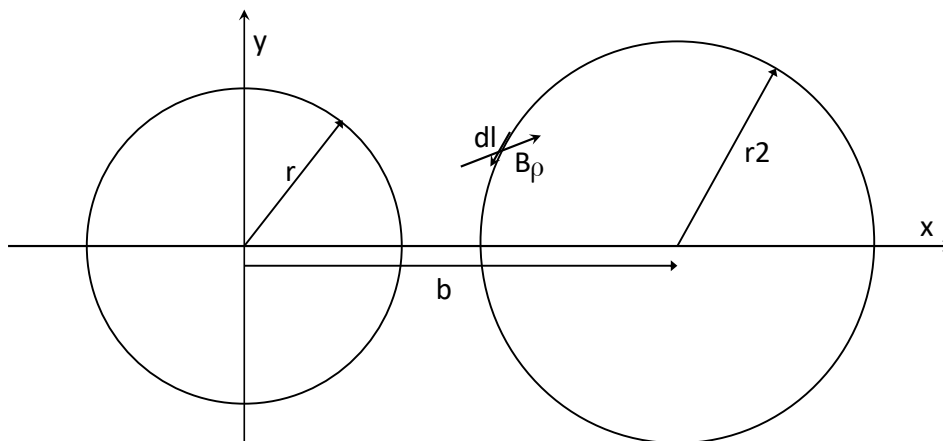


Figure 6. The two loops are shown so that the relationship between $d\vec{l}$ and $B_\rho \hat{\rho}$ can be seen.

$$\hat{\rho} = \frac{x}{(x^2 + y[x]^2)^{1/2}} \hat{x} + \frac{y[x]}{(x^2 + y[x]^2)^{1/2}} \hat{y} \quad \text{where} \quad b - r_2 \leq x \leq b + r_2 \quad (68)$$

Noting that $d\vec{l} = (dx, dy[x], 0)$ on the second coil, the cross product becomes

$$d\vec{l} \times \vec{\rho} = \frac{r_2^2 + bx - b^2}{((b + r_2 - x)(-b + r_2 + x)(r_2^2 - b^2 + 2bx))^{1/2}} \hat{z} \quad (69)$$

So the force on the differential loop element, $d\vec{l}$, is in the \hat{z} direction and is given by

$$dF_z(t) = -I_2(t) B_\rho(\rho, d_2, t) \frac{r_2^2 + bx - b^2}{((b + r_2 - x)(-b + r_2 + x)(r_2^2 - b^2 + 2bx))^{1/2}} \quad (70)$$

Using the exponential expressions to express the time dependence of the current and field, and recalling that the current has a φ phase difference when compared to the current in the first coil, the average force can be found in a process similar to that used above, yielding

$$dF_z = -I_2 B_\rho(\rho, d_2) e^{-i\varphi} \frac{r_2^2 + bx - b^2}{4((b + r_2 - x)(-b + r_2 + x)(r_2^2 - b^2 + 2bx))^{1/2}} + c.c. \quad (71)$$

Recall that

$$B_\rho(\rho, d_2) = -\frac{\partial A(\rho, z)}{\partial z} \Big|_{z=d_2} \quad (72)$$

where, from above

$$A(\rho, z) = \int_0^\infty F(\alpha) e^{\alpha d} e^{-\alpha z} J_1(\alpha \rho) d\alpha \quad (73)$$

so

$$B_\rho(\rho, d_2) = \alpha \int_0^\infty F(\alpha) e^{\alpha(d-d_2)} J_1(\alpha \rho) d\alpha \quad (74)$$

Using this the differential force is

$$dF_z = -I_2 \int_0^\infty \alpha F(\alpha) e^{\alpha(d-d_2)} J_1(\alpha \rho) d\alpha e^{-i\varphi} \frac{r_2^2 + bx - b^2}{4((b + r_2 - x)(-b + r_2 + x)(r_2^2 - b^2 + 2bx))^{1/2}} + c.c. \quad (75)$$

The total force on the second coil is then given by integrating this expression over x from $b - r_2$ to $b + r_2$, yielding (a factor of 2 has been added because the integral only accounts for half of the second loop)

$$F_z = -I_2 \int_0^\infty \alpha F(\alpha) e^{\alpha(d-d_2)} e^{-i\varphi} \int_{b-r_2}^{b+r_2} \frac{J_1(\alpha \sqrt{r_2^2 - b^2 + 2bx})(r_2^2 + bx - b^2)}{2((b + r_2 - x)(-b + r_2 + x)(r_2^2 - b^2 + 2bx))^{1/2}} dx d\alpha + c.c. \quad (76)$$

where $F(\alpha)$ is given by Equation 60 (for the case of a single conducting slab. Other forms for $F(\alpha)$ arise when multiple slabs or ferrous slabs are modeled) which is repeated here for convenience.

$$F(\alpha) = \mu_0 I r \frac{J_1(\alpha r)}{2} \left(\frac{(\alpha^2 - \alpha_1^2) e^{-2\alpha d} (e^{\alpha_1 s} - e^{-\alpha_1 s})}{(\alpha + \alpha_1)^2 e^{\alpha_1 s} - (\alpha - \alpha_1)^2 e^{-\alpha_1 s}} \right) \quad (77)$$

as a check, if $b = 0$, $I_2 = I$, $r_2 = r$ and $d_2 = d$ and $\varphi = 0$ then we should recover the \hat{z} directed force of the drive coil onto itself. Making these substitutions the force equation above becomes

$$F_z = -I_2 r \int_0^\infty \alpha F(\alpha) \int_{-r_2}^{r_2} \frac{J_1(\alpha r)}{2(r^2 - x^2)^{1/2}} dx d\alpha + c.c. = -\frac{I_2 \pi r}{2} \int_0^\infty \alpha (F(\alpha) + F^*(\alpha)) J_1(\alpha r) d\alpha \quad (78)$$

which is the same result as found earlier. Another interesting case occurs when $b = r_2$, the second coil touches the center of the first coil. In this case the Force expression simplifies to

$$F_z = -I_2 \int_0^\infty \alpha F(\alpha) e^{\alpha(d-d_2)} e^{-i\varphi} \int_0^{2r_2} \frac{J_1(\alpha \sqrt{2r_2 x}) r_2}{2(2r_2(2r_2 - x))^{1/2}} dx d\alpha + c.c. \quad (79)$$

$$F_z = -\frac{I_2 \pi r}{2} \int_0^\infty \alpha F(\alpha) e^{\alpha(d-d_2)} e^{-i\varphi} J_1(\alpha r_2) J_0(\alpha r_2) d\alpha + c.c.$$

2.3.5 Mathematica Simulation of Repulsive Force in a Linear Induction Motor

Returning to the linear induction motor described in Section 2.3.3 and using the math given by Equations 76 and 77, it is possible to calculate the total repulsive force for the LIM. This force consists of the interactions of each individual coil with the eddy-currents it generates plus the forces generated on each coil by the eddy-currents from adjacent coils. Numbering the coils 1 through 4, the following force pairs must be computed for the most general case: 1-1, 2-2, 3-3, 4-4, 1-2, 2-1, 1-3, 3-1, 2-3, 3-2, 1-4, 4-1, where the first number in each pair is the drive coil and the second number is the coil feeling the force.

For our example, the symmetries help to reduce the computation. Coils 1 and 3 are the closest to the plate having a separation of 1.5 cm. So, only the self-induced force for one of the pairs (1-1 or 3-3) needs to be computed and doubled. The same is true for coils 2 and 4 which are at 3.5 cm from the plate. The phase relationships then determine which of the other terms are needed. When driving the coils in quadrature, directly adjacent pairs 1-2 and 2-1 have equal and opposite forces and cancel each other. However, coils that are two apart (i.e., 1-3, 3-1, 2-4, 4-2) are driven out of phase with one another so that the eddy-current forces on the coils don't cancel each other. In fact, they have a net attractive force that reduces the overall repulsive force, depending on the amount of coil overlap. The furthest apart coil pairs, 1-4 and 4-1, again cancel each other.

The amount of overlap was varied to see how much of a reduction in the repulsive force could be achieved as this is undesirable in a LIM that is created to drive

longitudinally. Figure 7 shows a series of plots for different amounts of coil overlap. As overlap increases to $b=r/4$, the repulsive force is almost half of that of the case where $b=r$. Unfortunately, the same holds true for the longitudinal forces. As overlap increases, the longitudinal force decreases by a similar factor to the net repulsive force. The main advantage can be seen in the right hand plots that show the frequency where the longitudinal and repulsive forces are equal in magnitude. As overlap is increased, so is the frequency band where the longitudinal force is larger than the repulsive force.

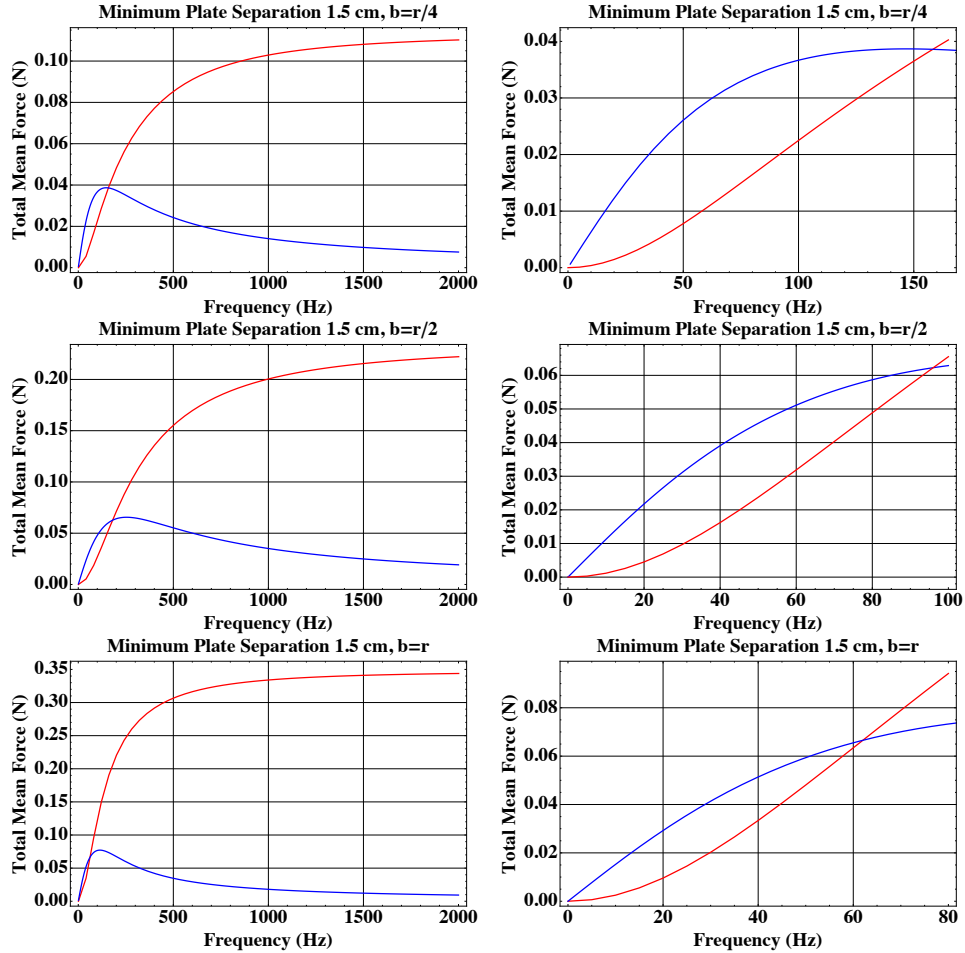


Figure 7. Plots showing the lateral (blue) and repulsive (red) forces for different amount of coil overlap. The left hand side shows the forces over a range of 0-2 kHz while the right side zooms in on the potentially more useful region where the lateral force exceeds the repulsive force. From top to bottom, the first pair of plots is for $b=r/4$, the 2nd set is for $b=r/2$, and the last pair is for $b=r$

2.3.6 Comparison of Linear Induction Motor Forces using a Mathematica Simulation and a COMSOL Model

A four coil linear induction model was constructed using our analytic approach in Mathematica and compared to a similar one constructed in the COMSOL Multiphysics program which uses finite elements to solve the mathematics in a discrete numeric method. For this comparison, the coils were assumed to have a radius of 1.5 cm and an overlap of the same size so that the center of each coil overlaps the outer edge of the next. Each coil was modeled as an infinitely thin loop of current (125 Amps) driven 90 degrees out of phase from the adjacent coil (quadrature). The coils faced a 3 mm thick aluminum plate with a conductivity of 3.5×10^7 S/m. The coils were staggered with the closest pair being 2.5 mm from the aluminum plate and the remaining two half a cm further at 7.5 mm. The comparison of the repulsive and lateral forces appear in the pair of plots shown in Figure 8.

The results between the two models are in fairly close agreement. The slight differences that do occur are likely due to the discrete nature of the finite element model and potentially insufficient mesh density in regions of the plate. Additionally, numeric computations are used with Mathematica - Some of the integrals are performed as a discrete sum over a non-infinite range of values, potentially contributing to the differing results.

The documentation for the COMSOL model appears in the Appendix.

2.4 One Coil Facing a Conductive Slab with a Time Varying/Pulsed Current

In the previous sections, the analysis was restricted to a sinusoidally varying current. This limitation allowed the vector potential to be separated into the product of a time varying and a spatially varying function, permitting the solution to be obtained. But there is interest in allowing the current to be more general, for example, pulsed, and that case will be considered here. This type of drive current might best lend itself to the application of repelling space debris. So, much larger currents are used in the examples resulting in much larger forces and magnetic fields.

The case of a time varying current can be handled using Fourier Transforms, however, the force calculation is nonlinear so some care is required. Start by considering the force expression derived above for the total force on the coil (after integrating around the coils circumference)

$$\vec{F} = I(t) 2\pi r \frac{\partial A(r, d, t)}{\partial z} \hat{z}, \quad (80)$$

Since the current, $I(t)$ is assumed to be known, then the problem is to find the vector potential and its derivative corresponding to this current and use this equation to find the force. (Note that both the current and the vector potential derivative in this expression are real quantities.) The vector potential is linear in the current, allowing Fourier Transforms to be used to find it for the general current. Let $I(\omega)$ be the Fourier Transform of $I(t)$ such that

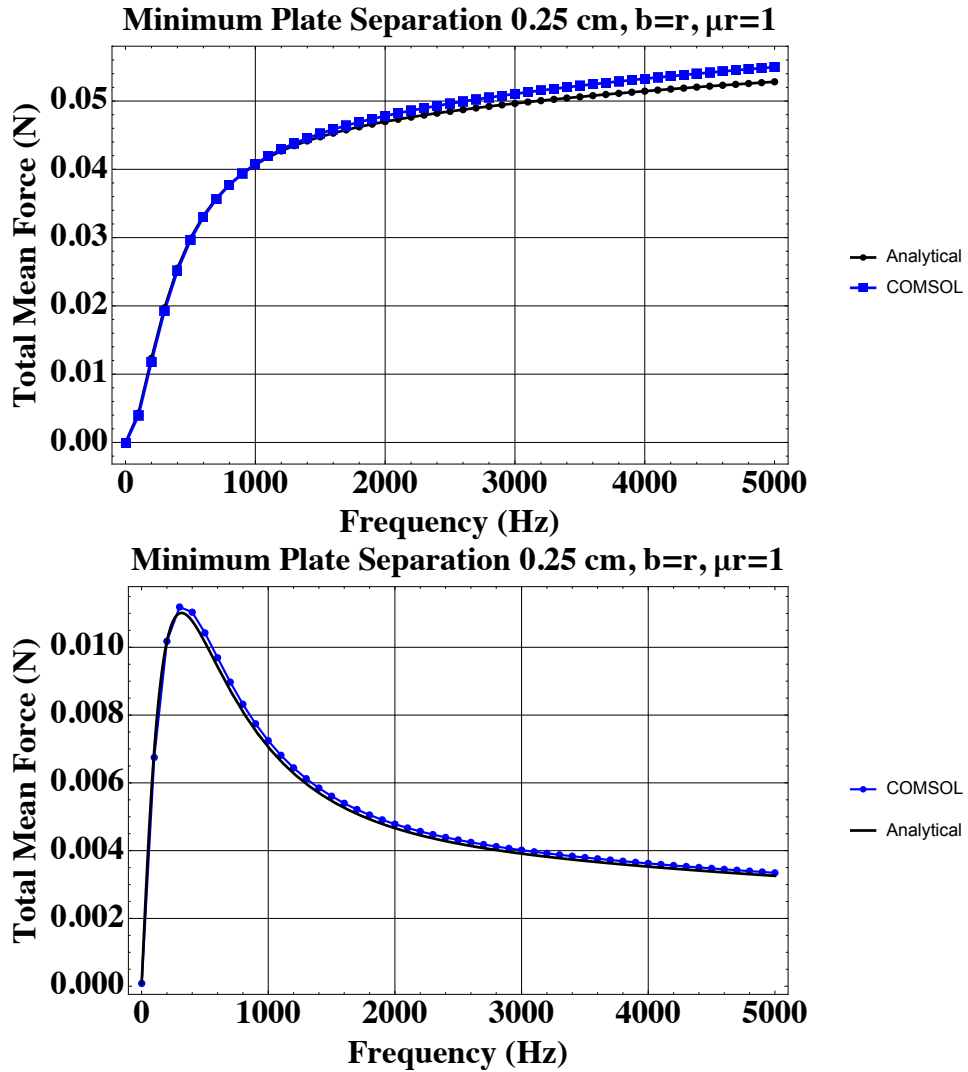


Figure 8. Plots showing a comparison between the analytical model and a COMSOL model when used to compute the longitudinal (top) and repulsive (bottom) forces with an aluminum slab for a four coil LIM driven in quadrature with a coil overlap equal to the radius. Slight differences occur due to the discrete nature of the finite elements used in the COMSOL model.

$$I(t) = \frac{1}{\sqrt{2\pi}} \int_{-\infty}^{\infty} I(\omega) e^{i\omega t} d\omega \quad I(\omega) = \frac{1}{\sqrt{2\pi}} \int_{-\infty}^{\infty} I(t) e^{-i\omega t} dt \quad (81)$$

$I(\omega)$ is interpreted here as the amplitude of current oscillating at frequency ω in each frequency interval, $d\omega$. Recall that even though $I(t)$ is a real function, $I(\omega)$ is a complex function whose complex phase corresponds to the phase of that portion of current oscillating at frequency ω .

Previously the vector potential for a single frequency was found. This result can be generalized to express the vector potential derivative amplitude, corresponding to the size and phase of the vector potential derivative at a specified frequency

$$\frac{\partial A(r, d, \omega)}{\partial z} = - \int_0^{\infty} \alpha F(\alpha) J_1(\alpha r) d\alpha. \quad (82)$$

where

$$F(\alpha) = \mu_0 I(\omega) r \frac{J_1(\alpha r)}{2} \left(\frac{(\alpha^2 - \alpha_1^2) e^{-2\alpha d} (e^{\alpha_1 s} - e^{-\alpha_1 s})}{(\alpha + \alpha_1)^2 e^{\alpha_1 s} - (\alpha - \alpha_1)^2 e^{-\alpha_1 s}} \right) \quad (83)$$

and

$$\alpha_1 = \sqrt{\alpha^2 + i\omega\mu_0\sigma}. \quad (84)$$

The only difference between this and the previous expression is that the function $I(\omega)$, which replaces the previous constant I , describes the amount and the phase of the current oscillating at frequency ω .

Now, to find the time varying, real, vector potential derivative, the frequency components have to be summed

$$\frac{\partial A(r, d, t)}{\partial z} = \text{Real} \left[\frac{1}{\sqrt{2\pi}} \int_{-\infty}^{\infty} \frac{\partial A(r, d, \omega)}{\partial z} e^{i\omega t} d\omega \right] \quad (85)$$

Putting this result into the Eq. 80 yields the total force. This represents the force between a single loop of current and the eddy current it forms in the conductive plate.

This analytic model was compared to a similar model built in COMSOL and the results are in close agreement. The current loop was assumed to be 0.19 m in diameter and located 0.01 m from a copper plate that has a thickness of 0.013 m. The current and the resulting force are shown in Figure 9 for both the analytic and COMSOL solutions. In the Mathematica notebook, Fast Fourier Transforms (FFT) were used for transforming the time dependent current into the frequency domain where it could be inserted into the frequency domain representation of the derivative of the magnetic vector potential. This was then converted back to the time domain via the inverse FFT. In Mathematica, the commands that call on these routines are Fourier and InverseFourier. These commands offer options to use different Fourier pairs by setting the FourierParameters option. Only the FourierParameters setting of {1,-1} , associated with signal processing, produced the correct magnitude and phase response.

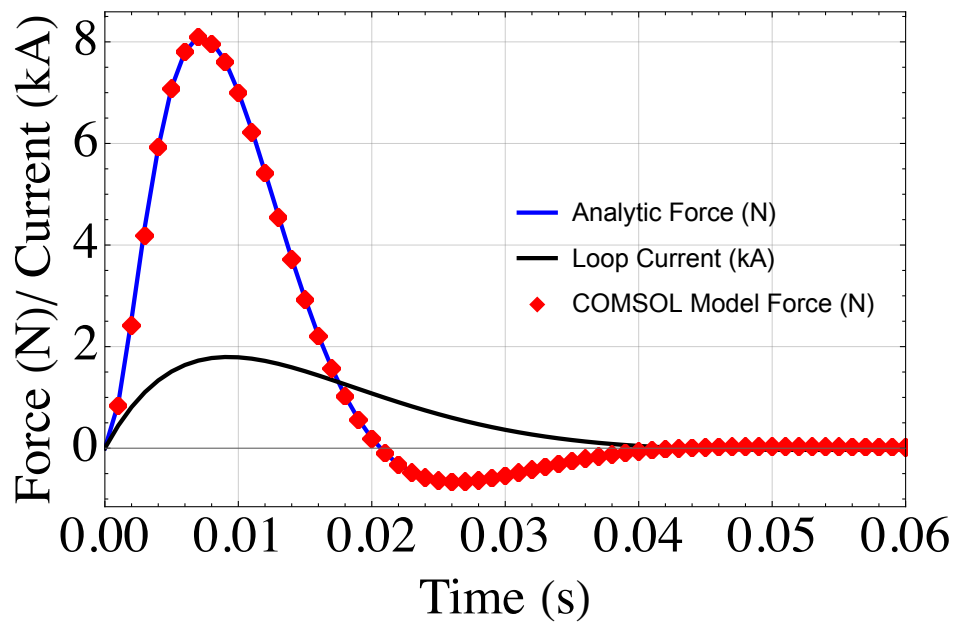


Figure 9. Plots showing a comparison between the analytical model and a COMSOL model when used to compute the repulsive forces between a copper slab and pulsed current loop.

2.5 Multi-turn Coil Facing a Conductive Slab with a Time Varying/ Pulsed Current

To get the force for a solenoid, the math in the prior sub-section needs to be generalized a bit further. We'll need to use pairs of coils and sum the forces from eddy currents generated by one coil on the current flowing in a second coil. We'll use r_1 and d_1 to represent the radius and distance from the plate of the first coil and r_2 and d_2 to represent the radius and distance of the 2nd coil. The different combinations of forces then sum according to the following slightly modified equations to get the force between the whole solenoid and the plate.

$$\vec{F} = \sum_{r_1} \sum_{r_2} \sum_{d_1} \sum_{d_2} I(t) 2\pi r_1 \frac{\partial A(r_1, r_2, d_1, d_2, t)}{\partial z} \hat{z}, \quad (86)$$

$$\frac{\partial A(r_1, r_2, d_1, d_2, \omega)}{\partial z} = - \int_0^\infty \alpha F(\alpha) J_1(\alpha r_2) e^{\alpha(d_1 - d_2)} d\alpha, \quad (87)$$

$$F(\alpha) = \mu_0 I(\omega) r_1 \frac{J_1(\alpha r_1)}{2} \left(\frac{(\alpha^2 - \alpha_1^2) e^{-2\alpha d_1} (e^{\alpha_1 s} - e^{-\alpha_1 s})}{(\alpha + \alpha_1)^2 e^{\alpha_1 s} - (\alpha - \alpha_1)^2 e^{-\alpha_1 s}} \right). \quad (88)$$

To get the force for a cylinder of the same thickness as the slab, an approximation can be made by scaling the force by the ratio between the surface areas of the cylinder and the coil. Also, since the transforms pairs aren't dependent on radius or the distance, they remain the same as above.

As an example, let's consider a 92 turn pancake style coil made from 10 gauge copper transformer wire with 23 wraps in the radial direction (inner radius 8.5 cm, outer radius of 15.6 cm) and 4 wraps in the axial direction. We'll assume this is placed opposite a copper plate that is 1.3 cm thick. As a starting distance, the separation between the plate and the closest loop is 1 cm. The coil will then extend to about 2.1 cm from the plate. If we assume the same current is flowing in this solenoid as the single loop coil in the prior subsection, we can expect to see about n^2 times the peak force of around 8 N, where n is the number of turns in the solenoid. The eddy current generated in the slab by each loop of current generates a force on every other loop, including itself giving rise to the n^2 number of forces to compute and sum. So, for this case, we would expect an estimated $92^2 * 8 = 67.7$ kN of force. Of course, the majority of the loops in the solenoid are further away from the plate than the single loop so that the total force should be something less than this estimate. In this case, the actual value is approximately 56 kN. The plots that show the force between this solenoid and the plate for different separation distances is given in Figure 10.

Thus far we have only looked at the forces, but it's important to point out that the magnetic field may also be easily computed. One method to do this is to find the magnetic vector potential for each loop using Equations 25, 37, and 84 combined with $I(\omega)$ in the frequency domain, sum the results for each loop and then take the inverse transform to get the total magnetic vector potential in the time domain. The magnetic field is then found using the relation $\vec{B} = \nabla \times \vec{A}$. Since the magnetic vector potential is only in the $\hat{\phi}$ direction with no dependence on ϕ , the resulting answer yields a magnetic field of the form $\vec{B}(\rho, z) = B(\rho, z)\hat{\rho} + B(\rho, z)\hat{z}$.

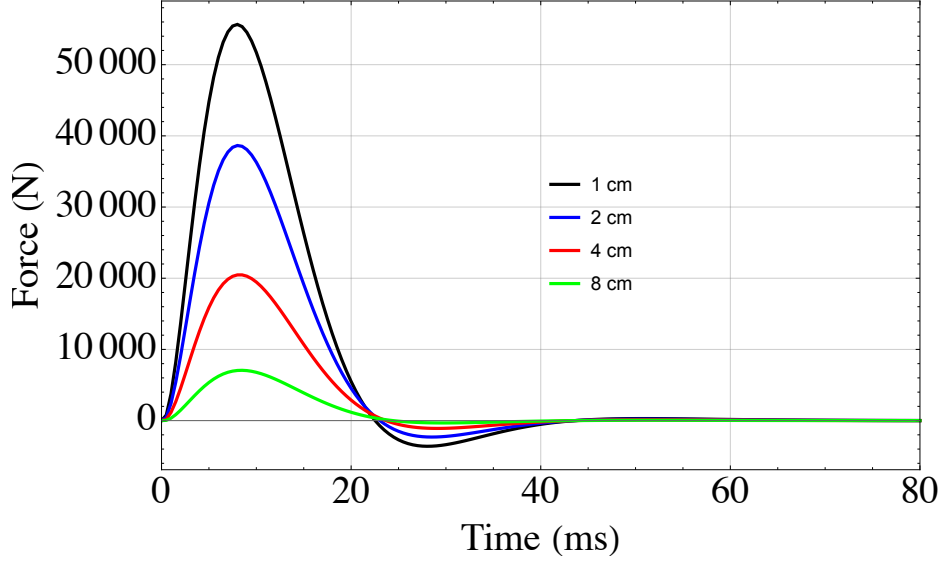


Figure 10. Plots showing the repulsive forces between a solenoid and a copper slab for four different separation distances. The excitation current pulse is the same as shown in Figure 9.

2.6 Electromagnetic coil surrounding an electrically conductive cylinder

This section presents the mathematics to predict the forces on a conductive cylinder centered on a current loop as the first step towards a model for a piece of space debris interacting with a magnetic shielding system. The analysis assumes a sinusoidally oscillating current.

2.6.1 Problem Setup

Assume a single current loop, or coil, of radius r has current $I(t)$ flowing through it. Place a cylindrical coordinate system onto the coil, with origin centered on the coil, and the coil laying in the $z = 0$ plane. Now place a cylinder or rod, of radius d , on the \hat{z} axis. The slab is assumed to have conductivity, σ and be non-magnetic $\mu_r = 1$. The magnetic vector potential due to just the coil is as derived in Section 2.1

2.6.2 Oscillating Current and Infinite Length Rod

In this section the rod is assumed to be infinitely long and the current is assumed to be oscillating as $I(t) = I \cos \omega t$ where $\omega = 2\pi f$, is the angular frequency and f is the frequency of the oscillation. We approach this problem by solving for the vector potential \vec{A} , starting with the non-homogeneous wave equation for \vec{A} ,

$$\nabla^2 \vec{A} - (1/c^2) \frac{\partial^2 \vec{A}}{\partial t^2} = -\mu_0 \vec{J}, \quad (89)$$

where \vec{J} is the current density. We limit our maximum frequency to about 10 kHz and our maximum length or size to one meter. Consequently, the time derivative has a maximum factor about 4×10^{-8} times smaller than the spatial derivative and can be dropped, leaving

$$\nabla^2 \vec{A} = -\mu_0 \vec{J}. \quad (90)$$

The current density in the coil is given by $\vec{J} = I(t)\delta(\rho - r)\delta(z)\hat{\phi}$. Since the current only points in the $\hat{\phi}$ direction, so does the vector potential, and recalling the problem has cylindrical symmetry (i.e. no ϕ dependence) allows the vector potential to be written in the form, $\vec{A} = A(\rho, z, t)\hat{\phi}$. Then, assuming a Lorentz Gauge,

$$\nabla \cdot \vec{A} + \frac{1}{c^2} \frac{\partial V}{\partial t} = 0, \quad (91)$$

we see that $\nabla \cdot \vec{A}$ can be assumed to be zero because at low frequency the change in potential divided by c^2 is very small. These two results allow the vector Laplacian to be replaced by a double curl and allows the vector differential equation to reduce to a scalar differential equation (taking only the $\hat{\phi}$ direction)

$$\nabla^2 \vec{A} = -\nabla \times \nabla \times \vec{A} = \left(\frac{\partial^2 A}{\partial \rho^2} + \frac{\partial^2 A}{\partial z^2} + \frac{1}{\rho} \frac{\partial A}{\partial \rho} - \frac{A}{\rho^2} = -\mu_0 J \right) \hat{\phi}. \quad (92)$$

Now, assuming separation of variables, we write $A(\rho, z) = A_\rho(\rho)A_z(z)$ and this equation, after dividing by $A_\rho(\rho)A_z(z)$, becomes

$$(A''_\rho + A'_\rho/\rho - A_\rho/\rho^2)/A_\rho + A''_z/A_z = -\mu_0 J/(A_\rho A_z) \quad (93)$$

where primes indicate differentiation and where the explicit variable dependence has been dropped since the subscripts provide that information.

2.6.3 The Magnetic Vector Potential Including the Rod

Inside of the conductive rod the time variation of the vector potential generates an electric field given by $\vec{E} = -\partial \vec{A}/\partial t$. This causes currents to flow by Ohm's Law, $\vec{J} = \sigma \vec{E}$. Using these, the differential equation for the vector potential in the rod becomes

$$\nabla^2 \vec{A} = -\mu_0 \vec{J} = -\mu_0 \sigma \vec{E} = \mu_0 \sigma \frac{\partial \vec{A}}{\partial t}. \quad (94)$$

Now assume the coil current is varying sinusoidally, $I(t) = I \cos(\omega t)$, causing the vector potential to also vary sinusoidally and allowing it to be expressed as

$$\vec{A}(\rho, z, t) = \frac{\vec{A}(\rho, z) e^{i\omega t} + \vec{A}^*(\rho, z) e^{-i\omega t}}{2} \quad (95)$$

There is a phase difference between the current and the vector potential that will cause $\vec{A}(\rho, z)$ to be complex, but when we calculate forces we will need to multiply the vector potential times the current and this multiplication can only be done between real terms, not complex ones. Consequently, it must be kept in mind that before this multiplication can be performed that the above formula must be used to

recover the real version of the vector potential. So using $\vec{A}(\rho, z) e^{i\omega t}$ as the form for the vector potential, the differential equation in the rod becomes

$$\nabla^2 \vec{A} = -\nabla \times \nabla \times \vec{A} = \frac{\partial^2 \vec{A}}{\partial \rho^2} + \frac{\partial^2 \vec{A}}{\partial z^2} + \frac{1}{\rho} \frac{\partial \vec{A}}{\partial \rho} - \frac{\vec{A}}{\rho^2} = i\omega\mu_0\sigma \vec{A}. \quad (96)$$

The coefficient $\omega\mu_0\sigma$ can be significant. Aluminum has a conductivity of about 4×10^7 A/(V-m) and if the frequency is 50 Hz this coefficient is about 16,000 m⁻². So the term on the right of this equation must be kept through the analysis.

As was the case with the isolated coil, the currents and therefore the magnetic vector potential are only in the $\hat{\phi}$ direction. So, $\vec{A} = A(\rho, z)\hat{\phi}$, allowing Eq. 96 to be written in scalar form. Then, using separation of variables, $A(\rho, z) = A_\rho(\rho) A_z(z)$, yields the differential equation

$$\begin{aligned} (A_\rho'' + A_\rho'/\rho - A_\rho/\rho^2)/A_\rho + A_z''/A_z &= i\omega\mu_0\sigma \\ (A_\rho'' + A_\rho'/\rho - A_\rho/\rho^2)/A_\rho - i\omega\mu_0\sigma &= \alpha^2 = -A_z''/A_z \end{aligned} \quad (97)$$

Solving this yields the solution for a specific α

$$A(\rho, z) = C_1 \cos \alpha z (C_2 K_1(\alpha_1 \rho) + C_3 I_1(\alpha_1 \rho)), \quad (98)$$

where $\alpha_1 = \sqrt{\alpha^2 + i\omega\mu_0\sigma}$. The function $Y_1(\alpha_1 \rho)$ is a Bessel function of the second kind and is not bounded when $\rho = 0$, so $C_3 = 0$. Combining this with the isolated coil result from the previous section yields the following expression for the vector potential

$$A(\rho, z) = \begin{cases} \int_0^\infty A(\alpha) \cos \alpha z I_1(\alpha_1 \rho) d\alpha, & \rho < d \\ \int_0^\infty \cos \alpha z (C(\alpha) I_1(\alpha \rho) + B(\alpha) K_1(\alpha \rho)) d\alpha, & d < \rho < r \\ \int_0^\infty D(\alpha) \cos \alpha z K_1(\alpha \rho) d\alpha, & \rho > r \end{cases} \quad (99)$$

Across each interface the vector potential is continuous and, since the rod is assumed to not be magnetic ($\mu_r = 1$), the tangential component of the magnetic field, $H_z = (1/\rho)\partial(\rho A)/\partial\rho$, is continuous across the surface of the rod. Combining these with the boundary condition across the coil itself, supplies four conditions on the four functions shown, allowing the problem to be solved.

Start with continuity of the vector potential across the surface of the rod, i.e. at $\rho = d$. From the above expressions this yields

$$A(\alpha) I_1(\alpha_1 d) = C(\alpha) I_1(\alpha d) + B(\alpha) K_1(\alpha d) \quad (100)$$

Now consider the magnetic field boundary condition. Recall that

$$(1/\rho) \frac{\partial}{\partial \rho} (\rho I_1(\beta \rho)) = \beta I_0(\beta \rho) \quad \text{and} \quad (1/\rho) \frac{\partial}{\partial \rho} (\rho K_1(\beta \rho)) = -\beta K_0(\beta \rho). \quad (101)$$

Using this, the magnetic field boundary condition at the surface of the rod yields

$$A(\alpha) \alpha_1 I_0(\alpha_1 d) = C(\alpha) \alpha I_0(\alpha d) - \alpha B(\alpha) K_0(\alpha d) \quad (102)$$

Continuity across the $\rho = r$ interface supplies this condition

$$D(\alpha)K_1(\alpha r) = C(\alpha)I_1(\alpha r) + B(\alpha)K_1(\alpha r) \quad (103)$$

The last condition on these functions is found by integrating across the loop itself from $r - \epsilon$ to $r + \epsilon$, a very small distance. So consider, Eq. 92 with the coil current inserted

$$\frac{\partial^2 A}{\partial \rho^2} + \frac{\partial^2 A}{\partial z^2} + \frac{1}{\rho} \frac{\partial A}{\partial \rho} - \frac{A}{\rho^2} = -\mu_0 I \delta(z) \delta(\rho - r). \quad (104)$$

Integrate along a line from $(r - \epsilon, 0)$ to $(r + \epsilon, 0)$ passes through the coil. Assuming the z derivative is the same on either side, yields

$$\frac{1}{\rho} \frac{\partial \rho A}{\partial \rho} \Big|_{r+\epsilon} - \frac{1}{\rho} \frac{\partial \rho A}{\partial \rho} \Big|_{r-\epsilon} = -\mu_0 I \delta(z). \quad (105)$$

Substituting in the general solution and letting ϵ go to zero yields

$$-\int_0^\infty D(\alpha) \alpha \cos \alpha z K_0(\alpha r) d\alpha - \int_0^\infty C(\alpha) \alpha \cos \alpha z I_0(\alpha r) d\alpha + \int_0^\infty B(\alpha) \alpha \cos \alpha z K_0(\alpha r) d\alpha = -\mu_0 I \delta(\rho - r). \quad (106)$$

Now, recall that

$$\int_0^\infty \cos(\beta z) \cos(\alpha z) dz = \delta(\beta - \alpha) + \delta(\beta + \alpha), \quad (107)$$

which can be used to simplify the expression above. Multiply both sides by $\cos(\beta z)$, where $\beta > 0$ and integrate z from 0 to ∞ . Since $\alpha > 0$ only the $\delta(\beta - \alpha)$ term is retained

$$\begin{aligned} & \int_0^\infty \int_0^\infty D(\alpha) \alpha \cos \beta z \cos \alpha z K_0(\alpha r) d\alpha dz + \int_0^\infty \int_0^\infty C(\alpha) \alpha \cos \beta z \cos \alpha z I_0(\alpha r) d\alpha dz \\ &= \int_0^\infty \int_0^\infty B(\alpha) \alpha \cos \beta z \cos \alpha z K_0(\alpha r) d\alpha dz + \int_0^\infty \cos \beta z \mu_0 I \delta(z) dz \\ & \int_0^\infty D(\alpha) \alpha \delta(\alpha - \beta) K_0(\alpha r) d\alpha + \int_0^\infty C(\alpha) \alpha \delta(\alpha - \beta) I_0(\alpha r) d\alpha = \int_0^\infty B(\alpha) \alpha \delta(\alpha - \beta) K_0(\alpha r) d\alpha + \mu_0 I \\ & D(\alpha) \alpha K_0(\alpha r) + C(\alpha) \alpha I_0(\alpha r) = B(\alpha) \alpha K_0(\alpha r) + \mu_0 I. \end{aligned} \quad (108)$$

Now solve Eqs. 102, 100, 103 and 108 for the functions $A(\alpha)$, $B(\alpha)$, $C(\alpha)$, and $D(\alpha)$ to obtain

$$\begin{aligned} A(\alpha) &= \frac{\mu_0 I r}{\pi} \frac{K_1(\alpha r)}{\alpha d I_1(\alpha_1 d) K_0(\alpha d) + \alpha_1 d I_0(\alpha_1 d) K_1(\alpha d)} \\ B(\alpha) &= \frac{\mu_0 I r}{\pi} \frac{(-\alpha_1 I_0(\alpha_1 d) I_1(\alpha d) + \alpha I_0(\alpha d) I_1(\alpha_1 d)) K_1(\alpha r)}{\alpha I_1(\alpha_1 d) K_0(\alpha d) + \alpha_1 I_0(\alpha_1 d) K_1(\alpha d)} \\ C(\alpha) &= \frac{\mu_0 I r}{\pi} K_1(\alpha r) \\ D(\alpha) &= \frac{\mu_0 I r}{\pi} I_1(\alpha r) + \frac{\mu_0 I r}{\pi} \frac{(-\alpha_1 I_0(\alpha_1 d) I_1(\alpha d) + \alpha I_0(\alpha d) I_1(\alpha_1 d)) K_1(\alpha r)}{\alpha I_1(\alpha_1 d) K_0(\alpha d) + \alpha_1 I_0(\alpha_1 d) K_1(\alpha d)} \end{aligned} \quad (109)$$

and the vector potential is

$$A(\rho, z) = \begin{cases} \int_0^\infty A(\alpha) \cos \alpha z I_1(\alpha_1 \rho) d\alpha, & \rho < d \\ \int_0^\infty \cos \alpha z (C(\alpha) I_1(\alpha \rho) + B(\alpha) K_1(\alpha \rho)) d\alpha, & d < \rho < r \\ \int_0^\infty D(\alpha) \cos \alpha z K_1(\alpha \rho) d\alpha, & \rho > r \end{cases} \quad (110)$$

where

$$\alpha_1 = \sqrt{\alpha^2 + i\omega\mu_0\sigma} \quad (111)$$

2.6.4 The Force on the Cylinder

Now consider the force on the cylinder due to the coil current. The total force can be found more easily by integrating across the coil, but we want to consider an integral over a finite length in z as an approximation for the force on a finite length cylinder.

The force on a volume element of the cylinder is given by $d\vec{F} = \vec{J}(t) \times \vec{B}$, where $\vec{J}(t)$ is the eddy current density in the cylinder. Since we are only interested in the total force along the z axis, and since the eddy currents are only in the $\hat{\phi}$ direction, only the radial components of the magnetic field contribute, resulting in $dF\hat{z} = -J(t)B_\rho(\rho, z, t)\hat{z}$. $B_\rho(\rho, z, t) = -\partial A(\rho, z, t)/\partial z$. So the force on each differential volume element of the cylinder is given by

$$dF_z(\rho, z, t) = -\sigma \frac{\partial A(\rho, z, t)}{\partial t} \frac{\partial A(\rho, z, t)}{\partial z} \quad (112)$$

where Eq. 94 has been used to replace the eddy current density with the vector potential. Now recall that

$$A(\rho, z, t) = \frac{A(\rho, z) e^{i\omega t} + A^*(\rho, z) e^{-i\omega t}}{2} \quad (113)$$

so the force equation becomes

$$\begin{aligned} dF_z(\rho, z, t) &= -\sigma \frac{\partial}{\partial t} \left(\frac{A(\rho, z) e^{i\omega t} + A^*(\rho, z) e^{-i\omega t}}{2} \right) \frac{\partial}{\partial z} \left(\frac{A(\rho, z) e^{i\omega t} + A^*(\rho, z) e^{-i\omega t}}{2} \right) \\ &= -\sigma \left(\frac{i\omega A(\rho, z) e^{i\omega t} - i\omega A^*(\rho, z) e^{-i\omega t}}{2} \right) \left(\frac{\partial A(\rho, z) / \partial z e^{i\omega t} + \partial A^*(\rho, z) / \partial z e^{-i\omega t}}{2} \right). \end{aligned} \quad (114)$$

Averaging over time only retains the time independent terms

$$dF_z(\rho, z) = -\sigma\omega (iA(\rho, z)\partial A^*(\rho, z)/\partial z - iA^*(\rho, z)\partial A(\rho, z)/\partial z)/4. \quad (115)$$

To obtain the total force on a section of the cylinder this expression must be integrated over a selected volume of the cylinder, from $z = 0$ to $z = h$. In this volume the vector potential is given by

$$A(\rho, z) = \int_0^\infty A(\alpha) \cos \alpha z I_1(\alpha_1 \rho) d\alpha \quad (116)$$

where $A(\alpha)$ is given by Eq. 109. So the total force is given by

$$\begin{aligned}
F_z &= -\frac{\sigma\omega}{4} \int_0^h \int_0^d \int_0^{2\pi} (iA(\rho, z)\partial A^*(\rho, z)/\partial z - iA^*(\rho, z)\partial A(\rho, z)/\partial z) \rho d\phi d\rho dz. \\
&= -\frac{\sigma\omega}{4} \int_0^h \int_0^d \int_0^{2\pi} \left[i \int_0^\infty A(\alpha) \cos \alpha z I_1(\alpha_1 \rho) d\alpha \frac{\partial}{\partial z} \left(\int_0^\infty A(\alpha') \cos \alpha' z I_1(\alpha'_1 \rho) d\alpha' \right) \right] \rho d\phi d\rho dz + c.c. \\
&= \frac{i\sigma\omega\pi}{2} \int_0^h \int_0^d \left[\int_0^\infty A(\alpha) \cos \alpha z I_1(\alpha_1 \rho) d\alpha \int_0^\infty A(\alpha') \alpha' \sin \alpha' z I_1(\alpha'_1 \rho) d\alpha' \right] \rho d\rho dz + c.c.
\end{aligned} \tag{117}$$

where

$$\alpha_1^2 = \alpha^2 - i\omega\mu_0\sigma \tag{118}$$

Further simplification can be achieved by using the following integrals

$$\int_0^h \cos(\alpha z) \sin(\alpha' z) dz = \frac{\alpha \sin(\alpha h) \sin(\alpha' h) + \alpha' \cos(\alpha h) \cos(\alpha' h) - \alpha'}{\alpha^2 - (\alpha')^2} \tag{119}$$

$$\int_0^d I_1(\alpha_1 \rho) I_1(\alpha'_1 \rho) \rho d\rho = \frac{d\alpha_1 I_1(\alpha'_1 d) I_2(\alpha_1 d) - d\alpha'_1 I_1(\alpha_1 d) I_2(\alpha'_1 d)}{\alpha_1^2 - (\alpha'_1)^2} \tag{120}$$

2.6.5 The Magnetic Field

Experimentally the magnetic field is measured and then the force on a conductor is observed. So the magnetic field of the bare coil is needed. This is given by $\nabla \times \vec{A}$, which becomes, in the \hat{z} direction,

$$B_z = \frac{1}{\rho} \frac{\partial(\rho A_\phi)}{\partial \rho} \tag{121}$$

Using the isolated coil expression this becomes

$$B_z = \frac{1}{\pi} \int_0^\infty \mu_0 I(t) \alpha r \cos \alpha z K_1(\alpha r) I_0(\alpha \rho) d\alpha \tag{122}$$

at the center of the loop, $\rho = 0$, this simplifies to the expected result

$$B_z = \mu_0 I(t) \frac{r^2}{2(r^2 + z^2)^{3/2}} \quad \Rightarrow \quad B_z = \frac{\mu_0 I(t)}{2r} \quad \text{when } z = 0 \tag{123}$$

2.6.6 Comments

Space debris may consist of materials with a wide range of conductive properties. It turns out that it is possible to maintain force by varying the coil drive frequency to compensate materials with different conductivities. This is an important result in that debris might be composed of materials with relatively poor conductivity, yet by raising the frequency the repulsive force magnitude could be maintained. In the vector potential analysis present above this result is still present, though with a skin depth effect. First note that in the analysis above, see for example Eq. 96, that the

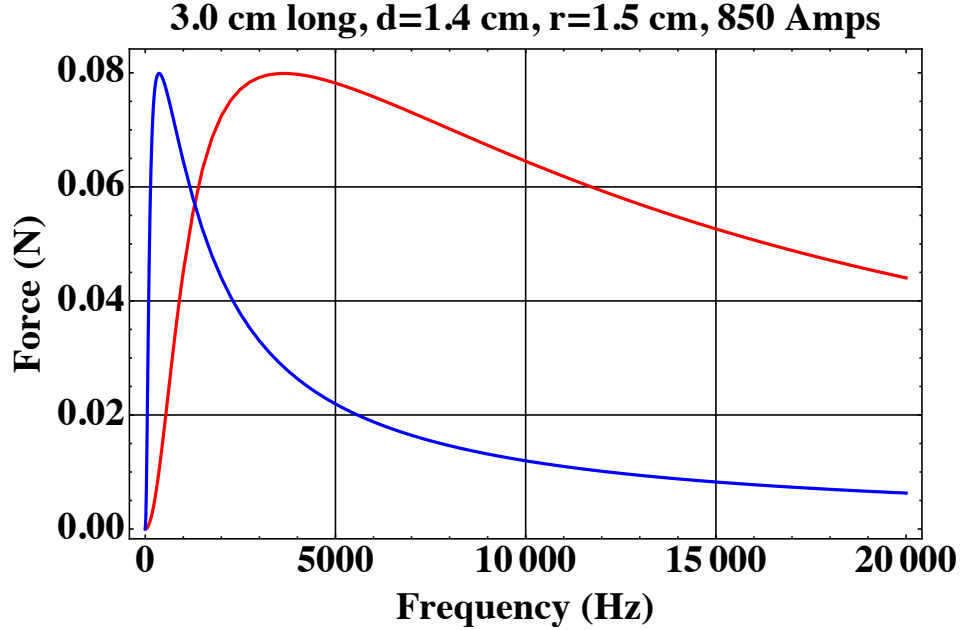


Figure 11. Force plots versus frequency for a small loop (1.5 cm radius) with a cylinder sitting on the plane of the loop with radius 1.5 cm and height equal to 3 cm. Two conductivities are shown, aluminum 4×10^7 S/m (the left plot (blue)) and a lower conductivity (right plot (red)) of 4×10^6 S/m.

conductivity and the frequency only appear in the product, $\omega\sigma\mu_0$. Consequently, lowering the conductivity can always be compensated for by raising the frequency so that this product takes on the same value. Figure 11 shows the force exerted by a coil of 1.5 cm radius, with 850 peak amps, on a cylinder that is sitting on the plane of the coil and is 1.4 cm in radius and 3 cm long. The two plots correspond to two conductivities; that of aluminum ($\sigma = 4 \times 10^7$ S/m) and a conductivity ten times less ($\sigma = 4 \times 10^6$ S/m). Both curves are identical in shape and yield the same peak force, but the low conductivity curve is stretched out further in frequency.

Recall that skin depth is given by $(2/(\omega\sigma\mu_0))^{1/2}$ for non-magnetic materials. So for a 0.015 m radius cylinder of aluminum we would expect the electromagnetic field to have difficulty penetrating the cylinder at frequencies of about 200 Hz and higher. The peak in the curve shown is at about 300 Hz, which is in reasonable agreement (especially when considering that skin depth is defined for a flat plate and the current geometry is cylindrical). So the decay with frequency seen in these curves is due to the oscillating field not being able to penetrate into the cylinder.

The case shown in the figure corresponds to a central magnetic field (i.e., at the center of the coil) of about 36 mT. Figure 12 shows the total force on the low conductivity cylinder for different heights of the cylinder, 0.5 cm, 1.0 cm, and 1.5 cm. The 1.0 cm and 1.5 cm height cylinders have nearly identical forces. One would expect the force on the longer one to be higher, but this isn't the case, probably because the field drops off quickly from the current loop and because the length of

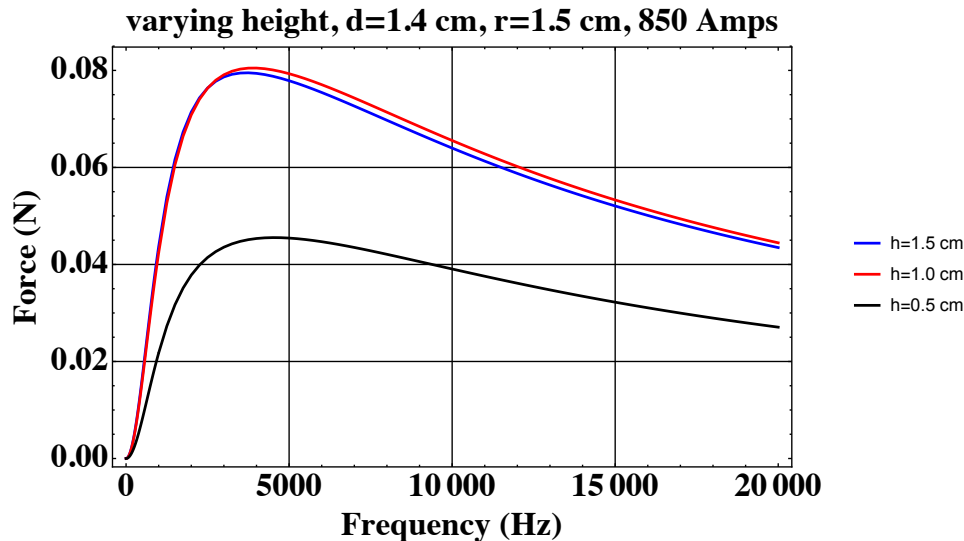


Figure 12. Force plots versus frequency for a small loop (1.5 cm radius) with a cylinder sitting on the plane of the loop with radius 1.5 cm and height equal to 0.5, 1.0, 1.5 cm and conductivity of 4×10^6 S/m.

the cylinder is preventing the higher frequency components from reaching the top of the cylinder.

The 0.5 cm high cylinder weighs 8.4 grams (assuming the same density as aluminum) and the peak force is about 0.045 N, showing that the force is not sufficient to elevate the cylinder (the force is about a factor of 2 too small). The energy stored in the magnetic field displaced by the puck (assuming it is uniform with value 36 mT) is about 0.0016 Joules, which corresponds to a kinetic energy velocity of the puck of about 0.6 m/sec.

In a real world application we would expect to have multiple loops carrying current. So achieving much higher forces are possible, yet alternating current magnets are not readily available. A preferred approach would be a pulsed magnet where the current in the coil increases in time.

3 Magnetic Force Actuators - Electromagnet Coils and their Eddy Current Interactions with Conductive and Ferromagnetic Targets

This section will consider the interactions between electromagnet coils and ferromagnetic plates and combinations of non-magnetic conductors and ferromagnetic plates. It is well known that a DC electromagnet will adhere to ferrous metals, but what happens with AC driven electromagnets? They too, will experience the attractive force at lower frequencies, but ferrous metals are also conductive, so eddy currents will be present to interact with the drive coils, frequently adding repulsive

forces to the mix. Now, add a conductive plate on top of the ferrous one and you get some interesting behaviors previously described by the father of maglev, E. R. Laithwaite [9], and others [10]. The subsections below will explore these behaviors and the mathematics derived from equations for the underlying physics. Once again, examples will be provided based on the coil configurations discussed in prior sections.

3.1 Single Coil Facing a Conductive Ferrous Slab

The math below builds on the derivations in Section 2.1.

3.1.1 The Magnetic Vector Potential for a Coil Facing a Conductive Ferrous Slab

Inside of the conductive slab the time variation of the vector potential generates an electric field given by $\vec{E} = -\partial\vec{A}/\partial t$. This causes currents to flow by Ohm's Law, $\vec{J}_f = \sigma\vec{E}$. In addition, because the slab is ferrous, it becomes magnetized in the presence of the field from the coil. This effect can be described using a magnetization current, J_m , but this needs to be expressed in terms of the vector potential. A better route is to recall one of Maxwell's Equations.

$$\nabla \times \vec{B} - \frac{1}{c^2} \frac{\partial \vec{E}}{\partial t^2} = \mu_0(\vec{J}_f + \nabla \times \vec{M}) \quad (124)$$

where \vec{M} is called the magnetization. In this equation, time derivative of the electric field can be dropped because that term is very small working at the low frequencies and short ranges of the proposed problem. Now, recall that for a linear, isotropic, ferrous material that

$$\vec{M} = \frac{\mu_r - 1}{\mu_0 \mu_r} \vec{B} \quad (125)$$

substituting this into Maxwell's Equation yields

$$\begin{aligned} \nabla \times \vec{B} - \frac{\mu_r - 1}{\mu_r} \nabla \times \vec{B} &= \mu_0 \vec{J}_f \\ \nabla \times \vec{B} &= \mu_0 \mu_r \vec{J}_f \end{aligned} \quad (126)$$

This result is obtained in Lorrain and Corson [11] and is used in Hammond's paper [1]. Maxwell's equation states the physical result that the presence of the magnetic field in the slab does two things, it magnetizes the slab and it generates free currents. The magnetization is in phase with the applied field, which should eventually yield an attractive force and the currents are in quadrature. After simplifying to obtain the above expression, it appears that the net result is that small free currents are associated with large magnetic fields. It will be interesting to see where this ends up.

Using these, the differential equation for the vector potential in the slab becomes

$$\nabla \times \nabla \times \vec{A} = \mu_0 \mu_r \vec{J} = \mu_0 \mu_r \sigma \vec{E} = -\mu_0 \mu_r \sigma \frac{\partial \vec{A}}{\partial t}. \quad (127)$$

Now assume the coil current is varying sinusoidally, $I(t) = I \cos(\omega t)$, causing the vector potential to also vary sinusoidally and allowing it to be expressed as

$$\vec{A}(\rho, z, t) = \frac{\vec{A}(\rho, z) e^{i\omega t} + \vec{A}^*(\rho, z) e^{-i\omega t}}{2} \quad (128)$$

There is a phase difference between the current and the vector potential that will cause $\vec{A}(\rho, z)$ to be complex, but when we calculate forces we will need to multiply the vector potential times the current and this multiplication can only be done between real terms, not complex ones. Consequently, it must be kept in mind that before this multiplication can be performed that the above formula must be used to recover the real version of the vector potential. So using $\vec{A}(\rho, z) e^{i\omega t}$ as the form for the vector potential, the differential equation in the slab becomes

$$-\nabla \times \nabla \times \vec{A} = \frac{\partial^2 \vec{A}}{\partial \rho^2} + \frac{\partial^2 \vec{A}}{\partial z^2} + \frac{1}{\rho} \frac{\partial \vec{A}}{\partial \rho} - \frac{\vec{A}}{\rho^2} = i\omega \mu_0 \mu_r \sigma \vec{A}. \quad (129)$$

The coefficient $\omega \mu_0 \mu_r \sigma$ can be significant. Aluminum has a conductivity of about 4×10^7 A/(V-m) and if the frequency is 50 Hz this coefficient is about $16,000 \text{ m}^{-2}$. Also, μ_r can be as large, for iron $\mu_r \approx 10^3$.

As was the case with the isolated coil, the currents and therefore the magnetic vector potential are only in the $\hat{\phi}$ direction. So, $\vec{A} = A(\rho, z)\hat{\phi}$, allowing Eq. 129 to be written in scalar form. Then, using separation of variables, $A(\rho, z) = A_\rho(\rho) A_z(z)$, yields the differential equation

$$\begin{aligned} (A_\rho'' + A_\rho'/\rho - A_\rho/\rho^2)/A_\rho + A_z''/A_z &= i\omega \mu_0 \mu_r \sigma \\ (A_\rho'' + A_\rho'/\rho - A_\rho/\rho^2)/A_\rho &= -\alpha^2 = -A_z''/A_z + i\omega \mu_0 \mu_r \sigma \end{aligned} \quad (130)$$

Solving this yields the solution for a specific α

$$A(\rho, z) = \left(D e^{z\sqrt{\alpha^2 + i\omega \mu_0 \mu_r \sigma}} + E e^{-z\sqrt{\alpha^2 + i\omega \mu_0 \mu_r \sigma}} \right) J_1(\alpha \rho), \quad (131)$$

and the general solution for the vector potential within the slab

$$A(\rho, z) = \int_0^\infty \left(D(\alpha) e^{z\sqrt{\alpha^2 + i\omega \mu_0 \mu_r \sigma}} + E(\alpha) e^{-z\sqrt{\alpha^2 + i\omega \mu_0 \mu_r \sigma}} \right) J_1(\alpha \rho) d\alpha. \quad (132)$$

Using the expressions obtained for the isolated coil, there are now four general solutions, for four different regions of space.

$$A(\rho, z) = \begin{cases} \int_0^\infty C(\alpha) e^{\alpha d} e^{-\alpha z} J_1(\alpha \rho) d\alpha, & z > d \\ \int_0^\infty (F(\alpha) e^{\alpha d} e^{-\alpha z} + G(\alpha) e^{-\alpha d} e^{\alpha z}) J_1(\alpha \rho) d\alpha, & 0 < z < d \\ \int_0^\infty \left(D(\alpha) e^{z\sqrt{\alpha^2 + i\omega \mu_0 \mu_r \sigma}} + E(\alpha) e^{-z\sqrt{\alpha^2 + i\omega \mu_0 \mu_r \sigma}} \right) J_1(\alpha \rho) d\alpha, & -s < z < 0 \\ \int_0^\infty H(\alpha) e^{\alpha z} J_1(\alpha \rho) d\alpha, & z < -s \end{cases} \quad (133)$$

Across each interface the vector potential is continuous and, since the slab is magnetic, the tangential components of the magnetic field, $H_\rho = -(1/(\mu_0\mu_r))\partial A/\partial z$, are continuous on each slab interface. This yields five boundary conditions for the six unknown functions. The sixth boundary condition comes from the coil itself. Starting with the continuity condition and letting $\alpha_1 = \sqrt{\alpha^2 + i\omega\mu_0\mu_r\sigma}$ (we assume α_1 is in the quadrant where both its real and imaginary components are greater than zero) we obtain

$$\begin{aligned} C(\alpha) &= F(\alpha) + G(\alpha) \\ F(\alpha)e^{\alpha d} + G(\alpha)e^{-\alpha d} &= D(\alpha) + E(\alpha) \\ D(\alpha)e^{-\alpha_1 s} + E(\alpha)e^{\alpha_1 s} &= H(\alpha)e^{-\alpha s}. \end{aligned} \quad (134)$$

The two magnetic field conditions across the slab surfaces yield

$$\begin{aligned} -\alpha F(\alpha)e^{\alpha d} + \alpha G(\alpha)e^{-\alpha d} &= (\alpha_1 D(\alpha) - \alpha_1 E(\alpha))/\mu_r \\ (\alpha_1 D(\alpha)e^{-\alpha_1 s} - \alpha_1 E(\alpha)e^{\alpha_1 s})/\mu_r &= \alpha H(\alpha)e^{-\alpha s}. \end{aligned} \quad (135)$$

Across the coil we have

$$\left. \frac{\partial A(\rho, z, t)}{\partial z} \right|_{z=d+\epsilon} - \left. \frac{\partial A(\rho, z, t)}{\partial z} \right|_{z=d-\epsilon} = -\mu_0 I(t) \delta(\rho - r). \quad (136)$$

But we need a boundary condition form for $A(\rho, z)$, i.e., with the time dependence removed. Using the expression for $A(\rho, z, t)$ given in Eq. 128 and expanding $I(t) = I \cos(\omega t)$ allows such a condition to be found:

$$\begin{aligned} \left. \frac{\partial (A(\rho, z)e^{i\omega t} + A^*(\rho, z)e^{-i\omega t})}{2\partial z} \right|_{z=d+\epsilon} - \left. \frac{\partial (A(\rho, z)e^{i\omega t} + A^*(\rho, z)e^{-i\omega t})}{2\partial z} \right|_{z=d-\epsilon} \\ = -\mu_0 I \frac{e^{i\omega t} + e^{-i\omega t}}{2} \delta(\rho - r) \end{aligned} \quad (137)$$

Rearranging terms to separate the time dependence gives:

$$\left(\left. \frac{\partial A(\rho, z)}{\partial z} \right|_{z=d+\epsilon} - \left. \frac{\partial A(\rho, z)}{\partial z} \right|_{z=d-\epsilon} \right) \frac{e^{i\omega t}}{2} + cc = -\mu_0 I \frac{e^{i\omega t}}{2} \delta(\rho - r) + cc, \quad (138)$$

where cc is the complex conjugate of each side of the equation. This can be further simplified to a time independent form:

$$\left. \frac{\partial A(\rho, z)}{\partial z} \right|_{z=d+\epsilon} - \left. \frac{\partial A(\rho, z)}{\partial z} \right|_{z=d-\epsilon} = -\mu_0 I \delta(\rho - r) \quad (139)$$

Substituting this into the first two general solutions in Eq. 132 gives:

$$\int_0^\infty (- (C(\alpha) + G(\alpha))e^{-\alpha\epsilon} + F(\alpha)e^{\alpha\epsilon}) J_1(\alpha\rho) \alpha d\alpha = -\mu_0 I \delta(\rho - r). \quad (140)$$

Now use the orthogonality integral relationship $\int_0^\infty J_1(\beta\rho) J_1(\alpha\rho) \rho d\rho = (1/\alpha)\delta(\beta - \alpha)$ to obtain:

$$\begin{aligned} \int_0^\infty J_1(\beta\rho) \int_0^\infty (- (C(\alpha) + G(\alpha)) e^{-\alpha\epsilon} + F(\alpha) e^{\alpha\epsilon}) J_1(\alpha\rho) \alpha d\alpha \rho d\rho \\ = - \int_0^\infty J_1(\beta\rho) \mu_0 I \delta(\rho - r) \rho d\rho. \end{aligned} \quad (141)$$

This then reduces to

$$\int_0^\infty (- (C(\alpha) + G(\alpha)) e^{-\alpha\epsilon} + F(\alpha) e^{\alpha\epsilon}) \delta(\beta - \alpha) d\alpha = -J_1(\beta r) r \mu_0 I. \quad (142)$$

Evaluating the final integral results in

$$- (C(\beta) + G(\beta)) e^{-\beta\epsilon} + F(\beta) e^{\beta\epsilon} = -J_1(\beta r) r \mu_0 I. \quad (143)$$

Letting ϵ go to zero and changing variables gives the last expression needed to find the full solution:

$$C(\alpha) + G(\alpha) - F(\alpha) = J_1(\alpha r) r \mu_0 I. \quad (144)$$

Solving these six equations for the coefficient functions yields:

$$\begin{aligned} C(\alpha) &= \mu_0 I r \frac{J_1(\alpha r)}{2} \left(1 + \frac{(\mu_r^2 \alpha^2 - \alpha_1^2) e^{-2\alpha d} (e^{\alpha_1 s} - e^{-\alpha_1 s})}{(\mu_r \alpha + \alpha_1)^2 e^{\alpha_1 s} - (\mu_r \alpha - \alpha_1)^2 e^{-\alpha_1 s}} \right) \\ F(\alpha) &= \mu_0 I r \frac{J_1(\alpha r)}{2} \left(\frac{(\mu_r^2 \alpha^2 - \alpha_1^2) e^{-2\alpha d} (e^{\alpha_1 s} - e^{-\alpha_1 s})}{(\mu_r \alpha + \alpha_1)^2 e^{\alpha_1 s} - (\mu_r \alpha - \alpha_1)^2 e^{-\alpha_1 s}} \right) \\ G(\alpha) &= \mu_0 I r \frac{J_1(\alpha r)}{2} \\ D(\alpha) &= \mu_0 \mu_r I r J_1(\alpha r) \left(\frac{\alpha (\alpha_1 + \mu_r \alpha) e^{\alpha_1 s - \alpha d}}{(\mu_r \alpha + \alpha_1)^2 e^{\alpha_1 s} - (\mu_r \alpha - \alpha_1)^2 e^{-\alpha_1 s}} \right) \\ E(\alpha) &= \mu_0 \mu_r I r J_1(\alpha r) \left(\frac{\alpha (\alpha_1 - \mu_r \alpha) e^{-\alpha_1 s - \alpha d}}{(\mu_r \alpha + \alpha_1)^2 e^{\alpha_1 s} - (\mu_r \alpha - \alpha_1)^2 e^{-\alpha_1 s}} \right) \\ H(\alpha) &= \mu_0 \mu_r I r J_1(\alpha r) \left(\frac{2\alpha \alpha_1 e^{\alpha(s-d)}}{(\mu_r \alpha + \alpha_1)^2 e^{\alpha_1 s} - (\mu_r \alpha - \alpha_1)^2 e^{-\alpha_1 s}} \right) \end{aligned} \quad (145)$$

These expressions combined with Eq. 132 yield the complete description of the time-independent portion of the vector potential. If $\alpha_1 = \alpha$, i.e., the slab is non-conducting or the frequency is very small, these expressions reduce to the same vector potential as found for the isolated coil.

3.1.2 The Force on the Coil

Now consider the force on the coil due to the presence of the slab. The force on an element of the coil is given by $d\vec{F} = I(t)d\vec{l} \times \vec{B}$. Since we are only interested in the total force along the z axis, and since $d\vec{l}$ points in the $\hat{\phi}$ direction, only the radial components of the magnetic field contribute, resulting in $dF\hat{z} = -I(t)dlB_\rho\hat{z}$. Integrating around the coil's circumference yields:

$$\vec{F} = -I(t)2\pi r B_\rho(r, d, t)\hat{z} = I(t)2\pi r \frac{\partial A(r, d, t)}{\partial z}\hat{z}, \quad (146)$$

where $B_\rho(r, d, t)$ is the radial component of the magnetic field on the coil and where $\partial A(r, d, t)/\partial z$ is the derivative of A with respect to z and evaluated at $\rho = r$ and $z = d$. From Eq. 128

$$\frac{\partial A(r, d, t)}{\partial z} = \left(\frac{\partial A(r, d)}{\partial z} e^{i\omega t} + \frac{\partial A^*(r, d)}{\partial z} e^{-i\omega t} \right) / 2. \quad (147)$$

This results in a force on the coil given by

$$\vec{F} = I \cos(\omega t) 2\pi r \left(\frac{\partial A(r, d)}{\partial z} e^{i\omega t} + \frac{\partial A^*(r, d)}{\partial z} e^{-i\omega t} \right) / 2\hat{z}. \quad (148)$$

We are only interested in the steady state force so we can average the time dependence over a cycle which will leave

$$\vec{F}_{avg} = I\pi r \left(\frac{\partial A(r, d)}{\partial z} + \frac{\partial A^*(r, d)}{\partial z} \right) / 2\hat{z}. \quad (149)$$

From the above expressions we know that

$$A(\rho, z) = \begin{cases} \int_0^\infty C(\alpha) e^{\alpha d} e^{-\alpha z} J_1(\alpha \rho) d\alpha, & z > d \\ \int_0^\infty (F(\alpha) e^{\alpha d} e^{-\alpha z} + G(\alpha) e^{-\alpha d} e^{\alpha z}) J_1(\alpha \rho) d\alpha, & 0 < z < d. \end{cases} \quad (150)$$

Taking the derivatives yields,

$$\frac{\partial A(\rho, z)}{\partial z} = \begin{cases} \int_0^\infty -\alpha C(\alpha) e^{\alpha d} e^{-\alpha z} J_1(\alpha \rho) d\alpha, & z > d \\ \int_0^\infty (-\alpha F(\alpha) e^{\alpha d} e^{-\alpha z} + \alpha G(\alpha) e^{-\alpha d} e^{\alpha z}) J_1(\alpha \rho) d\alpha, & 0 < z < d. \end{cases} \quad (151)$$

Now let $z = d + \epsilon$ when $z > d$ and $z = d - \epsilon$ when $0 < z < d$ to obtain

$$\begin{aligned} \frac{\partial A(\rho, d + \epsilon)}{\partial z} &= \int_0^\infty -\alpha C(\alpha) e^{-\alpha \epsilon} J_1(\alpha \rho) d\alpha \\ \frac{\partial A(\rho, d - \epsilon)}{\partial z} &= \int_0^\infty (-\alpha F(\alpha) e^{\alpha \epsilon} + \alpha G(\alpha) e^{-\alpha \epsilon}) J_1(\alpha \rho) d\alpha. \end{aligned} \quad (152)$$

Now use the expression $C(\alpha) = F(\alpha) + G(\alpha)$

$$\begin{aligned}\frac{\partial A(\rho, d + \epsilon)}{\partial z} &= \int_0^\infty (-\alpha F(\alpha)e^{-\alpha\epsilon} - \alpha G(\alpha)e^{-\alpha\epsilon}) J_1(\alpha\rho) d\alpha \\ \frac{\partial A(\rho, d - \epsilon)}{\partial z} &= \int_0^\infty (-\alpha F(\alpha)e^{\alpha\epsilon} + \alpha G(\alpha)e^{-\alpha\epsilon}) J_1(\alpha\rho) d\alpha.\end{aligned}\quad (153)$$

The $G(\alpha)$ terms correspond to the vector potential gradient due to the current in the coil itself. As was discussed earlier, these two terms are of opposite sign and cancel each other. The remaining term corresponds to the vector potential gradient from the slab and is given by

$$\frac{\partial A(\rho, d)}{\partial z} = \int_0^\infty -\alpha F(\alpha) J_1(\alpha\rho) d\alpha. \quad (154)$$

On the coil itself, this becomes

$$\frac{\partial A(r, d)}{\partial z} = \int_0^\infty -\alpha F(\alpha) J_1(\alpha r) d\alpha. \quad (155)$$

Combining this with Eq. 149, the force on the coil due to the slab is given by

$$\vec{F}_{avg} = -\frac{I\pi r}{2} \int_0^\infty \alpha (F(\alpha) + F^*(\alpha)) J_1(\alpha r) d\alpha \hat{z}, \quad (156)$$

where

$$F(\alpha) = \mu_0 I r \frac{J_1(\alpha r)}{2} \left(\frac{(\mu_r^2 \alpha^2 - \alpha_1^2) e^{-2\alpha d} (e^{\alpha_1 s} - e^{-\alpha_1 s})}{(\mu_r \alpha + \alpha_1)^2 e^{\alpha_1 s} - (\mu_r \alpha - \alpha_1)^2 e^{-\alpha_1 s}} \right) \quad (157)$$

and

$$\alpha_1 = \sqrt{\alpha^2 + i\omega\mu_0\mu_r\sigma}. \quad (158)$$

If $\mu_r = 1$ the coefficient to the $F(\alpha)$ function has a factor of $\alpha^2 - \alpha_1^2 = -i\omega\mu_0\sigma$.

3.1.3 Mathematica and COMSOL Force Models for a Coil Facing a Ferrous Slab

A Mathematica model was constructed for the force equation in the previous section to illustrate the behavior of the forces between an AC driven coil and a slab as a function of frequency and permeability. The coil uses the same parameters as giving in the example for the single coil facing a conductive slab. Since iron has a lower conductivity than aluminum, a value of 1×10^{-7} S/m is assumed for the slab. The slab thickness is assumed to be 1.5 mm to keep it light weight for space applications. The result is shown below in Figure 13.

The same coil and slab parameters were used to build a model in COMSOL. This was done to see how the analytical mathematics would compare to a finite element model (FEM). The results are shown in Figure 14. The COMSOL model produced results slightly smaller than the analytic model due to the mesh density in the slab. Increasing the density further would bring the results closer together

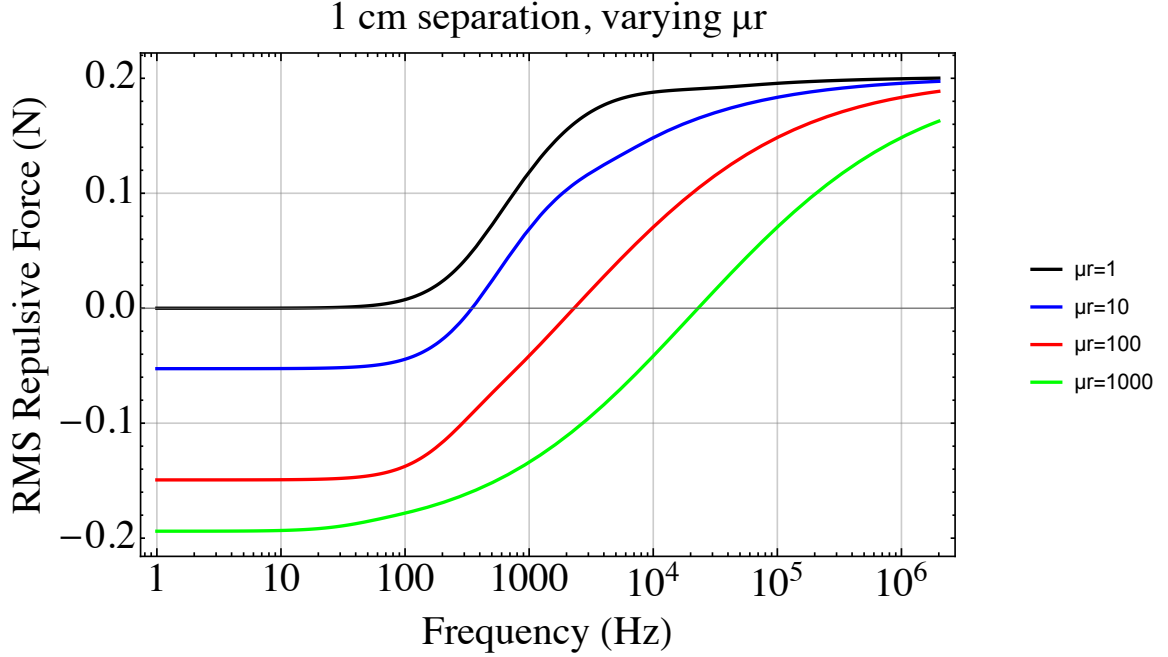


Figure 13. Semi-log plots showing the repulsive forces between a coil and a ferrous slab for multiple permeabilities over a broad frequency range. The separation between the slab and the face of the solenoid is 1 cm.

but the expense of excessive computation time. At least for this case, the analytic code runs much faster than the FEM in COMSOL.

3.2 Single Coil Facing a Stack of Two Conductive and/ or Ferrous Slabs

3.2.1 The Vector Potential and Force on the Coil

Place the coil a distance d from the surface of the composite slab, facing the slab with the z axis aligned with the center of of the coil. Let the first slab be thickness s_1 , and have conductivity, σ_1 , and relative permeability, μ_{r1} . Let the second slab be pressed against the first slab and be thickness s_2 , and have conductivity, σ_2 , and relative permeability, μ_{r2} .

$$A(\rho, z) = \begin{cases} \int_0^\infty C(\alpha) e^{\alpha d} e^{-\alpha z} J_1(\alpha \rho) d\alpha, & z > d \\ \int_0^\infty (F(\alpha) e^{\alpha d} e^{-\alpha z} + G(\alpha) e^{-\alpha d} e^{\alpha z}) J_1(\alpha \rho) d\alpha, & 0 < z < d \\ \int_0^\infty \left(D(\alpha) e^{z\sqrt{\alpha^2 + i\omega\mu_0\mu_{r1}\sigma_1}} + E(\alpha) e^{-z\sqrt{\alpha^2 + i\omega\mu_0\mu_{r1}\sigma_1}} \right) J_1(\alpha \rho) d\alpha, & -s_1 < z < 0 \\ \int_0^\infty \left(M(\alpha) e^{z\sqrt{\alpha^2 + i\omega\mu_0\mu_{r2}\sigma_2}} + N(\alpha) e^{-z\sqrt{\alpha^2 + i\omega\mu_0\mu_{r2}\sigma_2}} \right) J_1(\alpha \rho) d\alpha, & -s_1 - s_2 < z < -s_1 \\ \int_0^\infty H(\alpha) e^{\alpha z} J_1(\alpha \rho) d\alpha, & z < -s_1 - s_2 \end{cases} \quad (159)$$

Copying the approach from above where the vector potential and transverse field

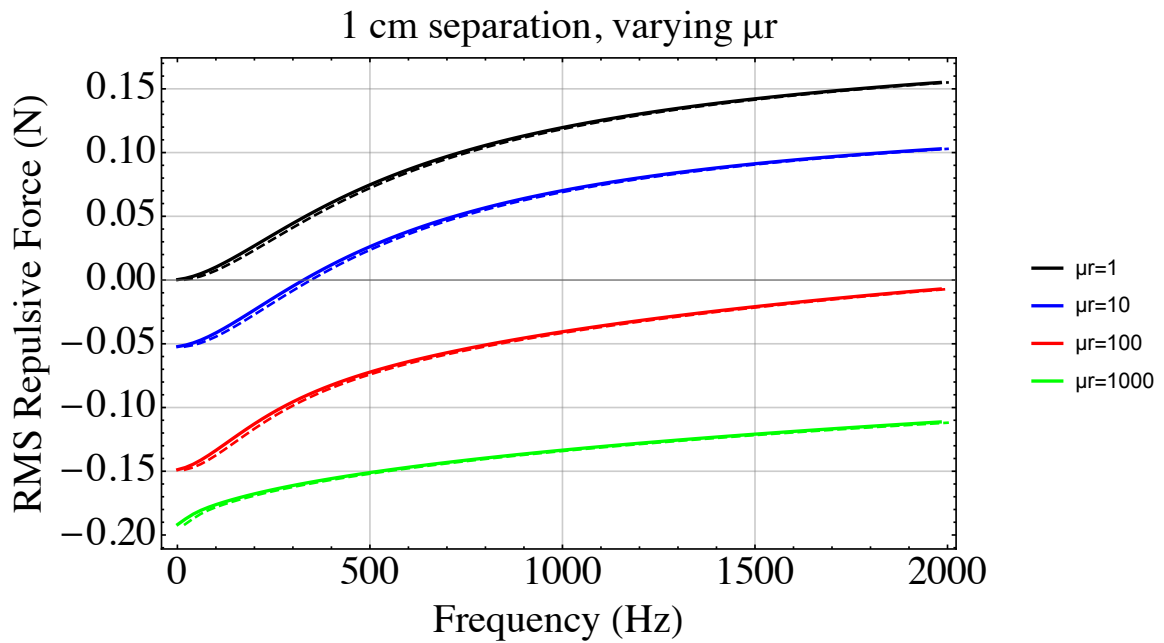


Figure 14. Plots comparing results computed from the analytic expression derived above and a COMSOL FEM model. The models were each used to compute the repulsive forces between a coil and a ferrous slab for multiple permeabilities. The analytic expressions are shown as a continuous line and the COMSOL results are shown as a dashed line. The separation between the slab and the face of the solenoid is 1 cm.

must be continuous across each boundary yields the following boundary condition equations,

$$\begin{aligned}
C(\alpha) &= F(\alpha) + G(\alpha) \\
F(\alpha) e^{\alpha d} + G(\alpha) e^{-\alpha d} &= D(\alpha) + E(\alpha) \\
D(\alpha) e^{-\alpha_1 s_1} + E(\alpha) e^{\alpha_1 s_1} &= M(\alpha) e^{-\alpha_2 s_1} + N(\alpha) e^{\alpha_2 s_1} \\
M(\alpha) e^{-\alpha_2(s_1+s_2)} + N(\alpha) e^{\alpha_2(s_1+s_2)} &= H(\alpha) e^{-\alpha(s_1+s_2)} \\
-\alpha F(\alpha) e^{\alpha d} + \alpha G(\alpha) e^{-\alpha d} &= (\alpha_1 D(\alpha) - \alpha_1 E(\alpha))/\mu_{r1} \\
(\alpha_1 D(\alpha) e^{-\alpha_1 s_1} - \alpha_1 E(\alpha) e^{\alpha_1 s_1})/\mu_{r1} &= (\alpha_2 M(\alpha) e^{-\alpha_2 s_1} - \alpha_2 N(\alpha) e^{\alpha_2 s_1})/\mu_{r2} \\
(\alpha_2 M(\alpha) e^{-\alpha_2(s_1+s_2)} - \alpha_2 N(\alpha) e^{\alpha_2(s_1+s_2)})/\mu_{r2} &= \alpha H(\alpha) e^{-\alpha(s_1+s_2)}.
\end{aligned} \tag{160}$$

where

$$\begin{aligned}
\alpha_1 &= \sqrt{\alpha^2 + i\omega\mu_0\mu_{r1}\sigma_1} \\
\alpha_2 &= \sqrt{\alpha^2 + i\omega\mu_0\mu_{r2}\sigma_2}.
\end{aligned} \tag{161}$$

The last boundary condition comes from the coil itself (see the derivation of this above)

$$C(\alpha) + G(\alpha) - F(\alpha) = J_1(\alpha r) r \mu_0 I. \tag{162}$$

These eight equations can be solved for the eight functions, but only the $F(\alpha)$ function is needed to obtain the force exerted on the coil due to the presence of the slabs.

$$F(\alpha) = J_1(\alpha r) r \mu_0 I e^{-2\alpha d} \frac{F_{num}(\alpha)}{2F_{den}(\alpha)} \tag{163}$$

$$\begin{aligned}
F_{num}(\alpha) &= \exp[\alpha_1 s_1 - \alpha_2 s_2](\alpha_1 - \alpha \mu_{r1})(-\alpha_2 + \alpha \mu_{r2})(-\alpha_2 \mu_{r1} + \alpha_1 \mu_{r2}) \\
&+ \exp[-\alpha_1 s_1 + \alpha_2 s_2](\alpha_1 + \alpha \mu_{r1})(\alpha_2 + \alpha \mu_{r2})(-\alpha_2 \mu_{r1} + \alpha_1 \mu_{r2}) \\
&+ \exp[-\alpha_1 s_1 - \alpha_2 s_2](\alpha_1 + \alpha \mu_{r1})(\alpha_2 - \alpha \mu_{r2})(\alpha_2 \mu_{r1} + \alpha_1 \mu_{r2}) \\
&+ \exp[\alpha_1 s_1 + \alpha_2 s_2](\alpha_1 - \alpha \mu_{r1})(\alpha_2 + \alpha \mu_{r2})(\alpha_2 \mu_{r1} + \alpha_1 \mu_{r2}) \\
F_{den}(\alpha) &= \exp[\alpha_1 s_1 - \alpha_2 s_2](\alpha_1 + \alpha \mu_{r1})(-\alpha_2 + \alpha \mu_{r2})(\alpha_2 \mu_{r1} - \alpha_1 \mu_{r2}) \\
&+ \exp[-\alpha_1 s_1 + \alpha_2 s_2](\alpha_1 - \alpha \mu_{r1})(\alpha_2 + \alpha \mu_{r2})(\alpha_2 \mu_{r1} - \alpha_1 \mu_{r2}) \\
&+ \exp[-\alpha_1 s_1 - \alpha_2 s_2](\alpha_1 - \alpha \mu_{r1})(-\alpha_2 + \alpha \mu_{r2})(\alpha_2 \mu_{r1} + \alpha_1 \mu_{r2}) \\
&+ \exp[\alpha_1 s_1 + \alpha_2 s_2](\alpha_1 + \alpha \mu_{r1})(\alpha_2 + \alpha \mu_{r2})(\alpha_2 \mu_{r1} + \alpha_1 \mu_{r2})
\end{aligned} \tag{164}$$

The force on the coil is then given by

$$\vec{F}_{avg} = -\frac{I\pi r}{2} \int_0^\infty \alpha (F(\alpha) + F^*(\alpha)) J_1(\alpha r) d\alpha \hat{z}, \tag{165}$$

3.2.2 Mathematica and COMSOL Force Models for a Coil Facing a Conductive Slab Over a Ferrous Slab

A Mathematica model was constructed for the force equation in the previous section to illustrate the behavior of the forces between an AC driven coil and a two slab configuration as a function of frequency and permeability. The slab closest to the coil face is assumed to be 1.5 mm thick aluminum. The second slab is underneath the first and is assumed to be 1.5 mm thick with a conductivity of 1×10^{-7} S/m but with varying permeability. The coil is uses the same parameters as giving in the example for the single coil facing a conductive slab. The result is shown below in Figure 15. The same configuration was modeled in COMSOL. However, the results

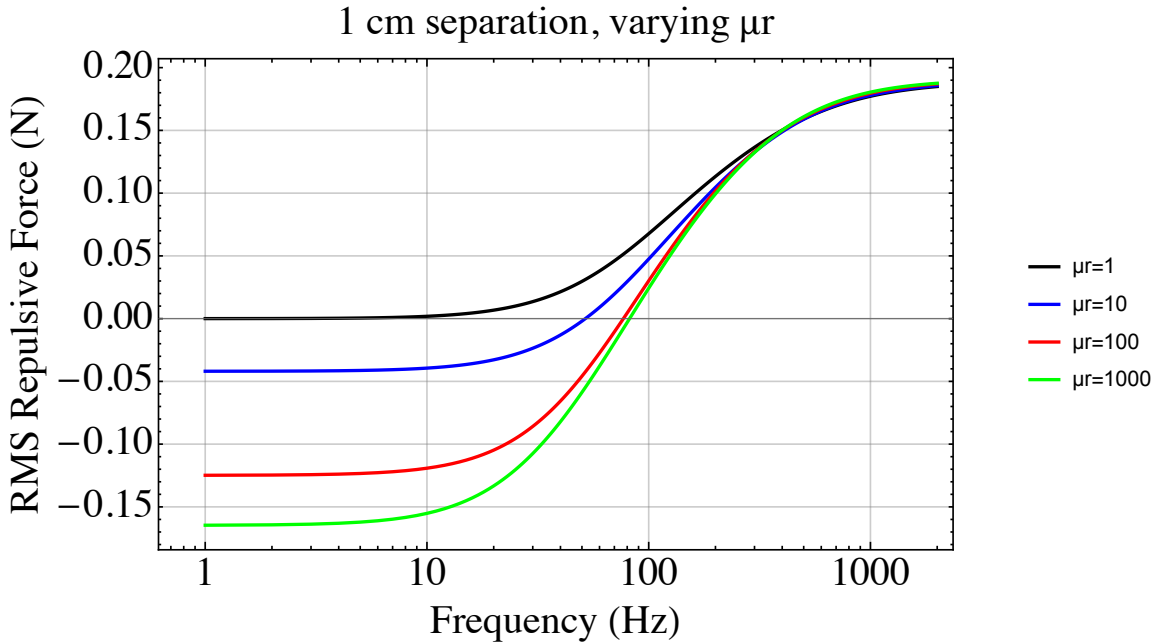


Figure 15. Semi-log plots showing the repulsive forces between a coil and an aluminum slab over a ferrous slab for multiple permeabilities over a range of frequencies. The separation between the slab and the face of the solenoid is 1 cm.

were so close to the curves shown in Figure 15 that they overlap and are therefore not shown.

Comparing the results from the all iron slab and the two slab case (Figures 13 and 15) shows the benefit of adding the aluminum slab. The transition between attractive and repulsive force now occurs at a much lower frequency. For iron, the transition moves from almost 30 kHz down to somewhere around 70-80 Hz. These lower frequencies are much easier to drive a solenoid at high currents as the proximity effect and skin depth both will raise the resistance at higher frequencies. By varying frequency between 30-200 Hz, it's possible to go from 100 mN of attractive force to 100 mN of repulsive force. This provides a means to construct a docking and undocking actuator for either another spacecraft or an iron core asteroid. For the

asteroid, an aluminum plate could be carried to repel off of when the mission is complete.

3.3 Two Coils Facing a Stack of Two Conductive and/ or Ferrous Slabs

3.3.1 Problem Setup and Force Solution

In this section a second current loop is added. The first current loop, located as in the previous sections, is now considered to be a drive loop that generates the vector potential and the eddy currents in the plate. It is driven with the same current as before, $I(t) = I \cos \omega t$. The second current loop is also driven with an oscillating current of the same frequency, but different phase than the drive coil, $I_2(t) = I_2 \cos(\omega t + \varphi)$ and is not inductively coupled to the first loop, i.e. the power supply can overcome inductive voltages.

The drive coil, has radius r , is centered on the \hat{z} axis a distance d from the near surface of the plate, and faces the plate. The second coil also faces the plate, but is a distance d_2 from the front plate surface. The second coil is radius r_2 and it's center is a distance b along the \hat{x} axis from the center of the drive coil.

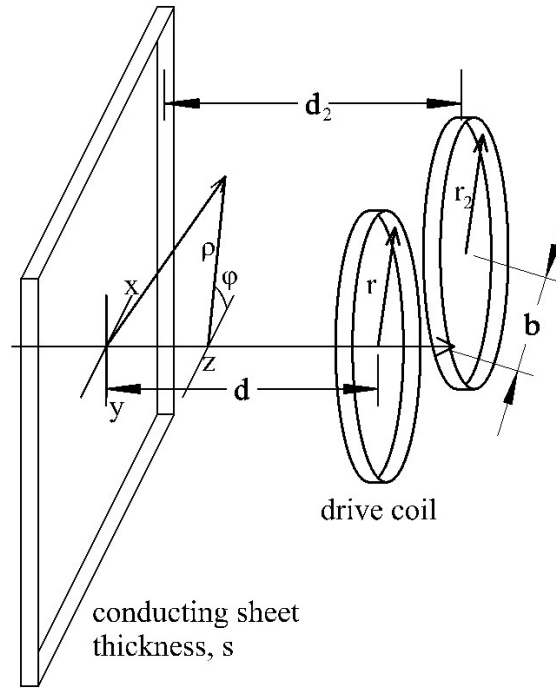


Figure 16. Two coils, one a drive coil and one under evaluation, are placed facing a conducting sheet. Both cylindrical and Cartesian coordinates are shown. A second conducting sheet with thickness s_2 is added behind the first. Additionally, both sheets are allowed to vary in permeability.

Section 2.3.2 derived the total longitudinal force on the second coil (including

the factor of 2) yielding Equation 64 which is repeated here for convenience:

$$F_x = \frac{I_2}{2} \int_0^\infty (F(\alpha)e^{-i\varphi} + F^*(\alpha)e^{i\varphi}) e^{\alpha(d-d_2)} \alpha \int_{b-r_2}^{b+r_2} \frac{(b-x)J_0(\alpha\sqrt{r_2^2 - b^2 + 2bx})}{\sqrt{r_2^2 - (x-b)^2}} dx d\alpha \quad (166)$$

$F(\alpha)$ is dependent on the eddy currents in the slab or slabs. Since we are now dealing with multiple slabs, it is now given by the combination of Equations 163 and 164. Likewise, the axial force, F_z , has the the same $F(\alpha)$ but now it is used in conjunction with Equation 76.

3.3.2 Mathematica Model of LIM Longitudinal and Axial Forces

A Mathematica model was created using similar parameters and methods as described in Subsections 2.3.3 and 2.3.5 but with the math model described above. Two parameters were fixed: the phase angle between adjacent coils was set to $\phi = \pi/2$ (quadrature) and an overlap of $b = r$, the coil radius. Figure 17 shows the result for a variety of permeabilities. When $\mu_r = 1$, the result is almost identical to the lower left plot shown in Figure 7 which has the same upper aluminum slab but no lower slab. The first important thing to note here is that the presence of the iron under the aluminum doesn't change the peak repulsive force but about doubles the longitudinal force. By zooming in on the lower frequencies, we can see

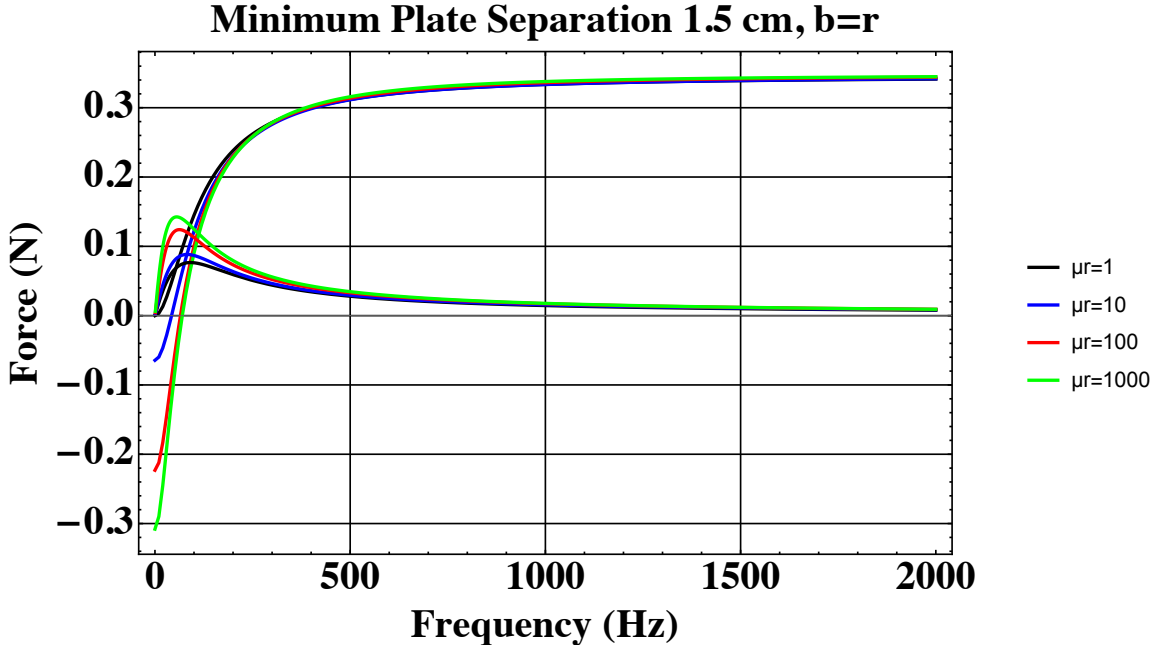


Figure 17. The longitudinal and z axis forces for a LIM facing an aluminum slab over an iron slab. The longitudinal force about doubles as μ_r approaches the value for iron of 1000, while the peak repulsive forces converge on the same value, regardless of μ_r .

the second important thing to note: The z axis forces transition from attractive to repulsive at a frequency where the longitudinal force is still significant. This allows for a frequency controlled LIM where longitudinal forces can be generated without attractive or repulsive forces also being present. Shifting the frequency by a few tens of Hertz allows you to also add in either an attractive or repulsive force. This is illustrated by the plots shown in Figure 18

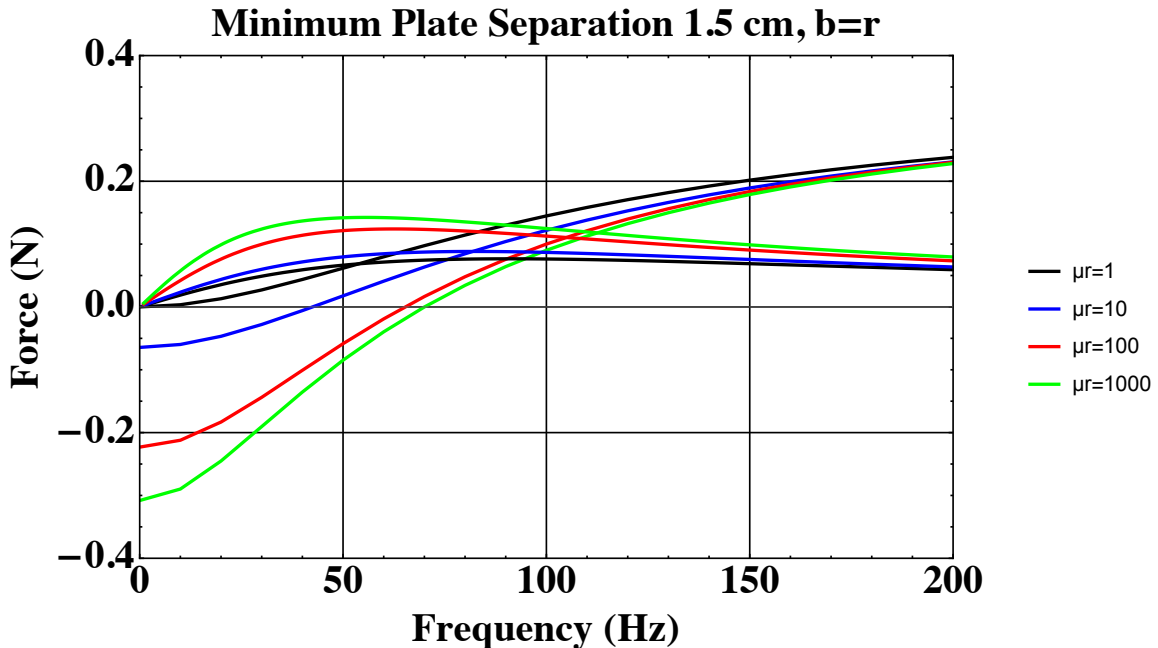


Figure 18. A zoomed in plot of the longitudinal and z axis forces for a LIM facing an aluminum slab over an iron slab. Note that the z axis force is zero at around 70 Hz when $\mu_r = 1000$, the case for iron. At 70 Hz, the longitudinal force is still large and the lack of forces in the \hat{z} direction allows for cross plane motion without requiring another compensating actuator. If the frequency is allowed to vary between 30-170 Hz, up to 200 mN of attractive or repulsive force can be added to the longitudinal force.

3.3.3 Comparison of Linear Induction Motor Forces using a Mathematica Simulation and a COMSOL Model for an Aluminum Slab on Top of a Ferrous Slab

A four coil linear induction model was constructed using our analytic approach in Mathematica and compared to a similar one constructed in the COMSOL Multiphysics program which uses finite elements to solve the mathematics in a discrete numeric method. For this comparison, the same four coil configuration that was modeled in Section 2.3.6 was used. The only difference now is that the aluminum slab is now 1.5 mm thick rather than 3.0 mm thick as in the previous example. Additionally, a 1.5 mm thick ferrous slab is placed under the aluminum slab. The

ferrous slab is assumed to have a conductivity of 1×10^7 S/m and a relative permeability of 1000. The comparison of the repulsive and lateral forces appear in the pair of plots shown in Figure 19.

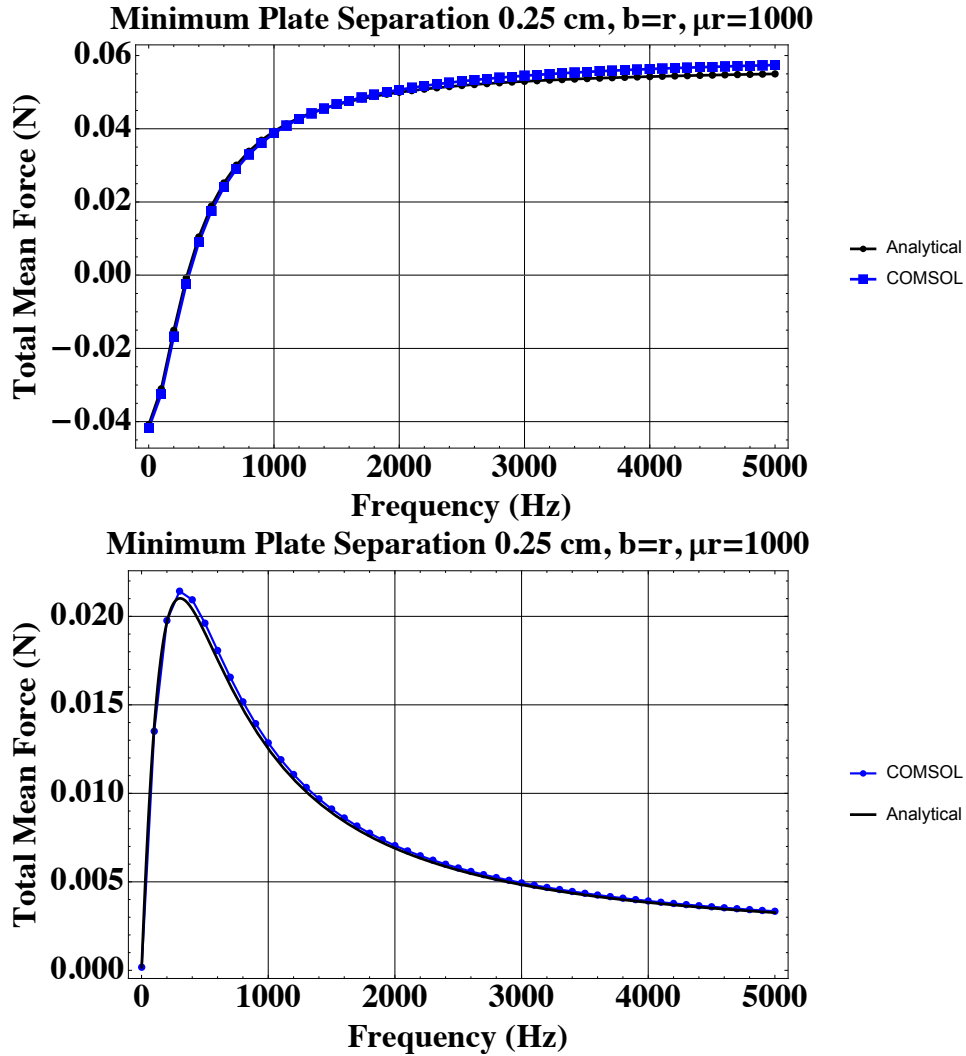


Figure 19. Plots showing a comparison between the analytical model and a COMSOL model when used to compute the longitudinal (top) and repulsive (bottom) forces with an aluminum slab over an iron slab for a four coil LIM driven in quadrature with a coil overlap equal to the radius. Slight differences occur due to the discrete nature of the finite elements used in the COMSOL model.

As mentioned in the case of the four coils opposite an aluminum slab, the differences between the two models are likely from the a combination of the discrete nature of the FEM model (mesh density) and the numeric approximation made in computing the results for the analytic model. It's interesting to note that operating at around 300 Hz will allow lognitudinal motion with no repulsive (or attractive)

force. Shifting the frequency up by 100 Hz will result in the addition of a repulsive force similar in magnitude to the longitudinal force, while shifting the frequency down 100 Hz results in the addition of an attractive force, again of similar magnitude to the longitudinal force.

The COMSOL model details for this LIM model appear in the Appendix.

4 AC Modulated Electrostatic Force Actuator

We initially looked into using magnetic means of generating the correct phase eddy currents in a conductive non-ferrous slab to get an attractive force as there is evidence in literature that this is possible [12–14]. After a short time exploring this option, we determined that if this is possible, it will require very large magnetic fields, high power, and mass. Since high power and mass are undesirable in spacecraft, we abandoned this approach and decided to explore an electrostatic approach to achieving an attractive force. What follows is a description of the math modeling and the experimental work done to test the model.

4.1 Force Between Plates of a Parallel Plate Capacitor

The attractive force is based on electrostatics and uses separation of charges using capacitive plates driven with high voltages but low currents. The charged capacitive plate closest to the ISS will result in mirror charges (equal but opposite) to form on the conductive metal skin of the ISS to cancel the electric field generated by the satellite spacecraft. This creates an attractive force between the two that will act to pull them together.

The electric field between a parallel pair of charged conductors is $\vec{E} = \frac{\sigma}{\epsilon_0} \hat{n}$ where ϵ_0 is the permittivity of free space (8.85×10^{-12} F/m), σ is the surface charge density, and \hat{n} is a unit vector normal to the surface of the more positively charged conductor. Capacitance is defined as $C = Q/V$, where Q is the total charge on the electrode and V is the potential difference between the electrode and a ground reference. For a square pair of parallel conductors, $V = \int_0^d \vec{E} \cdot d\vec{l} = \frac{\sigma}{\epsilon_0} d$, where d is the separation between electrodes. The charge density σ can be written as Q/s^2 where s is the length of the electrode. Substituting this in for V in the capacitance equation, we are left with the familiar form for the capacitance of a parallel plate capacitor: $C = \epsilon_0 \frac{s^2}{d}$. However, this formula is for an ideal capacitor and neglects edge effects and variations in the plate alignment that change the effective area of the electrode pair. The test electrodes we have selected for our experimental setup are 0.152 m on a side and $d \geq 0.01$ m. So, we will add a scale factor, f_s to account for the varying effects giving $C = f_s \epsilon_0 \frac{s^2}{d}$.

The force on each plate is toward the opposite plate where the magnitude is given by $F = U/d$, where the potential energy, $U = \frac{1}{2} CV^2$. These equations can be combined to yield $\vec{F} = -\frac{1}{2} f_s \epsilon_0 \frac{s^2}{d^2} V^2 \hat{x}$ where we have chosen the direction normal to the separation of the plates to be \hat{x} . To get a feel for the magnitude of this force, we use a square plate that is 0.152 m on a side (approximately 6 inches) and use 4242 V_{rms} for the voltage. Inserting these values into the force equation and assuming

an ideal capacitor where $f_s = 1$ produces the plot of force magnitude as a function of separation shown in Figure 20.

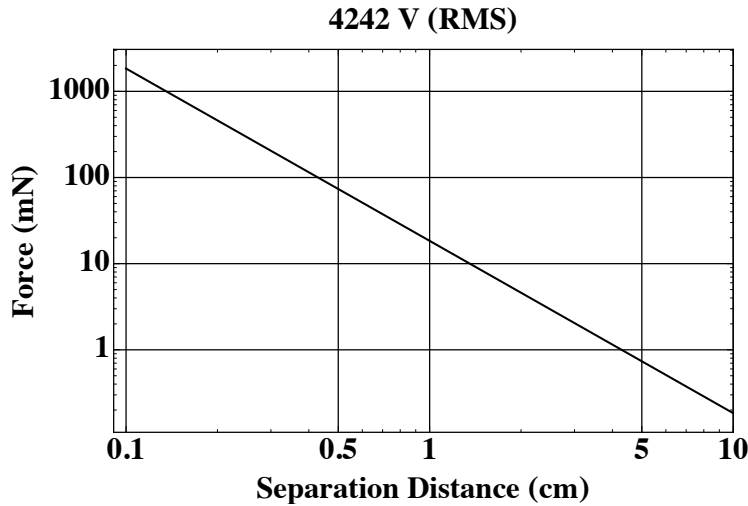


Figure 20. Computed electrostatic attractive force magnitude for a 15.2 cm on a side square plate charged with a 4242 V_{rms} source opposite an infinite conductor as a function of separation distance.

4.2 Electrostatic Force Experiment

4.2.1 Test Description

To test the attractive force, four equal sized square plates (0.152 m on a side) were cut out of aluminum sheet. Two are mounted to aluminum rods to create a balanced mobile that is free to pivot on a point. The other two plates are rigidly mounted in a parallel plate configuration with a 0.06 m separation giving them a capacitance of 3.4 pF. A DC-DC transformer (HVM part no. HVA0560) with a programable input was used to transform a low voltage function generator output to a high voltage low frequency signal of up to 12 kVpp or 4.2 kV RMS. A 10 Hz sine wave was used as the input for our experiments. Nylon standoffs are used to separate the plates and are also used as a stop (0.01 m) to keep the pivoting plates from directly contacting the charged capacitor. A photo of the test setup is shown below in Figure 21. One of the plates from the mobile was positioned a few centimeters from the capacitor and allowed to come to rest. A laser displacement sensor was used to determine the position of the plate with respect to the capacitor by monitoring the position of the plate being used as a counterweight. The output of the function generator was turned on and the data versus time was captured and stored on a laptop and later processed. The maximum force generated by our configuration should be around 18.5 mN for a plate separation of 1 cm and 4.2 kV RMS, but saw losses due to alignment errors that gave a correction scale factor of $f_s = 0.75$ reducing the maximum to about 13.9 mN. From the force expression it's easy to see that the

force goes as voltage squared, but falls off to 1/distance squared.

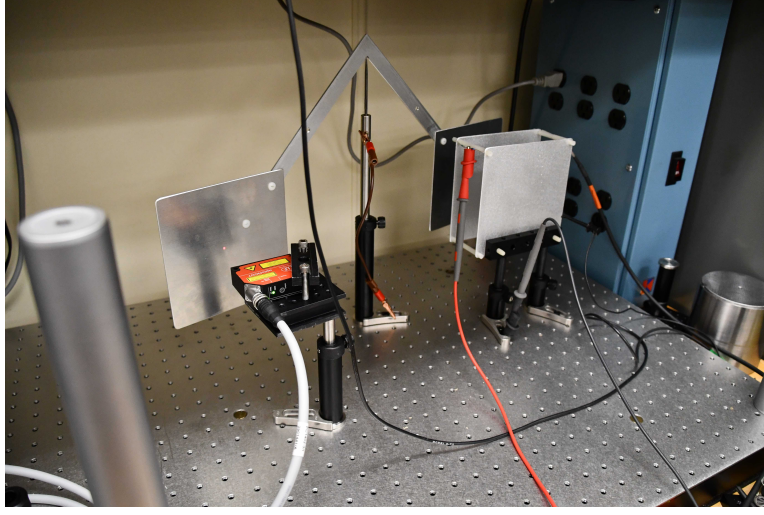


Figure 21. Electrostatic attraction test configuration showing a mobile balanced by two square plates. An optical displacement sensor is used to measure the movement of the plate on the left. The mobile servicing spacecraft is modeled by the parallel plate capacitor on the right hand side.

To see if the predicted force will match up with the position data, some additional math is needed. We have a rotating plate that is measured at a radius of r_2 from the pivot point. So, the torque, $\vec{\tau} = -r_2 F \hat{z} = -I \alpha \hat{z}$, where I is the moment of inertia of our rotating mobile and α is the angular acceleration. If we take our earlier expression for the force and let $c_1 = \frac{1}{2} f_s \epsilon_0 s^2 V^2$, $F = c_1 / d^2$. We then substitute this into our expression for torque and allow d to now be a variable, x yielding:

$$\tau(x) = r_2 \frac{c_1}{x^2} = I \alpha(x). \quad (167)$$

The angular acceleration can be rewritten in terms of the linear acceleration for small movements, $\alpha(x) = a(x)/r_2$. We then let $a(x) = \ddot{x}$ to denote the second time derivative of position, x . We then substitute and get

$$\tau(x) = r_2 \frac{c_1}{x^2} = I \ddot{x} / r_2. \quad (168)$$

Rearranging, we get:

$$\ddot{x} / x^2 = r_2^2 c_1 / I. \quad (169)$$

Since the right hand side of the equation is a constant, we'll now let $c_2 = r_2^2 c_1 / I$. Rearranging we get $\ddot{x} = c_2 / x^2$. We then multiply both sides by the velocity, \dot{x} and integrate with respect to time:

$$\int \ddot{x} \dot{x} dt = \int c_2 \frac{\dot{x}}{x^2} dt. \quad (170)$$

Performing the integrals gives the equation for velocity in terms of position and time:

$$\frac{1}{2}\dot{x}(t)^2 = -\frac{c_2}{x(t)} + c_3, \quad (171)$$

where c_3 is a constant from integration representing initial velocity. Rearranging and incorporating the proper direction we get

$$\dot{x}(t) = -\sqrt{\frac{2c_2}{x(t)} - 2c_3}. \quad (172)$$

We can then write a discrete version and using appropriate initial conditions, we can try to match the data. Using the discrete form $\dot{x}(t) \rightarrow \frac{x(n+1)-x(n)}{\Delta t}$, Equation 172 becomes

$$x(n+1) = x(n) - \Delta t \sqrt{\frac{2c_2}{x(n)} - 2c_3}. \quad (173)$$

For the initial conditions, we set $x(0)$ equal to the starting position. The constants c_1 and c_2 are calculated with the geometry, the computed moment of inertia, and applied voltage. If we assume that the starting velocity is zero, $c_3 = c_2/x(0)$. This gives us $x(1) = x(0)$ and subsequent values of $x(n)$ will all be the same unless we include a starting acceleration. Earlier, we found $\ddot{x}(t) = c_2/x(t)^2$. This too can be written in discrete form and used to find the starting acceleration:

$$\frac{x(n+1) - 2x(n) + x(n-1)}{\Delta t^2} = c_2/x^2(n). \quad (174)$$

Rearranging and seeking to find $x(2)$ and recalling $x(1) = x(0)$, we get

$$x(2) = c_2\Delta t^2/x(0)^2 + x(0). \quad (175)$$

In summary, we use our knowledge of the starting velocity (zero) and the starting acceleration (using Equations 174 and 175) to find the first three data points starting with the position just before voltage is applied to our capacitor. We then can use Equation 173 to compute each subsequent point using this recursion relationship. However, we are still missing one piece of data: the moment of inertia, I , for our test fixture. The next section will detail this computation.

4.2.2 Moment of Inertia Computation for Test Fixture

A dimensioned diagram of the mobile is shown with one of the plates removed in Figure 22. The moment of inertia is computed with the following volume integral:

$$I = \int_V \rho(x, y, z) \|\vec{r}\|^2 dV \quad (176)$$

where $\rho(x, y, z)$ is the spatially varying density of the material, \vec{r} is the vector from the rotation axis to a point in the material, and V is the volume of the part you are integrating over. Since our test fixture is created entirely from aluminum, we'll assume a uniform density of $\rho = 2800 \text{ kg/m}^3$. To compute the moment of inertia for

our test fixture, we'll break it up into three separate integrals. For the plate we'll use

$$I_{p1} = \rho d \int_{r_1}^{r_2} \int_0^h x^2 dy dx, \quad (177)$$

where d is the thickness of the plate (1.54 mm), $r_1 = 124.8$ mm is the radius from the center to the inner edge of the plate, $r_2 = 276.8$ mm is the radius to the outer edge of the plate, and $h = 152$ mm is the height of the plate. Plugging in these numbers in meters gives a moment of inertia for one plate as $I_{p1} = 0.00417$ kg·m².

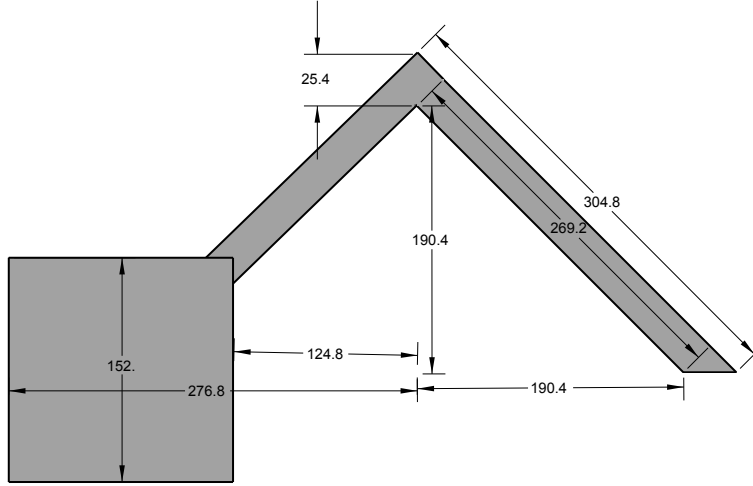


Figure 22. Drawing of test fixture with one plate removed. The dimensions are given in millimeters and are used to compute the moment of inertia. The thickness of the support frame is 3.11 mm and the thickness of the square plate is 1.54 mm

The angled support plate can be broken into two computations to find its moment of inertia. The first is given by

$$I_{p2} = \rho d_2 s_2 \int_0^{s_1} x^2 dx, \quad (178)$$

where $d_2 = 3.11$ mm gives the thickness of the support, $s_1 = 190.4$ mm is the distance from the center to the inner edge of of the support, and $s_2 = 25.4$ mm and represents the width of the support as shown in Figure 22. Computation shows that $I_{p2} = 0.00051$ kg·m². This leaves the small triangular section on the outermost section of the support plate. This moment of inertia is calculated by finding it for a square plate and dividing by two:

$$I_{p3} = \frac{\rho d_2 s_2}{2} \int_{s_1}^{s_1+s_2} x^2 dx. \quad (179)$$

After inserting our measurements shown in Figure 22, $I_{p3} = 0.00012$ kg·m². Summing the three moments of inertia and doubling it gives us the total moment of inertia for our test fixture, $I = 0.0096$ kg·m².

4.2.3 Test Results

We now have enough information to compute predicted position data as a function of the applied voltage and starting position. Two sets of results appear below in Figure 24 showing the close agreement between theory and experiment, if we assume a correction factor of $f_s = 0.75$.

It should be mentioned that there is a large reservoir of free charge in the aluminum skin covering the outside of the ISS. Charging plates on a servicing spacecraft will result in mirror charges being pulled from this reservoir to cancel the electric field generated by the servicing spacecraft electrodes. In our experiment in Figure 21, the mobile is connected via a grounding cable to the optical table to provide that reservoir to the plate. In the final experimental mobile shown in Figure 23, a drag wire was suspended from the mobile to provide this additional charge.

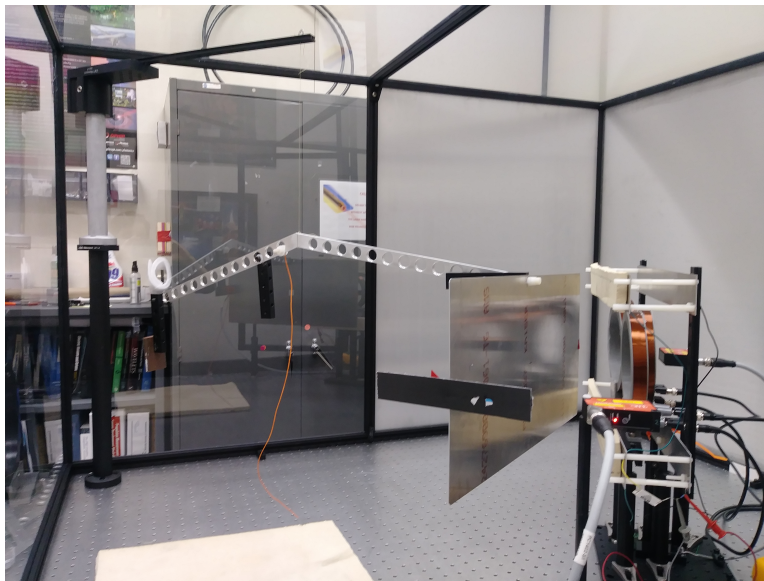


Figure 23. A photo showing a linear induction motor test setup for measuring lateral motion and force along with electrostatic actuators above and below the coils. A suspended drag wire is used to provide an adequate source of charge so the mobile can respond to the electrostatic actuators.

Another point that should be discussed is the choice of alternating the charges between the plates to create a changing electric field versus applying a DC voltage across the plates. In the vacuum of space, the ion density is quite low so that there would be no charge cancellation on the electrodes when using a DC voltage. However, at 400 km altitude, the ionosphere still has enough charge to cause cancellation of a static electric field. So, for testing purposes, our fields were varied at 10 Hz. Higher frequencies are possible but not with the electronics we used. It is possible that 10 Hz will be insufficient and the ionosphere will partially or totally shield the ISS from the electric field, but the initial analysis discussed below in Section 5 looks promising.

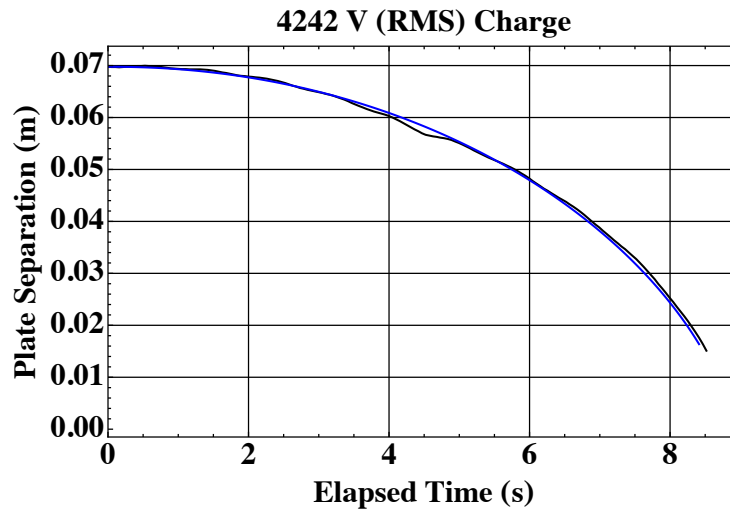
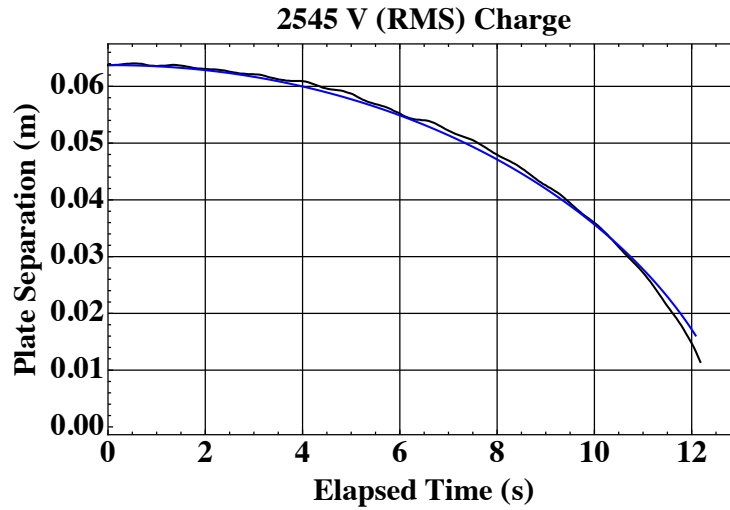


Figure 24. Position vs time data for two electrostatic attraction tests showing predicted data (blue) and actual data (black). The upper plot is for a 10 Hz 2545 V RMS sinusoidal drive signal and the lower plot is for a 10 Hz 4242 V RMS sinusoidal drive signal.

4.3 Plasma Shielding

The ISS sits in an orbit (408 km) that contains a low density plasma. The peak measured value for the plasma's electron density at altitudes between 240-450 km is $1.6 \times 10^{11} \text{ m}^{-3}$ [15]. The free charges in plasma can have two types of shielding that can adversely affect the proposed electromagnetic propulsion methods discussed above. The first is a response to the changing magnetic field used for repulsion and transverse motion. Since the plasma is conductive, eddy currents will form in response to the changing magnetic field and work to cancel the field passing through it. This is similar to the skin depth in conductors and follows similar mathematics, but is referred to as the plasma length.

The second is a response to the polarized electrodes used for generating attractive force. The charges in the plasma will rearrange themselves to cancel the electric field generated by the electrodes. This is similar to the double layer effect seen when electrodes are placed in ionic solutions. In plasmas, an electrostatic field will fall off exponentially in what is referred to as the Debye length. At the altitude of the ISS, this is approximately 4.5-8.3 mm depending on the electron temperature variations [16]. If the potential across the electrodes is varied in time, there is a frequency dependent inertial response by the charges. As the frequency of the changing potential is increased, the charge motion can no longer keep up with the varying field and the electric field is no longer cancelled by the plasma. The frequency this occurs at is dependent on the electron density and referred to as the plasma frequency [11]:

$$f_p = \frac{1}{2\pi} \left(\frac{Ne^2}{\epsilon_0 m_e} \right)^{1/2} = 8.98\sqrt{N}, \quad (180)$$

where N is the electron density, e is the charge of an electron, ϵ_0 is the permittivity of free space, and m_e is the mass of an electron. Assuming a worst case $N = 1.6 \times 10^{11}$, then $f_p = 3.59 \text{ MHz}$. The plasma length is

$$\delta = 1/\text{Im}(k), \quad (181)$$

where k is the wavenumber given by

$$k = \sqrt{\left(\frac{2\pi f}{c} \right)^2 \left(1 - \frac{f_p^2}{f^2} \right)}, \quad (182)$$

where c is the speed of light in vacuum and f is the frequency of the electromagnetic wave propagating through the plasma. When $f < f_p$, the fields will attenuate exponentially. At the low frequencies used to drive our magnetic fields, the plasma length is approximately $\delta = 13.3 \text{ m}$. When $f > f_p$, no attenuation occurs. Since our ECAPS will be operated at only short distances from the ISS, we are free to choose frequencies that allow us to drive our coils most efficiently. However, our capacitance based force will be blocked at frequencies below the plasma frequency. We could run at frequencies above the plasma frequency, but there is a resonance of the plasma electrons that occurs at f_p . This resonance can potentially be used to allow us to drive the capacitive plates at a much lower voltage due to a gain effect that occurs.

To understand how this works, we need to look at the response of plasma between two electrodes derived in a draft textbook by J. D. Callen [17]. The applied field is given by $\vec{E}_{ext} \equiv \vec{E}_0 \sin \omega_0 t$, where \vec{E}_0 is the electric field amplitude and ω_0 is the angular frequency. The inertial response of the system is governed by the differential equation:

$$\frac{\partial^2 \vec{E}}{\partial t^2} + \omega_{pe}^2 \vec{E} = -\omega_{pe}^2 \vec{E}_{ext}. \quad (183)$$

The total response is given by Callen after summing together the homogeneous, particular, and externally applied electric field components ($\vec{E} = \vec{E}_h + \vec{E}_p + \vec{E}_{ext}$). The end result is given by

$$\vec{E}(t) = -\frac{\omega_0 \omega_{pe}}{\omega_0^2 - \omega_{pe}^2} \vec{E}_0 \sin \omega_{pe} t + \frac{\omega_0^2}{\omega_0^2 - \omega_{pe}^2} \vec{E}_0 \sin \omega_0 t, \quad (184)$$

where ω_{pe} is the angular plasma frequency. When $\omega_0 \ll \omega_{pe}$, the field is totally cancelled by the charges in the plasma, assuming the plasma charge density is sufficient to block all of the charges on the electrodes. As ω_0 approaches ω_{pe} , a resonance occurs that results in the field becoming many times larger than the external field. If we can operate our drive circuit near the plasma frequency, we may be able to take advantage of this and use it to amplify our field using much lower voltages on our electrodes. For $\omega_0 > \omega_{pe}$, the charges in the plasma can no longer rearrange themselves in time to block the field and the entire external field penetrates the plasma.

To get the force between the electrode and the ISS skin, we use the relationship $\vec{F} = q\vec{E}$. We have \vec{E} from equation 184, but need to find q , the total charge on the plate (or skin of the ISS). We can start with the following relationship for the surface charge, σ , on a conductive surface:

$$\sigma = -\epsilon_0 \frac{\partial \Phi}{\partial n} = \epsilon_0 E \hat{n}. \quad (185)$$

This states that the surface charge density is equal to the normal component of the electric field at the conductor's surface multiplied by the permittivity of free space. If we integrate over the surface of our electrode, we get the total charge,

$$q = \epsilon_0 EA. \quad (186)$$

So, the force is given by $\vec{F} = \epsilon_0 E^2 A \hat{n}$. We can then combine this with equation 184 to get

$$\vec{F} = \epsilon_0 A \left(-\frac{\omega_0 \omega_{pe}}{\omega_0^2 - \omega_{pe}^2} \vec{E}_0 \sin \omega_{pe} t + \frac{\omega_0^2}{\omega_0^2 - \omega_{pe}^2} \vec{E}_0 \sin \omega_0 t \right)^2 \cdot \hat{n}, \quad (187)$$

where $\vec{E}_0 = \frac{V}{d} \hat{n}$ for a parallel plate geometry.

An implicit assumption in the above discussion is that below the plasma frequency there is sufficient charge density in the ionosphere to cancel the charges on the plates used for electrostatic attraction. If we assume a 0.01 m² plate at a distance of 0.1 m, charged to ± 6000 V and use Equations 185 and 186, we get a total charge of 5.31×10^{-9} Coulombs. The total charge in a cubic decimeter of space

nearby is $(.001m^3)Nq = 2.56 \times 10^{-11}$ Coulombs. So there is around 207 times more charge on the electrode than in a cubic decimeter of nearby space between the plate and the ISS surface. This suggests that only a low frequency oscillation may be necessary to minimize the shielding effect from the plasma.

4.4 Plasma Test

4.4.1 Test Description

A test was conducted in the Low Earth Orbit ionosphere simulation chamber at Marshall Space Flight Center (MSFC) to see if a low frequency oscillation mentioned above will overcome the shielding effect from the plasma. The test chamber is designed to provide varying densities of the type of plasma experienced in Earth's atmosphere while in low Earth orbit, simulating the conditions experienced by the ISS. It was hypothesized that putting a large amount of charge on the plates of an inspection spacecraft and oscillating the voltage at audio frequencies is sufficient to keep the plasma in the ionosphere from cancelling out the force.

The test uses a hanging conductive sphere next to a ground plane since the capacitance and force for this geometry are already well known [18]. The Debye length is under half a centimeter, so the separation between the sphere and ground plane must exceed this distance. Therefore, testing was conducted with 1 cm between the sphere edge and the ground plane. Two methods of excitation are used to generate 2-12 kV_{pp} between the sphere and the ground plane. One method, using a DC-DC converter tests frequencies from 10-150 Hz and the other uses a step-up transformer operating at 5-20 kHz. The position was recorded with a laser displacement sensor mounted outside the chamber and aiming at the sphere through a window. Tests were run in vacuum with the voltage on and off and repeated again with the ion source on to see to what extent the displacement is reduced.

4.4.2 Equipment List

1. Micro-Epsilon optoNCDT 1420-500 Displacement Sensor (500 mm)
2. Micro-Epsilon IFP2001/USB RS-422 to USB interface
3. Fluke 189 True RMS Digital Multimeter with Optical USB interface
4. Cal Test Electronics CT4079-NA High Voltage Probe Kit for multimeter and oscilloscope
5. Rigol DG4162 Function Generator with USB cable
6. Crown CDi4000 Audio Power Amplifier
7. GW Instek GPS-3303 DC Power Supply
8. Step up transformers (hyperlink 1 and hyperlink 2)
9. HVM Technology HVA0560, 0 to +/- 6000 V DC/DC Converter (will run AC up to 150 Hz)

10. Terminal strip for landing high voltage wires
11. Painted hollow aluminum sphere, 2-inch diameter with threaded solder fitting for high voltage cable
12. 8"×9" aluminum plate, with insulated coating on one side
13. HP Laptop with Windows 7 and a USB hub

4.4.3 Test Configuration with Transformer

The block diagram below in Figure 25 shows the configuration of the test equipment using one of the transformers to provide voltage to the sphere. The Rigol function generator is configured with a 3 Vpp sine wave with no offset voltage. This will provide a standard line voltage input to the channel one input of the power amplifier. The output of the power amplifier is configured and wired in bridge mode to gang together the channel 1 and 2 outputs. The amplifier output is then run to the primary side of the transformer. The secondary is the high voltage side of the transformer and it is connected to the terminal block to feed the sphere. The metal sphere is painted and suspended so that the center of the sphere lines up with the window in the test chamber.

The ILD1420 has a range of 500 mm (19.7"). The sphere and displacement sensor must be located so that the distance between them is less than this amount. Some photos of the setup used at Kennedy Space Center appear in Figure 26.

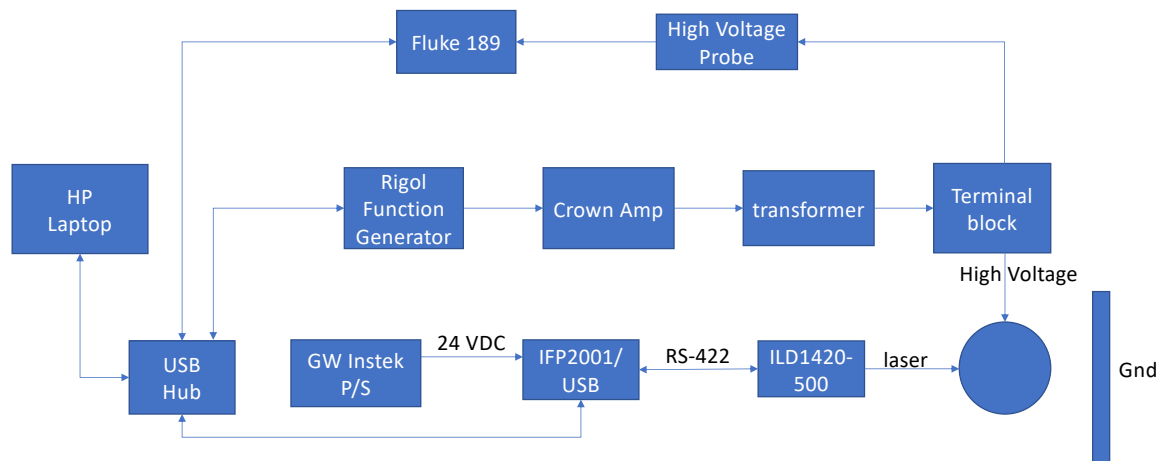


Figure 25. Block diagram showing test configuration using a step-up transformer to generate the high voltages between the sphere and the ground plane.

4.4.4 Test Configuration with High-Voltage DC-DC Converter

This test configuration uses an HVM Technology HVA Series (HVA0560) to generate up to +/- 6 kV from DC to a few hundred Hertz. The HVA0560 requires a 5 VDC

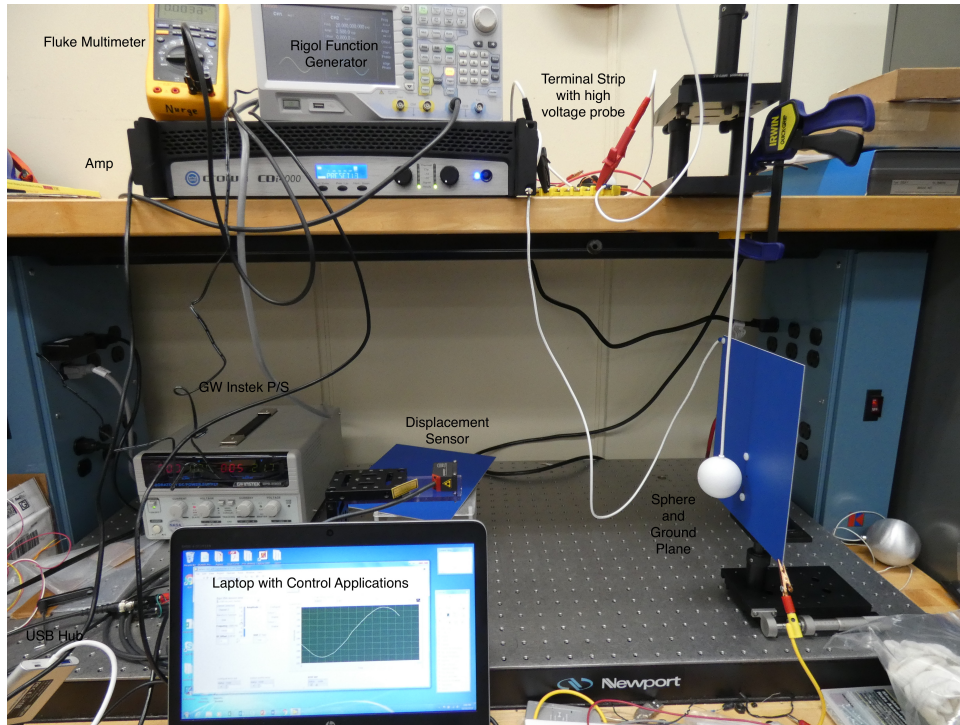


Figure 26. Photos showing test configuration using a step-up transformer to generate the high voltages between the sphere and the ground plane.

supply voltage and a 5 Vpp (with 2.5 VDC offset) control voltage. By using a 10-150 Hz sine wave, the output can be varied sinusoidally up to +/-6 kV. The data sheet is available at this link: HVA0560. The test configuration block diagram appears below in Figure 27.

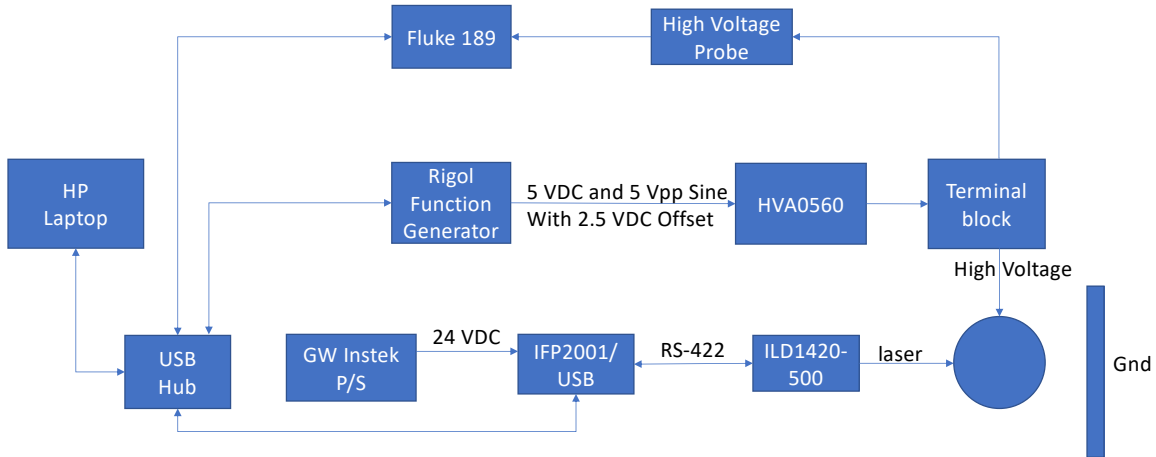


Figure 27. Block diagram showing test configuration using a HVM Technology DC-DC converter to generate the high voltages between the sphere and the ground plane.

4.4.5 Test Plan

The Rigol function generator is to be configured to provide a 5, 4, 3, 2, 1, and 0 Vpp control signal (with 2.5 VDC offset) to the HVA0560 at frequencies of 10, 20, 50, 100, and 150 Hz. This should result in a set of data similar to the one found from the bench test at KSC. The data from this test is given below in Figure 28 along with the predicted displacement based on a 60 g, 1-inch radius sphere, suspended by a 23-inch long high voltage wire, with a starting location 1 cm from a ground plane. The MSFC test is done in the vacuum of the test chamber at least once with the ion source on and once with it off. If the results between the two vary, indicating a reduction in displacement due to the presence of the ions, other initial displacements should be tried. The theoretical displacement curve which shows fairly close agreement with the test data shown in Figure 28.

The transformer can be used to get slightly higher voltages than the DC-DC converter but it is optimized to operate at close to 20 kHz. Other frequencies are possible, but damage occurred during the KSC test when working at 5 kHz. The results for 20 kHz from the bench test at KSC are shown below in Figure 29. At 5 kV_{rms}, the displacement is higher than predicted. The sphere oscillates when it is displaced and 20+ cycles must be averaged to get a representation of the steady state value. Due to non-linearities, the force is much higher at its closest approach to the ground plane than its furthest separation. It's possible the measured displacement

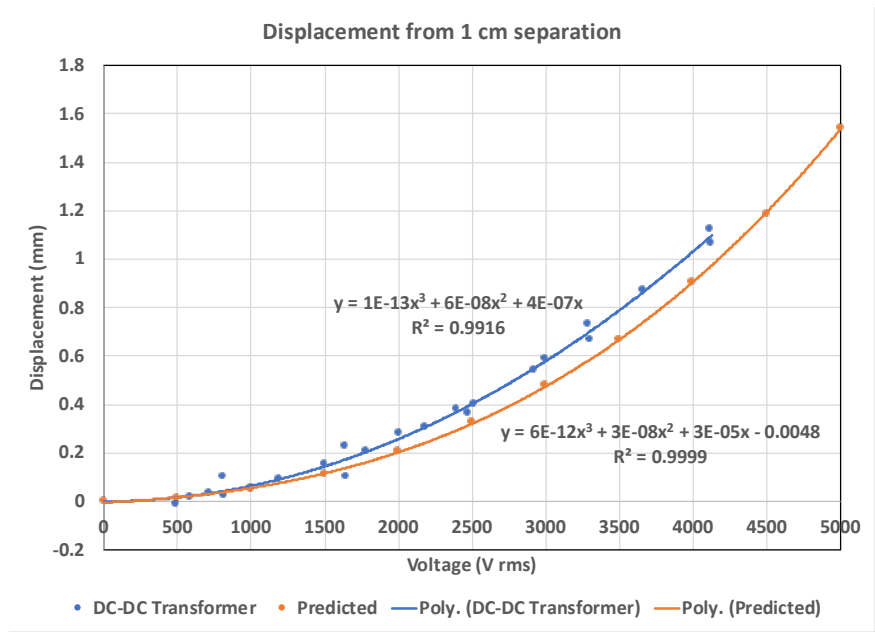


Figure 28. Graph showing the displacement as a function of voltage of the sphere starting at 1 cm separation from the ground plane compared to the predicted displacement. Data was generated using the HVA0560 DC-DC converter operating at frequencies between 10-150 Hz in normal atmosphere.

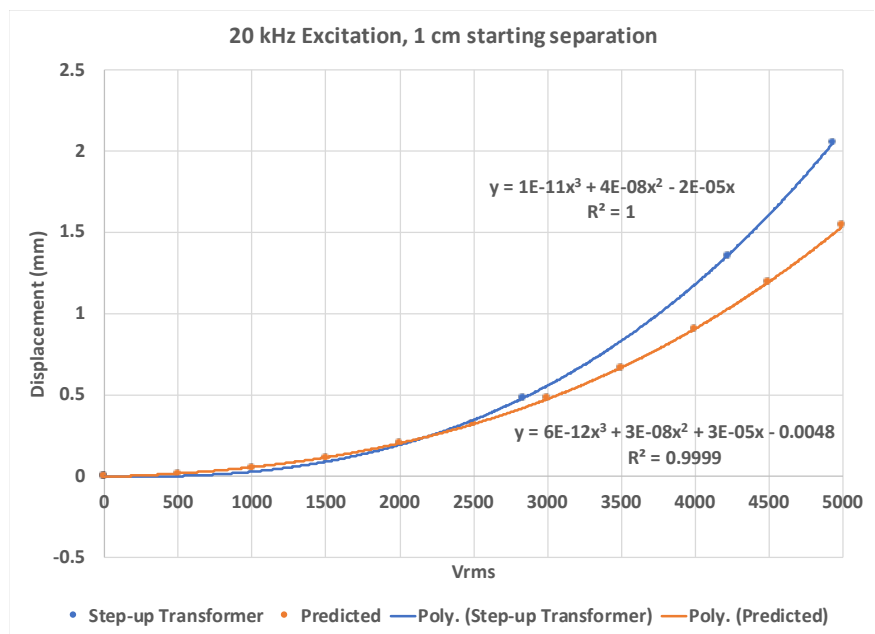


Figure 29. Graph showing the displacement as a function of voltage of the sphere starting at 1 cm separation from the ground plane using the step-up transformer at 20 kHz

may be biased higher since the oscillations bring it much closer to the ground plane than the calculated steady state value.

Using the transformer, the plan is to test at 1, 2, 3, 4, 5, and 6 kV_{rms} and at 10, 15, and 20 kHz. The goal is to fill in as much of the curve as possible similar to the plot for the HVA0560.

4.4.6 Test Results

The testing was conducted in November 18-21, 2019 in building 4605 at MSFC. The test configuration in and around the plasma chamber is shown in the series of photographs in Figure 30. The sphere was suspended from a wire hung from an “L” shaped frame constructed in the vacuum chamber (lower left photo). The distance between the pivot point and the sphere center was 17” rather than the 24” used in earlier testing at KSC. The ground plane was the same coated aluminum plate used in the testing at KSC and was mounted on a translation stage so the distance to the sphere could be varied. The high voltage wiring was routed along the “L” and then through a vacuum feed through on the side of the chamber. The wire then ran to the terminal strip on top of the amplifier (upper right photo). The displacement sensor was mounted outside the chamber and was able to monitor the position of the sphere through a window in the side of the chamber (lower right photo). Unfortunately, the overall capacitance of the feed-through and the cable path (about 115 pF) exceeded the drive capability of the HVA DC/DC converter. So, testing was only possible with the combination of the amplifier and step-up transformer.

The first test conducted was to charge the sphere up in ambient conditions to see that all of the equipment was operational. There were quite a few places where the high voltage cable came close to a ground point and caused corona discharges to occur. The high voltage cable was either separated further from the ground or better insulated through the addition of layers of Kapton tape. The first data was collected by ramping the voltage up and down with the sphere in the chamber after it was pumped down to a vacuum. The initial excitation was a 10 kHz sinusoidal signal that seemed to follow the predicted curve as voltage was increased and decreased. The comparison between the two plots appears in Figure 31. These two show close agreement but the falling voltage case as well as the curves for 10 kHz and 15 kHz have a fair amount of spread. The plot showing the composite of the collected data is shown in Figure 32. The high voltage cable had a rather thick insulator on it that had to be vacuum compatible. It is thought that the stiffness of this insulation played a role in the hysteresis seen in the data as the sphere rarely followed the same path or returned to the starting location.

When the plasma was turned on for the first time we had an inadvertent discharge that resulted in damage to the displacement sensor interface, the adjustable DC power supply, and our high voltage scope probe. Fortunately, the MSFC folks were able to obtain suitable replacements within a day to get us back up and testing. The Debye length during these early runs was around 4.4 mm. The sphere was painted with a high temperature paint that was supposed to be safe to use in vacuum. Unfortunately, the paint didn’t provide enough insulation to the sphere and the purple glow of the corona discharge was clearly visible around the sphere.

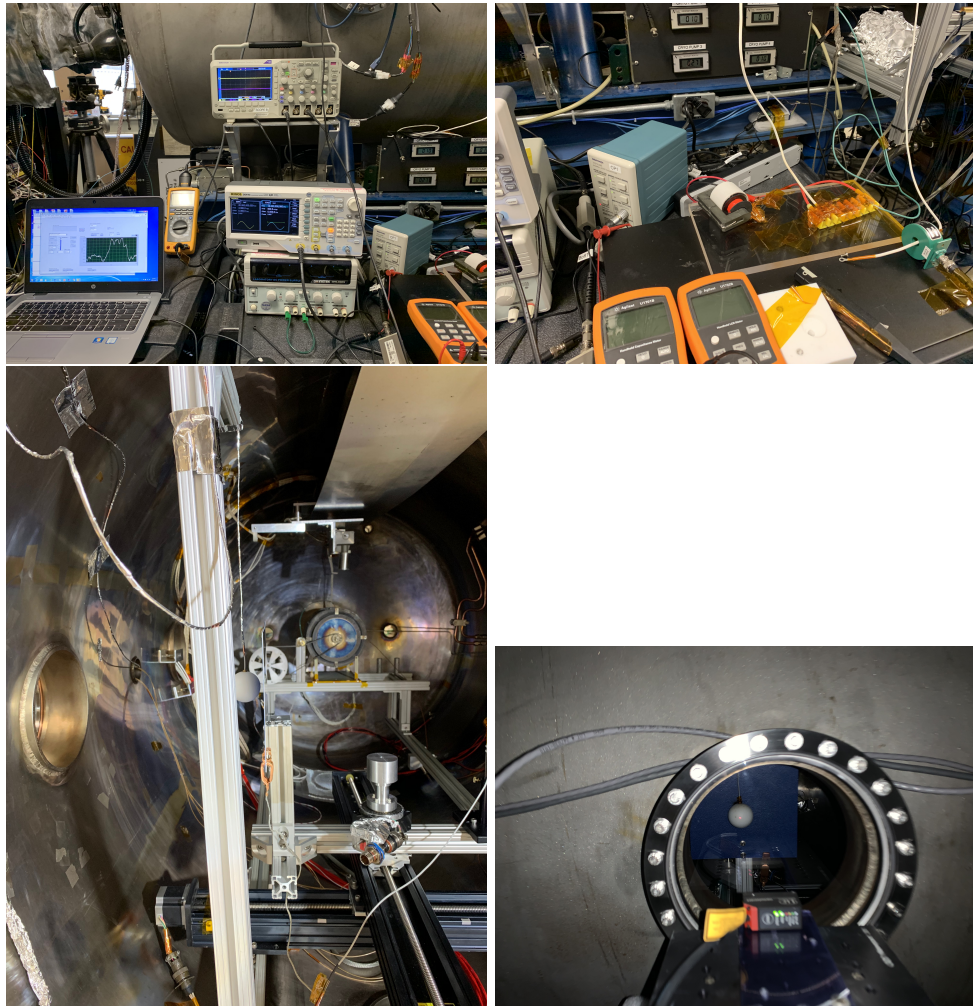


Figure 30. Photos showing the test configuration at MSFC.

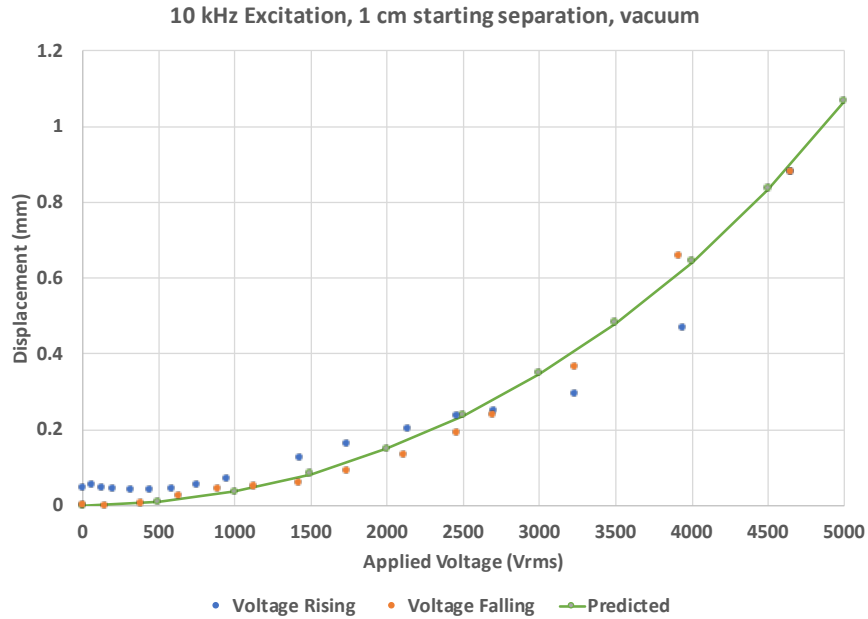


Figure 31. Plot showing displacement of a sphere starting 1 cm from a ground plane as the voltage on the sphere is increased with a 10 kHz drive frequency in vacuum. The curve for the predicted motion is shown for comparison.

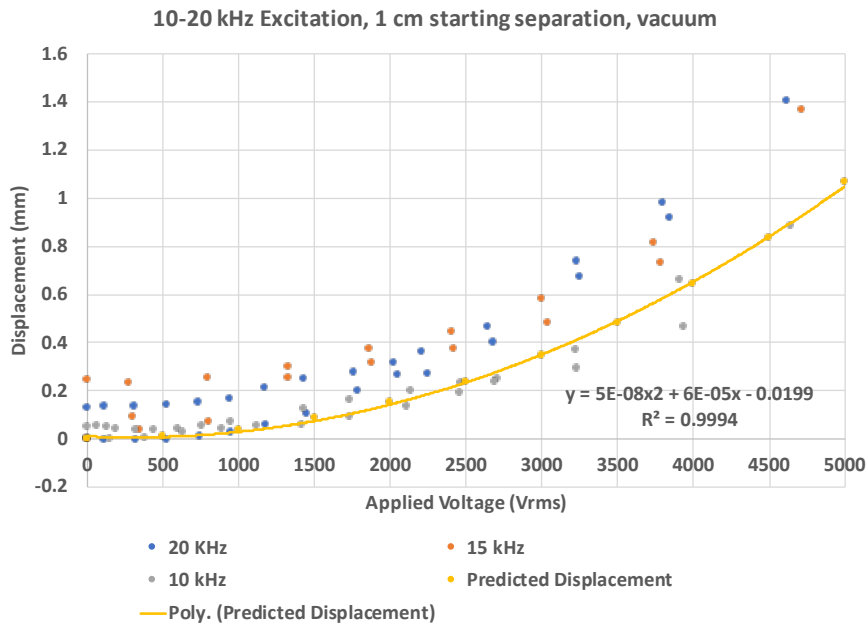


Figure 32. Plot of points showing displacement of a sphere starting 1 cm from a ground plane as the voltage on the sphere is increased. The points shown are from runs at three different frequencies, 10, 15, and 20 kHz. The curve for the predicted motion is shown for comparison

The left photo in Figure 33 shows the presence of the corona around the sphere and discharges can be seen as bright spots on the sphere. The discharges cause discoloration of the sphere as can be seen in the right hand photo. The discharges



Figure 33. The photo on the left shows the charged sphere in the presence of the plasma. The glow of a corona discharge is present. The bright spots on the sphere are believed to be electrons punching through the paint to try and neutralize the charge. The photo on the right shows the discoloration to the sphere from the hot spots in the paint that occur from the plasma electrons attempting to neutralize the potential.

likely caused the variations we experienced in the movement and the stability of the applied voltage. The results of a 10 kHz and 20 kHz run are shown in Figure 34. The overall motion exceeded the predictions but the mechanism for this is not understood at this time.

On the final day the plasma was measured to have a Debye length of around 4 mm. Numerous discharges occurred and the sphere turned black. The results are similar to the earlier test with hysteresis and strong variation in the distribution of the points that show the displacement of the sphere as a function of the RMS voltage. The MSFC lab had a high voltage AC supply that we used to achieve a 1 kHz oscillation frequency. The results from this final day of testing appear in Figure 35

4.4.7 Discussion of Results

We predicted the motion of 2-inch diameter sphere located 1 cm from a ground plane when the sphere is raised to some potential above the ground plane. When an oscillating voltage between 0 and 5000 Vrms is applied to this sphere, it will move approximately 1.1 and 1.5 mm for 43.2 cm and 61 cm suspension lengths and a mass of 60 g for the sphere. We selected to operate this test configuration in a plasma similar to that encountered at 400 km above the earth as experienced by the ISS. Post-test measurements were made of the plasma configuration and determined

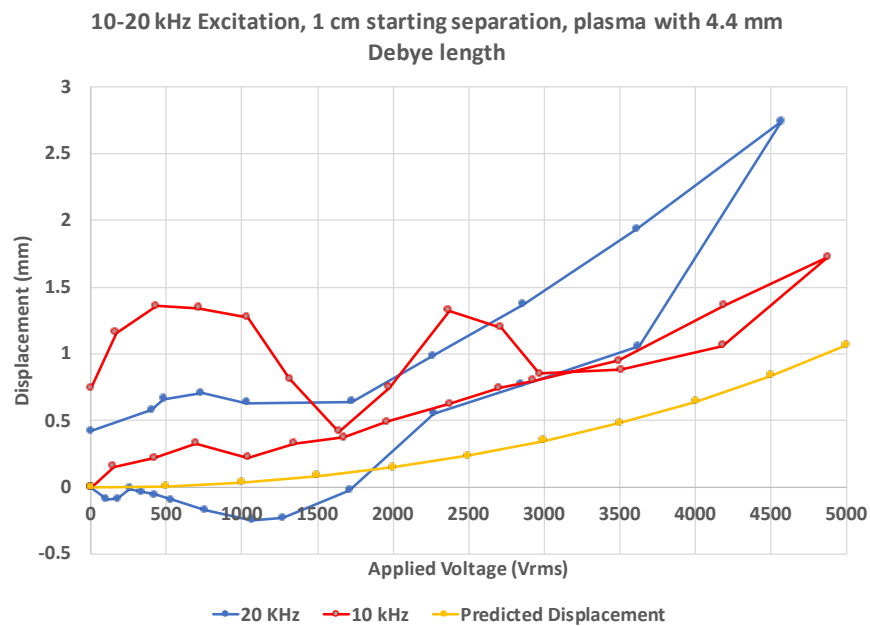


Figure 34. Plot of points showing displacement of a sphere starting 1 cm from a ground plane as the voltage on the sphere is increased in the presence of plasma with a Debye length of 4.4 mm. The points shown are from runs at two different frequencies, 10 and 20 kHz. The curve for the predicted motion is shown for comparison

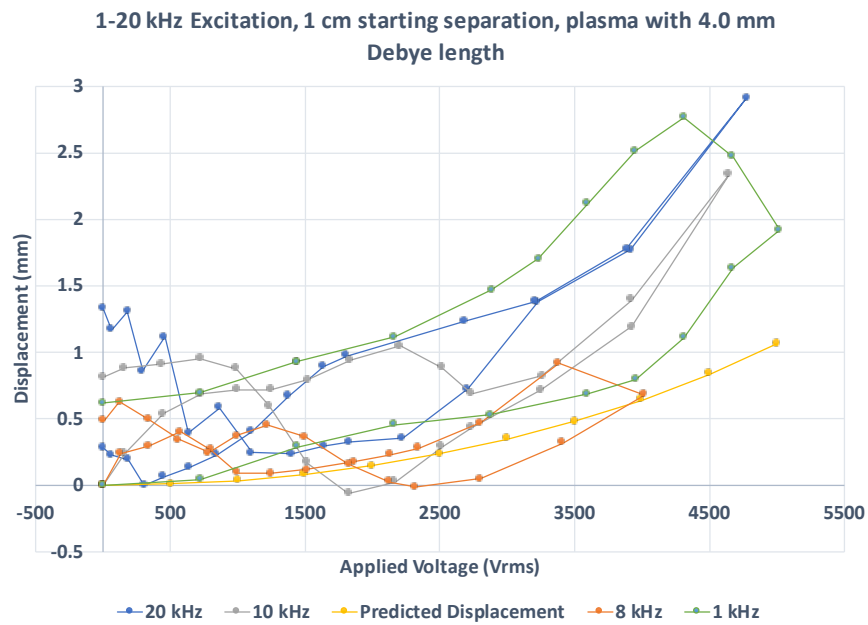


Figure 35. Plot of points showing displacement of a sphere starting 1 cm from a ground plane as the voltage on the sphere is increased in the presence of plasma with a Debye length of 4.0 mm. The points shown are from runs at various frequencies between 1-20 kHz. The curve for the predicted motion is shown for comparison

that the final tests were run at a plasma density of $0.8-1.0 \times 10^{12}$ electrons/m³ and electron temperatures of 0.2 eV for the cold electrons (90% of the population) and 2.0 eV for the hot electrons (10% of the population). Overall, this results in a Debye length of 4 mm. The results of the test show that there is at least 1.1 mm of displacement of the sphere with 5000 Vrms applied, even with the plasma turned on, regardless of the frequency. There is no evidence of any screening occurring to diminish the force of attraction between the sphere and the ground plane. This is likely due to the much larger quantity of charge placed on the sphere than is available in the chamber to screen the sphere from the ground plane.

Given the large variations in the data sets, a small screening effect would be hard to discern, especially at lower applied voltages where less charge is placed on the sphere. Additionally, concerns were raised that the plasma density at the sphere may not have been exactly what was read by the Langmuir probe in the chamber as the plasma generator, probe, and test setup were not well aligned with each other. The insulation on the cable suspending the sphere was stiff and is believed to be the source of the hysteresis in the plots and different starting and ending positions when the sphere was returned to 0 Volts. Another anomaly is that the peak displacement at the highest voltages on the sphere occurred with the plasma present. These were two to three times the predicted displacement. A possible explanation for this is formation of sheath near each electrode surface. The sheath formation causes the plasma between the sheaths to achieve a potential that exceeds the peak voltage applied to the electrodes. There is then a large drop in potential between the electrode and the edge of the plasma that is the width of the sheath. This causes a higher electric field to occur and an enhancement in the force felt by the electrode.

A repeat of the test was planned with improved insulation on the sphere, a more flexible wire, and improved alignment, but the impact of the shutdown of MSFC due to the Covid-19 virus precluded that from occurring prior to the project completion.

5 Conclusions

Several magnetic force actuators and an electrostatic force actuator have been discussed that provide attractive, repulsive, and translational motion with respect to conductive surfaces. Analytical solutions have been obtained that were then confirmed via models in Mathematica and independently in COMSOL. In some cases, experimental data was collected to confirm the force behavior. When combined, full six degree of motion is possible via these actuators. The feedback and control methods have not been discussed but will be documented in future publications by our co-author, Katherine Wilson. It is hoped that the analytic models will help to simplify the understanding of the actuator behavior and to serve as a basis for checking the results from more elaborate models built with software such as COMSOL.

A fascinating aspect of this work that we would have liked to explore further is the behavior of the magnetic actuator when opposite a conducting plate that was backed by a thin layer of ferrous metal. Because steel has a high capacity for magnetic flux, only a thin layer is required behind the conductor to obtain repulsive, neutral, or attractive forces just by shifting the drive frequency for the coil. The theory shows that the attractive force is approximately an order of magnitude larger than the electrostatic method at the same working distance. This simplifies the design as only coils would be needed. Such a system would also provide better balance between the attractive, repulsive, and lateral forces making the feedback and control system a bit easier to develop. This also enables applications like landing on a small iron core asteroid. DC currents in the drive coil would allow spacecraft to stick to the asteroid. If an aluminum plate was carried under the coil it could be dropped before take off and then used to push against with an AC coil current to generate repulsive force. Unfortunately due to the pandemic, we were unable to verify our mathematics and analysis experimentally.

Lastly, the electrostatic actuator testing had some ambiguous results that we planned to try and resolve through another round of testing but again were interrupted by the pandemic. It would be interesting to better understand the sheath formation and to determine if it can be exploited to provide an enhanced attractive force.

References

1. Hammond, P., 1962, "The calculation of the magnetic field of rotating machines. part 3: Eddy currents induced in a solid slab by a circular current loop," *Proceedings of the IEE-Part C: Monographs*, **109**(16), pp. 508–515.
2. Zaman, A. J. M., Long, S. A., and Gardner, C. G., 1980, "The impedance of a single-turn coil near a conducting half space," *Journal of Nondestructive Evaluation*, **1**(3), pp. 183–189.
3. Dodd, C. V., 1967, "Solutions to electromagnetic induction problems," Technical Memorandum ORNL-TM-1842, Oak Ridge National Laboratory.
4. Trötzsch, U., Wendler, F., and Kanoun, O., 2013, "Simplified analytical inductance model for a single turn eddy current sensor," *Sensors and Actuators A: Physical*, **191**, pp. 11–21.
5. Zhang, S., Wu Weihua, and Tang Jiangfeng, 2015, "Magnetic field calculation of cylindrical exciting coil above conductive plates," *2015 12th IEEE International Conference on Electronic Measurement Instruments (ICEMI)*, vol. 3, pp. 1471–1476.
6. Cheng, D. H. S., 1965, "The reflected impedance of a circular coil in the proximity of a semi-infinite medium," *IEEE Transactions on Instrumentation and Measurement*, **IM-14**(3), pp. 107–116.
7. Kausel, E. and Baig, M. M. I., 2012, "Laplace transform of products of Bessel functions: A visitation of earlier formulas," *Quarterly of Applied Mathematics*, **70**(1), pp. 77–97.
8. Jackson, J. D., 1998, *Classical Electrodynamics*, Wiley, 3rd ed.
9. Laithwaite, E. R., 1974, "The hyperconductor and the linomat," *Electrical Review*, **25**, pp. 530–532.
10. El-Markabi, M. H. S. and Freeman, E. M., 1982, "Electromagnetic properties of a circular cylindrical coil in a set of planar ferromagnetic regions," *IEE Proceedings*, **129**, **Part A**(8), pp. 582–589.
11. Lorrain, P., Corson, D. R., and Lorrain, F., 1988, *Electromagnetic Fields and Waves*, W. H. Freeman and Company, third ed.
12. Batygin, Y. V., Golovashchenkob, S. F., and Gnatova, A. V., 2013, "Pulsed electromagnetic attraction of sheet metals – fundamentals and perspective applications," *Journal of Materials Processing Technology*, **213**, pp. 444–452.
13. Batygin, Y. V., Golovashchenkob, S. F., and Gnatova, A. V., 2014, "Pulsed electromagnetic attraction of nonmagnetic sheet metals," *Journal of Materials Processing Technology*, **214**, pp. 390–401.

14. Astakhov, Y. S., Djaliashvili, O. A., Radzivanovich, V. D., Shneerson, G. A., and Fridman, B. E., 1992, "Application of alternating and pulsed magnetic fields for removal of intraocular foreign bodies of non-ferromagnetic metals," *IEEE Transactions on Magnetics*, **28**(1), pp. 659–662.
15. Jensen, M. D. and Baker, K. D., 1992, "Measuring ionospheric electron density using the plasma frequency probe," *Journal of Spacecraft and Rockets*, **29**(1), pp. 91–95.
16. Otsuka, Y., Kawamura, S., Balan, N., Fukao, S., and Bailey, G. J., 1998, "Plasma temperature variations in the ionosphere over the middle and upper atmosphere radar," *Journal of Geophysical Research*, **103**(A9), pp. 20705–20713.
17. Callen, J. D., 2003, "Fundamentals of plasma physics," Chapter 1, <http://homepages.cae.wisc.edu/callen/book.html>.
18. Crowley, J. M., 2008, "Simple expressions for force and capacitance for a conductive sphere near a conductive wall," *Proceedings of the ESA Annual Meeting on Electrostatics 2008*, pp. 1–14.

6 Appendix A - COMSOL Model for a Linear Induction Motor Interacting with and Aluminum Slab and an Aluminum Slab on top of an Iron Slab - Longitudinal Force

1 Global Definitions

GLOBAL SETTINGS

Version	COMSOL Multiphysics 5.5 (Build: 359)
Unit system	SI

USED PRODUCTS

COMSOL Multiphysics
AC/DC Module

1.1 PARAMETERS

PARAMETERS 1

Name	Expression	Value	Description
wbound	$nw \cdot \max(d, ro)$	6.75E-2 m	width of bounding box
sigmaCond2	$\text{if}(\text{mur}2 > 1, 1e7[\text{S/m}], 3.5e7[\text{S/m}])$	1E7 S/m	conductivity of conductor 2
sigmaCond1	3.5e7[S/m]	3.5E7 S/m	conductivity of conductor 1 (nearer to coil)
ro	0.015[m]	1.5E-2 m	outer radius of coil
p3	$\text{if}(\text{dir}l0 > 0, 360/4*3, 0)$	2.7E2	phase of coil 3
p2	$\text{if}(\text{dir}l0 > 0, 360/4*2, 360/4*1)$	1.8E2	phase of coil 2
p1	$\text{if}(\text{dir}l0 > 0, 360/4*1, 360/4*2)$	9E1	phase of coil 1
p0	$\text{if}(\text{dir}l0 > 0, 0, 360/4*3)$	0E0	phase of coil 0
nw	4.5	4.5E0	definition for width of bounding box
nTurns	25	2.5E1	number of turns
nh	4.5	4.5E0	definition for height of bounding box
ncond2	$n\text{cond} * 2$	1E-3 m	definition for maximum size of conductor mesh
ncond	0.5e-3[m]	5E-4 m	definition for maximum size of conductor mesh
mur2	1000	1E3	relative permeability of conductor 2
mur1	1	1E0	relative permeability of conductor 1
lbound	$(nw + 3) \cdot \max(d, ro)$	1.125E-1 m	length of bounding box
l0	$5[\text{A}] \cdot n\text{Turns}$	1.25E2 A	current in coil
hcond2	hcond1	1.5E-3 m	thickness of conductor 2
hcond1	1.5[mm]	1.5E-3 m	thickness of conductor 1

Name	Expression	Value	Description
hbound	$nh \cdot \max(d, ro) + \text{gap}$	7.25E-2 m	height of bounding box
gap	0.5[cm]	5E-3 m	gap between coils
dirI0	1	1E0	direction of current
d	0.25[cm]	2.5E-3 m	distance of liftoff

2 Component 1

SETTINGS

Description	Value
Unit system	Same as global system
Avoid inverted elements by curving interior domain elements	Off

SPATIAL FRAME COORDINATES

First	Second	Third
x	y	z

MATERIAL FRAME COORDINATES

First	Second	Third
X	Y	Z

GEOMETRY FRAME COORDINATES

First	Second	Third
Xg	Yg	Zg

MESH FRAME COORDINATES

First	Second	Third
Xm	Ym	Zm

2.1 GEOMETRY 1

UNITS

Length unit	mm
Angular unit	deg

2.1.1 Plate 1 (blk1)

POSITION

Description	Value
Position	{-wbound/2, -lbound/2, -hcond1}

AXIS

Description	Value
Axis type	z - axis

SIZE AND SHAPE

Description	Value
Width	wbound

Description	Value
Depth	lbound
Height	hcond1

2.1.2 Plate2 (blk4)

POSITION

Description	Value
Position	$\{-wbound/2, -lbound/2, -hcond1 - hcond2\}$

AXIS

Description	Value
Axis type	z - axis

SIZE AND SHAPE

Description	Value
Width	wbound
Depth	lbound
Height	hcond2

2.1.3 Outer Air Domain (blk3)

POSITION

Description	Value
Position	$\{-wbound/2, -lbound/2, -hbound/2 + (d + hcond1 + hcond2)/2 + gap/2\}$

AXIS

Description	Value
Axis type	z - axis

SIZE AND SHAPE

Description	Value
Width	wbound
Depth	lbound
Height	hbound

2.1.4 Work Plane 1 (wp1)

PLANE DEFINITION

Description	Value
Plane	xz - plane

UNITE OBJECTS

Description	Value
Unite objects	On

Plane Geometry (sequence2D)

Point 1 (pt1)

POINT

Description	Value
Point coordinate	{15, 2.5}

2.1.5 Revolve 1 (rev1)

SETTINGS

Description	Value
Work plane	Work Plane 1

REVOLUTION ANGLES

Description	Value
Angles	{0, 2*pi}
Type of specification	Full revolution

REVOLUTION AXIS

Description	Value
Point on the revolution axis	{0, 0}
Direction of revolution axis	{0, 1}
Revolution axis	{{0, 0}, {0, 1}}

2.1.6 Coil 0 (copy1)

SETTINGS

Description	Value
x	0E0
y	-2.25E1
z	0E0

2.1.7 Coil 1 (copy2)

SETTINGS

Description	Value
Keep input objects	On
x	0E0

Description	Value
y	1.5E1
z	5E0

2.1.8 Coil 2 (copy3)

SETTINGS

Description	Value
Keep input objects	On
x	0E0
y	1.5E1
z	-5E0

2.1.9 Coil 3 (copy4)

SETTINGS

Description	Value
Keep input objects	On
x	0E0
y	1.5E1
z	5E0

2.2 MATERIALS

2.2.1 Vacuum

SELECTION

Geometric entity level	Domain
Selection	Geometry geom1: Dimension 3: All domains

MATERIAL PARAMETERS

Name	Value	Unit
Relative permeability	1	1
Electrical conductivity	0.1	S/m
Relative permittivity	1	1

BASIC SETTINGS

Description	Value
Relative permeability	{{1, 0, 0}, {0, 1, 0}, {0, 0, 1}}
Electrical conductivity	{{0.1, 0, 0}, {0, 0.1, 0}, {0, 0, 0.1}}
Relative permittivity	{{1, 0, 0}, {0, 1, 0}, {0, 0, 1}}

2.2.2 Conducting plate 1

SELECTION

Geometric entity level	Domain
Selection	Geometry geom1: Dimension 3: Domain 3

MATERIAL PARAMETERS

Name	Value	Unit
Electrical conductivity	sigmaCond1	S/m
Relative permittivity	1	1
Relative permeability	mur1	1

BASIC SETTINGS

Description	Value
Electrical conductivity	{{sigmaCond1, 0, 0}, {0, sigmaCond1, 0}, {0, 0, sigmaCond1}}
Relative permittivity	{{1, 0, 0}, {0, 1, 0}, {0, 0, 1}}
Relative permeability	{{mur1, 0, 0}, {0, mur1, 0}, {0, 0, mur1}}
electricconductivity_symmetry	0E0
relpermeability_symmetry	0E0

2.2.3 Conducting plate 2

SELECTION

Geometric entity level	Domain
Selection	Geometry geom1: Dimension 3: Domain 2

MATERIAL PARAMETERS

Name	Value	Unit
Electrical conductivity	sigmaCond2	S/m
Relative permittivity	1	1
Relative permeability	mur2	1

BASIC SETTINGS

Description	Value
Electrical conductivity	{{sigmaCond2, 0, 0}, {0, sigmaCond2, 0}, {0, 0, sigmaCond2}}
electricconductivity_symmetry	0E0
Relative permittivity	{{1, 0, 0}, {0, 1, 0}, {0, 0, 1}}
relpermittivity_symmetry	3E0
Relative permeability	{{mur2, 0, 0}, {0, mur2, 0}, {0, 0, mur2}}
relpermeability_symmetry	0E0

2.3 MAGNETIC FIELDS

USED PRODUCTS

COMSOL Multiphysics
AC/DC Module

SELECTION

Geometric entity level	Domain
Selection	Geometry geom1: Dimension 3: All domains

2.3.1 Ampère's Law 1

SELECTION

Geometric entity level	Domain
Selection	Geometry geom1: Dimension 3: All domains

Constitutive relation B-H

SETTINGS

Description	Value
Magnetization model	Relative permeability
Relative permeability	From material

Constitutive relation Jc-E

SETTINGS

Description	Value
Conduction model	Electrical conductivity
Electrical conductivity	From material

Constitutive relation D-E

SETTINGS

Description	Value
Relative permittivity	From material

Coordinate system selection

SETTINGS

Description	Value
Coordinate system	Global coordinate system

PROPERTIES FROM MATERIAL

Property	Material	Property group
----------	----------	----------------

Property	Material	Property group
Relative permeability	Vacuum	Basic
Electrical conductivity	Vacuum	Basic
Relative permittivity	Vacuum	Basic
Relative permeability	Conducting plate 1	Basic
Electrical conductivity	Conducting plate 1	Basic
Relative permittivity	Conducting plate 1	Basic
Relative permeability	Conducting plate 2	Basic
Electrical conductivity	Conducting plate 2	Basic
Relative permittivity	Conducting plate 2	Basic

2.3.2 Magnetic Insulation 1

SELECTION

Geometric entity level	Boundary
Selection	Geometry geom1: Dimension 2: All boundaries

2.3.3 Initial Values 1

SELECTION

Geometric entity level	Domain
Selection	Geometry geom1: Dimension 3: All domains

Coordinate system selection

SETTINGS

Description	Value
Coordinate system	Global coordinate system

2.3.4 Edge Current 1

SELECTION

Geometric entity level	Edge
Selection	Geometry geom1: Dimension 1: Edges 24–25, 32, 34

SETTINGS

Description	Value
I_0	$-I_0 \cdot \exp(i \cdot \pi \cdot p_0 / 180)$

Coordinate system selection

SETTINGS

Description	Value
Coordinate system	Global coordinate system

2.3.5 Edge Current 2

SELECTION

Geometric entity level	Edge
Selection	Geometry geom1: Dimension 1: Edges 26–27, 33, 36

SETTINGS

Description	Value
I_0	$-I_0 \cdot \exp(i \cdot \pi \cdot p_1 / 180)$

Coordinate system selection

SETTINGS

Description	Value
Coordinate system	Global coordinate system

2.3.6 Edge Current 3

SELECTION

Geometric entity level	Edge
Selection	Geometry geom1: Dimension 1: Edges 28–29, 35, 38

SETTINGS

Description	Value
I_0	$-I_0 \cdot \exp(i \cdot \pi \cdot p_2 / 180)$

Coordinate system selection

SETTINGS

Description	Value
Coordinate system	Global coordinate system

2.3.7 Edge Current 4

SELECTION

Geometric entity level	Edge
Selection	Geometry geom1: Dimension 1: Edges 30–31, 37, 39

SETTINGS

Description	Value
I_0	$-I_0 \cdot \exp(i \cdot \pi \cdot p_3 / 180)$

Coordinate system selection

SETTINGS

Description	Value
Coordinate system	Global coordinate system

2.3.8 Force Calculation 1

SELECTION

Geometric entity level	Domain
Selection	Geometry geom1: Dimension 3: Domains 2-3

Force calculation

SETTINGS

Description	Value
Force name	0E0
Torque axis, x component	0E0
Torque axis, y component	0E0
Torque axis, z component	1E0
Torque rotation point, x component	0E0
Torque rotation point, y component	0E0
Torque rotation point, z component	0E0

2.4 MESH 1

2.4.1 Size (size)

SETTINGS

Description	Value
Maximum element size	3.96E1
Minimum element size	7.13E0
Curvature factor	6E-1
Resolution of narrow regions	5E-1
Maximum element growth rate	1.5E0
Custom element size	Custom

2.4.2 Mapped 1 (map1)

SELECTION

Geometric entity level	Boundary
Selection	Geometry geom1: Dimension 2: Boundary 12

Distribution 1 (dis1)

SELECTION

Geometric entity level	Edge
Selection	Geometry geom1: Dimension 1: Edge 11

SETTINGS

Description	Value
Number of elements	floor(lbound/(ncond2))

Distribution 2 (dis2)

SELECTION

Geometric entity level	Edge
Selection	Geometry geom1: Dimension 1: Edge 22

SETTINGS

Description	Value
Number of elements	floor(wbound/(ncond2))

2.4.3 Swept 1 (swe1)

SELECTION

Geometric entity level	Domain
Selection	Geometry geom1: Dimension 3: Domains 2-3

SETTINGS

Description	Value
Face meshing method	Quadrilateral (legacy version 5.4)

Distribution 1 (dis1)

SELECTION

Geometric entity level	Domain
Selection	Geometry geom1: Dimension 3: Domains 2-3

SETTINGS

Description	Value
-------------	-------

Description	Value
Number of elements	floor(hcond1/ncond)

2.4.4 Edge 1 (edg1)

SELECTION

Geometric entity level	Edge
Selection	Geometry geom1: Dimension 1: Edges 24–39

Size 1 (size1)

SELECTION

Geometric entity level	Edge
Selection	Geometry geom1: Dimension 1: Edges 24–39

SETTINGS

Description	Value
Maximum element size	2.25E0
Minimum element size	2.25E-2
Curvature factor	2E-1
Maximum element growth rate	1.3E0
Predefined size	Extremely fine

2.4.5 Free Tetrahedral 2 (ftet2)

SELECTION

Geometric entity level	Domain
Selection	Remaining

Size 1 (size1)

SELECTION

Geometric entity level	Domain
Selection	Geometry geom1

SETTINGS

Description	Value
Maximum element size	1.13E1
Minimum element size	2.03E0
Curvature factor	6E-1
Resolution of narrow regions	5E-1
Maximum element growth rate	1.5E0

3 Mesh Sweep

3.1 PARAMETRIC SWEEP

Parameter name	Parameter value list
mur2	1, 1000

STUDY SETTINGS

Description	Value
Sweep type	Specified combinations
Parameter name	mur2
Unit	

PARAMETERS

Parameter name	Parameter value list	Parameter unit
mur2 (relative permeability of conductor 2)	1, 1000	

3.2 FREQUENCY DOMAIN

Frequencies (Hz)
1, range(100,100,5000)

STUDY SETTINGS

Description	Value
Include geometric nonlinearity	Off

SETTINGS

Description	Value
Frequencies	{1, 100, 200, 300, 400, 500, 600, 700, 800, 900, 1000, 1100, 1200, 1300, 1400, 1500, 1600, 1700, 1800, 1900, 2000, 2100, 2200, 2300, 2400, 2500, 2600, 2700, 2800, 2900, 3000, 3100, 3200, 3300, 3400, 3500, 3600, 3700, 3800, 3900, 4000, 4100, 4200, 4300, 4400, 4500, 4600, 4700, 4800, 4900, 5000}

PHYSICS AND VARIABLES SELECTION

Physics interface	Discretization
Magnetic Fields (mf)	physics

MESH SELECTION

Geometry	Mesh
Geometry 1 (geom1)	mesh1

4 Results

4.1 DERIVED VALUES

4.1.1 Global Evaluation 1

EXPRESSIONS

Expression	Unit	Description
-mf.Forceavx_0		x component of force on LIM
-mf.Forceavy_0		y component of force on LIM
-mf.Forceavz_0		z component of force on LIM

7 Appendix B - COMSOL Model for a Linear Induction Motor Interacting with and Aluminum Slab and an Aluminum Slab on top of an Iron Slab - Repulsive Force

1 Global Definitions

GLOBAL SETTINGS

Version	COMSOL Multiphysics 5.5 (Build: 359)
Unit system	SI

USED PRODUCTS

COMSOL Multiphysics
AC/DC Module

1.1 PARAMETERS

PARAMETERS 1

Name	Expression	Value	Description
d	1[cm]	1E-2 m	separation between coil and conductor
hBound	nh*max(d, rCoil)	5.44E-1 m	height of bounding box
hCond1	1.5[mm]	1.5E-3 m	height of conductor 1
hCond2	hCond1	1.5E-3 m	height of conductor 2
I0	1[A]*nTurns	3.2E2 A	amplitude of current in coil
mu0	4[H/m]*pi*10^(-7)	1.2566E-6 H/m	vacuum permeability
mur1	1	1E0	relative permeability of first conductor
mur2	1	1E0	relative permeability of second conductor
nCond1	9e-5[m]	9E-5 m	definition for mesh density in first conductor
nCond2	nCond1	9E-5 m	definition for mesh density in second conductor
nh	8	8E0	definition for bounding box height
nTurns	320	3.2E2	number of turns in coil
nw	7	7E0	definition for bounding box width
rCoil	136[mm]/2	6.8E-2 m	radius of coil
sigmaCond1	3.5e7[S/m]	3.5E7 S/m	conductivity of first conductor
sigmaCond2	if(mur2>1, 1e7[S/m], 3.5e7[S/m])	3.5E7 S/m	conductivity of second conductor
wBound	nw*max(d, rCoil)	4.76E-1 m	width of bounding box

2 Component 1

SETTINGS

Description	Value
Unit system	Same as global system
Avoid inverted elements by curving interior domain elements	Off

SPATIAL FRAME COORDINATES

First	Second	Third
r	phi	z

MATERIAL FRAME COORDINATES

First	Second	Third
R	PHI	Z

GEOMETRY FRAME COORDINATES

First	Second	Third
Rg	PHI _g	Zg

MESH FRAME COORDINATES

First	Second	Third
R _m	PHI _m	Z _m

2.1 GEOMETRY 1

2.1.1 Bounding (r1)

POSITION

Description	Value
Position	{0, -hBound/2 + (d + hCond1 + hCond2)/2}

SIZE

Description	Value
Width	wBound
Height	hBound

2.1.2 Conductor (r2)

POSITION

Description	Value
Position	{0, -hCond1}

SIZE

Description	Value
Width	wBound
Height	hCond1

2.1.3 Conductor 1 (r3)

POSITION

Description	Value
Position	{0, -hCond1 - hCond2}

SIZE

Description	Value
Width	wBound
Height	hCond2

2.1.4 Point 1 (pt1)

POINT

Description	Value
Point coordinate	{0.068, 0.01}

2.2 MATERIALS

2.2.1 Bound

SELECTION

Geometric entity level	Domain
Selection	Geometry geom1: Dimension 2: All domains

MATERIAL PARAMETERS

Name	Value	Unit
Relative permeability	1	1
Electrical conductivity	0	S/m
Relative permittivity	1	1

BASIC SETTINGS

Description	Value
Relative permeability	{{1, 0, 0}, {0, 1, 0}, {0, 0, 1}}
Electrical conductivity	{{0, 0, 0}, {0, 0, 0}, {0, 0, 0}}
Relative permittivity	{{1, 0, 0}, {0, 1, 0}, {0, 0, 1}}

2.2.2 Conductor 1

SELECTION

Geometric entity level	Domain
Selection	Geometry geom1: Dimension 2: Domain 3

MATERIAL PARAMETERS

Name	Value	Unit
Relative permeability	mur1	1
Relative permittivity	1	1
Electrical conductivity	sigmaCond1	S/m

BASIC SETTINGS

Description	Value
Relative permeability	{{mur1, 0, 0}, {0, mur1, 0}, {0, 0, mur1}}
Relative permittivity	{{1, 0, 0}, {0, 1, 0}, {0, 0, 1}}
Electrical conductivity	{{sigmaCond1, 0, 0}, {0, sigmaCond1, 0}, {0, 0, sigmaCond1}}
relpermeability_symmetry	0E0
electricconductivity_symmetry	0E0

2.2.3 Conductor 2

SELECTION

Geometric entity level	Domain
Selection	Geometry geom1: Dimension 2: Domain 2

MATERIAL PARAMETERS

Name	Value	Unit
Relative permeability	mur2	1
Relative permittivity	1	1
Electrical conductivity	sigmaCond2	S/m

BASIC SETTINGS

Description	Value
Relative permeability	{{mur2, 0, 0}, {0, mur2, 0}, {0, 0, mur2}}
relpermeability_symmetry	0E0
Relative permittivity	{{1, 0, 0}, {0, 1, 0}, {0, 0, 1}}
relpermittivity_symmetry	3E0
Electrical conductivity	{{sigmaCond2, 0, 0}, {0, sigmaCond2, 0}, {0, 0, sigmaCond2}}
electricconductivity_symmetry	0E0

Description	Value
relpermeability_symmetry_symmetry	0E0

2.3 MAGNETIC FIELDS

USED PRODUCTS

COMSOL Multiphysics
AC/DC Module

SELECTION

Geometric entity level	Domain
Selection	Geometry geom1: Dimension 2: All domains

2.3.1 Ampère's Law 1

SELECTION

Geometric entity level	Domain
Selection	Geometry geom1: Dimension 2: All domains

Constitutive relation B-H

SETTINGS

Description	Value
Magnetization model	Relative permeability
Relative permeability	From material

Constitutive relation Jc-E

SETTINGS

Description	Value
Conduction model	Electrical conductivity
Electrical conductivity	From material

Constitutive relation D-E

SETTINGS

Description	Value
Relative permittivity	From material

Coordinate system selection

SETTINGS

Description	Value
Coordinate system	Global coordinate system

USED PRODUCTS

COMSOL Multiphysics

PROPERTIES FROM MATERIAL

Property	Material	Property group
Relative permeability	Bound	Basic
Electrical conductivity	Bound	Basic
Relative permittivity	Bound	Basic
Relative permeability	Conductor 1	Basic
Electrical conductivity	Conductor 1	Basic
Relative permittivity	Conductor 1	Basic
Relative permeability	Conductor 2	Basic
Electrical conductivity	Conductor 2	Basic
Relative permittivity	Conductor 2	Basic

2.3.2 Axial Symmetry 1

SELECTION

Geometric entity level	Boundary
Selection	Geometry geom1: Dimension 1: All boundaries

USED PRODUCTS

COMSOL Multiphysics

2.3.3 Magnetic Insulation 1

SELECTION

Geometric entity level	Boundary
Selection	Geometry geom1: Dimension 1: All boundaries

USED PRODUCTS

COMSOL Multiphysics

2.3.4 Initial Values 1

SELECTION

Geometric entity level	Domain
Selection	Geometry geom1: Dimension 2: All domains

Coordinate system selection

SETTINGS

Description	Value
Coordinate system	Global coordinate system

USED PRODUCTS

COMSOL Multiphysics

2.3.5 Force Calculation 1

SELECTION

Geometric entity level	Domain
Selection	Geometry geom1: Dimension 2: Domains 2–3

Force calculation

SETTINGS

Description	Value
Force name	0E0

2.3.6 Line Current (Out-of-Plane) 1

SELECTION

Geometric entity level	Point
Selection	Geometry geom1: Dimension 0: Point 6

SETTINGS

Description	Value
I_0	10

USED PRODUCTS

COMSOL Multiphysics

2.4 MESH 1

2.4.1 Size (size)

SETTINGS

Description	Value
Maximum element size	2.88E-2
Minimum element size	1.63E-4
Curvature factor	3E-1
Maximum element growth rate	1.3E0
Predefined size	Fine

2.4.2 Mapped 1 (map1)

SELECTION

Geometric entity level	Domain
Selection	Geometry geom1: Dimension 2: Domain 3

Distribution 1 (dis1)

SELECTION

Geometric entity level	Boundary
Selection	Geometry geom1: Dimension 1: Boundary 5

SETTINGS

Description	Value
Number of elements	floor(hCond1/nCond1)

Distribution 2 (dis2)

SELECTION

Geometric entity level	Boundary
Selection	Geometry geom1: Dimension 1: Boundary 8

SETTINGS

Description	Value
Number of elements	floor(wBound/nCond1)

2.4.3 Mapped 2 (map2)

SELECTION

Geometric entity level	Domain
Selection	Geometry geom1: Dimension 2: Domain 2

Distribution 1 (dis1)

SELECTION

Geometric entity level	Boundary
Selection	Geometry geom1: Dimension 1: Boundary 3

SETTINGS

Description	Value
Number of elements	floor(hCond2/nCond2)

Distribution 2 (dis2)

SELECTION

Geometric entity level	Boundary
Selection	Geometry geom1: Dimension 1: Boundary 6

SETTINGS

Description	Value
Number of elements	floor(wBound/nCond2)

2.4.4 Free Triangular 1 (ftri1)

SELECTION

Geometric entity level	Domain
Selection	Remaining

Size 1 (size1)

SELECTION

Geometric entity level	Domain
Selection	Geometry geom1

SETTINGS

Description	Value
Maximum element size	3.64E-2
Minimum element size	1.63E-4
Curvature factor	3E-1
Maximum element growth rate	1.3E0

3 Study 1

3.1 PARAMETRIC SWEEP

Parameter name	Parameter value list
mur2	1,10,100,1000

STUDY SETTINGS

Description	Value
Sweep type	Specified combinations
Parameter name	mur2
Unit	

PARAMETERS

Parameter name	Parameter value list	Parameter unit
mur2 (relative permeability of second conductor)	1,10,100,1000	

3.2 FREQUENCY DOMAIN

Frequencies (Hz)
1, range(20,20,2000)

STUDY SETTINGS

Description	Value
Include geometric nonlinearity	Off

SETTINGS

Description	Value
Frequencies	{1, 20, 40, 60, 80, 100, 120, 140, 160, 180, 200, 220, 240, 260, 280, 300, 320, 340, 360, 380, 400, 420, 440, 460, 480, 500, 520, 540, 560, 580, 600, 620, 640, 660, 680, 700, 720, 740, 760, 780, 800, 820, 840, 860, 880, 900, 920, 940, 960, 980, 1000, 1020, 1040, 1060, 1080, 1100, 1120, 1140, 1160, 1180, 1200, 1220, 1240, 1260, 1280, 1300, 1320, 1340, 1360, 1380, 1400, 1420, 1440, 1460, 1480, 1500, 1520, 1540, 1560, 1580, 1600, 1620, 1640, 1660, 1680, 1700, 1720, 1740, 1760, 1780, 1800, 1820, 1840, 1860, 1880, 1900, 1920, 1940, 1960, 1980, 2000}

PHYSICS AND VARIABLES SELECTION

Physics interface	Discretization
Magnetic Fields (mf)	physics

MESH SELECTION

Geometry	Mesh
Geometry 1 (geom1)	mesh1

4 Results

4.1 DERIVED VALUES

4.1.1 Export Table

OUTPUT

Evaluated in	Table 1
--------------	---------

DATA

Description	Value
Dataset	Study 1/Solution 1

EXPRESSIONS

Expression	Unit	Description
-mf.Forceavz_0	N	Repulsive force component on coil
numberofdofs	1E0	Number of degrees of freedom
mur2		relative permeability of second conductor
hCond1	m	height of conductor 1
hCond2	m	height of conductor 2
sigmaCond1	S/m	conductivity of first conductor
sigmaCond2	S/m	conductivity of second conductor

REPORT DOCUMENTATION PAGE

*Form Approved
OMB No. 0704-0188*

The public reporting burden for this collection of information is estimated to average 1 hour per response, including the time for reviewing instructions, searching existing data sources, gathering and maintaining the data needed, and completing and reviewing the collection of information. Send comments regarding this burden estimate or any other aspect of this collection of information, including suggestions for reducing this burden, to Department of Defense, Washington Headquarters Services, Directorate for Information Operations and Reports (0704-0188), 1215 Jefferson Davis Highway, Suite 1204, Arlington, VA 22202-4302. Respondents should be aware that notwithstanding any other provision of law, no person shall be subject to any penalty for failing to comply with a collection of information if it does not display a currently valid OMB control number.
PLEASE DO NOT RETURN YOUR FORM TO THE ABOVE ADDRESS.

1. REPORT DATE (DD-MM-YYYY) 01-03-2021		2. REPORT TYPE Technical Memorandum		3. DATES COVERED (From - To) 2018-2021	
4. TITLE AND SUBTITLE Mathematical Model Development and Experimental Verification of Electromagnetic Force Actuators for use in Space Applications				5a. CONTRACT NUMBER	
				5b. GRANT NUMBER 80NSSC18K1166	
				5c. PROGRAM ELEMENT NUMBER	
6. AUTHOR(S) Robert C. Youngquist, Mark A. Nurge, Katherine T. Wilson				5d. PROJECT NUMBER 295670.01.01.18.01	
				5e. TASK NUMBER	
				5f. WORK UNIT NUMBER	
7. PERFORMING ORGANIZATION NAME(S) AND ADDRESS(ES) NASA John F. Kennedy Space Center Kennedy Space Center, Florida, 32899				8. PERFORMING ORGANIZATION REPORT NUMBER L-	
9. SPONSORING/MONITORING AGENCY NAME(S) AND ADDRESS(ES) National Aeronautics and Space Administration Washington, DC 20546-0001				10. SPONSOR/MONITOR'S ACRONYM(S) NASA	
				11. SPONSOR/MONITOR'S REPORT NUMBER(S) NASA/TM-2021-0010505	
12. DISTRIBUTION/AVAILABILITY STATEMENT Unclassified-Unlimited Subject Category Availability: NASA STI Program (757) 864-9658					
13. SUPPLEMENTARY NOTES An electronic version can be found at http://ntrs.nasa.gov .					
14. ABSTRACT This technical memorandum shows the development of the mathematics needed to model several types of electromagnetic force actuators that may be of interest for use in space applications. The actuators described are capable of providing attractive, repulsive, and longitudinal forces between the actuator and a variety of metal surfaces. Potential applications for these propellant free actuators include spacecraft docking, in-space fabrication, robotic spacecraft inspection and servicing, deflection of metallic debris, and interaction with iron core asteroids (e.g., landing, repelling, and relocating).					
15. SUBJECT TERMS Magnetic Force Actuators, Electrostatic Force Actuator					
16. SECURITY CLASSIFICATION OF:			17. LIMITATION OF ABSTRACT UU	18. NUMBER OF PAGES 112	19a. NAME OF RESPONSIBLE PERSON STI Information Desk (help@sti.nasa.gov)
a. REPORT U	b. ABSTRACT U	c. THIS PAGE U			19b. TELEPHONE NUMBER (Include area code) (757) 864-9658

